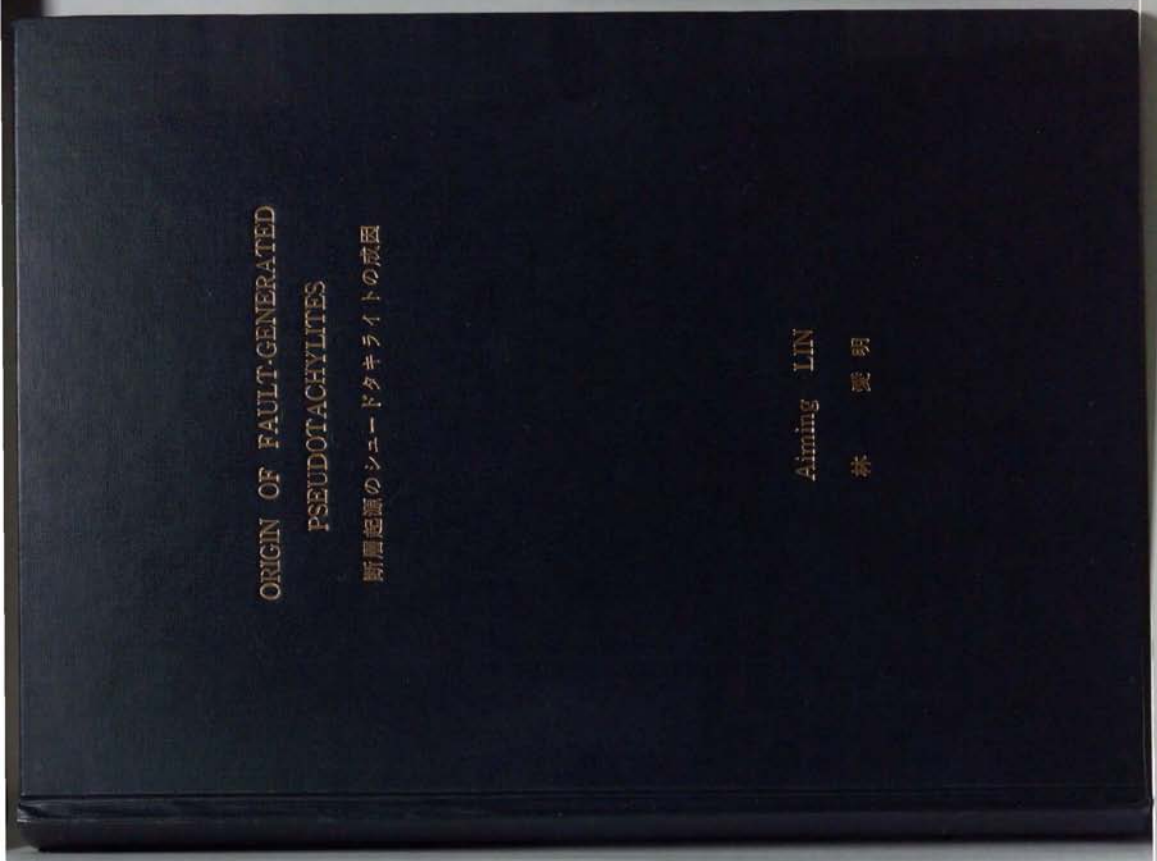
ORIGIN OF FAULT-GENERATED
PSEUDOTACHYLITES
断層起源のシュードタキライトの成因
Aiming LIN
林 愛明


KODAK Color Control Patches
Kodak
Blue
Cyan
Green
Yellow
Red
Magenta
White
3/Color
Black
Kodak Gray Scale

東京大学博士論文

# ORIGIN OF FAULT-GENERATED PSEUDOTACHYLITES

# 断層起源のシュードタキライトの成因

by

Aiming LIN

林 愛明

December 1991

## ABSTRACT

The origin and process and mechanical mechanism of formation of fault-generated pseudotachylites (PT) have been studied with the Fuyun PT from the Fuyun fault zone, northwest China and experimentally-generated PT.

Glassy and microlitic PT were found as a thin layer on the fault plane and as single veins or complex network of veins injected into country rocks of granitic mylonites from the Fuyun fault zone. The powder X-ray diffraction data indicate that the fine-grained matrices in the Fuyun PT vary from almost crystalline to complete glass (a few to 90 weight percents). The X-ray diffraction patterns also indicate that clasts in the glassy type PT veins consist of mostly quartz grains. These analyses show that the other minerals such as micas and feldspars contained in the host granitic rocks have been preferentially melted during the PT formation.

Microlites showing quenching or rapid-cooling textures such as skeletal, dendritic and complex spherulitic shapes, are found in the microlitic PT veins. There is a gradation in the size and shape of microlites from the margin to the center of veins; they become larger in size and more complex in morphology toward the center. The microlites are mainly made up of sanidine, anorthoclase, pyroxene, plagioclases ($An_{30}$-$An_{70}$), biotite and hornblende with high Ti component, which are not present in the host rocks formed in sub-epidote amphibolite facies. The presence of the high-temperature minerals of microlites indicates that they were the primary crystals formed from a melt. The vesicles or

amygdules, flow structures which resemble to similar folds in form, and rounded fragments are universal in the Fuyun PT.

The average bulk chemical compositions of the PT are very similar to that of the host rocks. But the glassy matrix has a low $SiO_2$ component which is 5-15 Wt.% lower than that of the host rocks. Locally, glasses with quartz and plagioclase components, generally rimed around the quartz fragments, are found. The PT contain 2-3 Wt.% water ($H_2O^+$). Using the experimental data relating the solubility of water to pressure in an andesitic melt, about 400 bars (40 MPa) normal pressure corresponding to about 1.5 km depth of PT formation is estimated. An estimated minimum temperature of about 1450 °C is obtained by the presence of the pure $SiO_2$ glass. Those estimates are based on the experimental results under equilibrum conditions and hence are tentative, because the frictional melting is unlikely to be an equilibrium phenomenon as demonstrated by the following experimental study.

In order to understand the mechanical mechanism and process of the melting-originated pseudotachylite formation, high-speed friction experiments on granites, gabbros, quartzite, anorthosite and albitite have been conducted using a rotary-shear high-speed frictional testing machine. Experiments were carried out on cylindrical specimens of 25 mm in diameter, under normal stresses of 1.0-1.5 MPa and maximum slip rates up to 2 m/s. The total displacement at the margin of cylindrical specimens exceeded 100 m in some runs.

Experimental results clearly show that the frictional melt form at least after displacements of a few meters under such low normal-stress conditions. The single vein generated along a shear zone and the network pseudotachylite veins injected into the host rocks were successfully

simulated. Experimentally generated PT consists of fused glass with abundant vesicles and angular or sub-angular to rounded fragments, and sometimes occurs as injected veins in fractured rock. The presence of glass (40-50 weight percents) was confirmed by quantitative analyses using the intensity of X-ray diffraction peaks. The $SiO_2$ content of the glass is smaller than that of the granitic host rock by 10-15 Wt.%. The analyses of the mineral contents of clasts in experimentally-generated PT in granite indicate that quartz is most resistant to melting, biotite least resistant, and feldspars are intermediate. Thus the $SiO_2$ depletion in the PT glass is likely to be due to such selective melting of constituent minerals during frictional heating.

In order to test whether the frictional melting is in chemical equilibrium melting or not, the frictional melting experiments on albitite-quartzite pair, which has a eutectic relationship and on anorthosite specimens (Ab-An solid solution) have been conducted. The results show that the albite with lower melting temperature melted in the former case and that the composition of the fused glass is the same as that the composition of the constituent plagioclase in the latter case. These results clearly indicate that the frictional melting is not an equilibrium phenomenon, and this must be kept in mind when one estimates the temperature reached during the formation of PT in nature.

The experimental studies so far successfully reproduced natural PT in terms of textures (except for the growth of microlites) and chemical compositions.

The petrological studies of the Fuyun PT demonstrate that the Fuyun PT formed by frictional melting on a shear plane under water-saturated conditions rather than dry conditions. Experimental results show

that the melting-originated PT can be generated by frictional heating at shallow depths as small as several tens of meters if deformation is confined to very thin planar zone, and that the frictional melting formed by selective melting in a chemical non-equilibrium state, other than total melting or partial melting of rocks during seismic faulting in a fault zone.

## ACKNOWLEDGMENTS

I would like to express my sincere thanks to Prof. Tokihiko Matsuda and Dr. Toshihiko Shimamoto for their advice and support throughout the course of this study. I thank Prof. Toshitsugu Fujii for his advice and discussions in petrographic work. I greatly appreciate the guidance offered by Mr. Ge Shumo, Mr. Tang Youbiao, Miss. Gao Guoyi and Miss Wei Ruoping in the field. I would also like thank Dr. Hikaru Iwamori for discussion and XRF analysis. I am grateful to Drs. Shigeru Yamashita, Atsushi Yashuda for their help in SEM-EDX analysis. I also would like to thank Drs. Akira Kato and Yoshiharu Hirayama for their help in powder X-ray analysis. I appreciate the help of Dr. Hideo Takagi in kindly providing the Outer Harries pseudotachylite samples. I appreciate the help and discussions with Drs. Yasuji Saito, Hiroshi Sato, Harutaka Sakai, Hiroyuki Nagahama, Akito Tsutsumi and Yukiko Otomo, and Mr. Norio Shigematsu. I thank Dr. Peter Sammonds for critically reading the manuscript.

I am also grateful to Miss. Tokie Wadanabe, Mrs. Chitani Harayama and Mr. Kiyotaka Kato for their kind help in the course of this study. I thank all my friends and colleagues for their generous assistance and care both academically and personally during these years.

Last but not least, I must acknowledge my family and my wife Sujuan Lin, for their help and support which made this dissertation a reality.

CONTENTS

# CHAPTER I. INTRODUCTION

The term pseudotachylite was introduced by Shand (1916) for a dark, aphanitic rock found as veins and networks in the granites in the Parys, South Africa. These rocks generally have some characteristics of sedimentary rocks in which the breccias are cemented by fine-grained material, and others of igneous rocks that have intruded fractures. Most the pseudotachylites known in the world are generally associated with faults such as those occurring in the Gairloch district in Scotland (Park, 1961), the Quebec, Canada (Philpotts, 1964), the Outer Hebrides Thrust, Scotland (Sibson, 1975), the Alpine Fault Zone, New Zealand (Wallace ,1976), the Arunta Block, central Australia (Allen, 1979), the Tanlu fault zone, China (Yang et al. 1981) and the Main Zone of the Hidaka metamorphic belt, Japan (Toyoshima, 1990).

Although there is considerable controversy about the origin of fault-generated pseudotachylites, most of researchers agree that they are generated by frictional melting of the rock due to heat generated during seismmogenic motion (e.g. Mackenzie & Brune, 1972; Sibson, 1973, 1975, 1980; Passchier, 1982). Wenk (1978) disagrees with the melting origin, but he agrees that pseudotachylites appear to be formed by a predominantly brittle mechanism at moderate to deep crustal levels and may be related to earthquakes. So, studies of fault-generated pseudotachylites should provide important information when estimating the state of earthquake faulting along a fault. Furthermore, it may be possible to place constraints on geophysical modes of the fault as a earthquake source, which otherwise are based largely on seismological data.

Even though the existence of pseudotachylites has been known for over a century, there are relatively few reports of pseudotachylites in the world, so they are still considered to be enigmatic and exceptional rocks and their origin is still in dispute. Two main hypotheses have been proposed, one is a friction melt (e.g. Park, 1961; Sibson, 1973, 1975), the other is an ultracrushed powder (e.g. Clough, 1888 cited in Francis, 1972; Wenk, 1978; Wenk & Weiss, 1982). The very fine-grained matrix hampers the observation of textures and constituent minerals, hindering progress in the study of their origin. The origin of the microcrystalline texture in the fault-generated pseudotachylites recently described by Wenk (1978), Wenk & Weiss (1982), Maddock (1983) and Macaudiere et al. (1985) is more controversial, although they all have observed the texture using the TEM (Transmission Electron Microscope) method. Nevertheless, uncertainties still remain over many aspects of their genesis. The problem of the origin of fault-generated pseudotachylites is still unsolved. It is necessary to study a wide variety of pseudotachylites, their field occurrences, textures and chemical compositions, in different locations to solve the question of their origin.

The objective of this study is to attempt to clarify the origin and the process of formation of fault- generated pseudotachylites in a fault zone by field surveying, petrographic and experimental studies. After observations of many pseudotachylites collected from several locations in the world, the pseudotachylites from the Fuyun fault zone, Xinjiang Province, northwest China were selected for the present study because they are very well preserved and little altered or metamorphosed. Frictional melting experiments have been conducted to simulate the process of formation of fault-generated pseudotachylites and to try to understand the

mechanical mechanism of seismic faulting on a fault plane during the forming of pseudotachylites, using a rotary-shear high-speed frictional testing machine. Powder X-ray diffraction and SEM-EDX (Scanning Electronic Microscope-Electron Dispersive X-ray) methods are used in this study.

## CHAPTER II. PREVIOUS WORK

Since Shand (1916) named the pseudotachylite, the pseudotachylites have been reported from the seven continents. Previous work, undertaken before the 1970's, is well summarized in the reviews by Philpotts (1964) and by Francis (1972). In the last two decades, there have been a large number of descriptions of pseudotachylites found in many locations, reports of simulation studies utilizing both modeling calculations and artifically-generated pseudotachylites, and microstructural studies by SEM-EDX and TEM. Previous work is reviewed in the following two sections.

### II-1. Field occurrences and petrographic studies

Although the pseudotachylites can be classified into three types: fault-generated type, landslide-generated type and impact-generated type (Takagi, 1991), most are related to faulting. Fault-generated pseudotachylites have so far been described in many major fault zones throughout the world such as in the Himalaya thrust, Nepal (Scott & Drever, 1953); the Gairloch district, Scotland (Park, 1961); the Quebec, Canada (Philpotts, 1964); the Outer Hebrides Thrust, Scotland (Sibson, 1975); the Alpine Fault Zone, New Zealand (Wallace, 1976); the Arunta Block, central Australia (Allen, 1989); the Tanlu fault zone, China (Yang et al., 1981); the Ikertoq shear belt, west Greenland (Grocott, 1981); the Koli Nappes Tannforsfaltet, central Sweden (Beckholmen, 1982); the

Saint- Barthekemy Massif, France (Passchier, 1982); the Bavali fault zone, India (Sinha-Roy & Kumar, 1985); the Redbank shear zone, central Australia ( Hobbs et al., 1986); the Fort Foster Brittle Zone, U.S.A. (Swanson, 1988); the Iida-Matsukawa fault, central Japan (Lin, 1988, 1989); the Palala shear belt, south Africa (Brandl & Reimdd, 1990); the Hidaka metamorphic belt, Hokkaido, Japan (Toyoshima, 1990).

Most of the pseudotachylites in published descriptions have striking similarities: being brown-brownish black to black in color, dense, aphanitic in appearance, occurring as irregular veins intruded into country rocks both as simple veins and complex networks, and generally a few millimeters to a few centimeters in width. It was Shand (1916) who first described and sketched the occurrence of irregular, branching pseudotachylite veins in the Vredefor region, South Africa. Sibson (1975) classified the fault-generated pseudotachylite veins into two fundamental classes of veins: (i) fault veins, lying along markedly planar shear fractures on which the pseudotachylite has been generated and (ii) injection veins, intruded into the country rocks and often appear to be dilatational veins along which there has been no lateral offset of markers. Evidence of repeated episodes of fracturing and pseudotachylite formation is one of the most universal features of all fault-generated pseudotachylite occurrences. Grocott (1981) examined the fracture geometry of pseudotachylite generation zone in the Ikertoq shear zone and concluded that this pseudotachylite generation zones has a systematic fracture geometry and that the intrusion of veins of pseudotachylite off the principal displacement shear fractures may be contemporaneous with minor shear fracturing in the generation zones. Swanson (1988), mapping the Fort Roster Brittle Zone, described the pseudotachylite and minor breccias that

have been produced in the intricate internal duplex structure of a system of dextral strike-slip faults.

Alterated occurrences of pseudotachylites and mylonitic deformation in the same shear zone have been observed by several authors (Sibson, 1980; Stel, 1981; Wenk & Weiss, 1982; Passchier, 1984; Hobbs et al., 1986). Sibson (1980) observed the occurrence of pseudotachylites within a ductile shear zone of the Outer Hebrides Thrust Zone, Scotland, and suggested that the pseudotachylite has been produced intermittently by seismic slip on the discrete planes within an otherwise ductile deformation shear zone. Passchier (1984) described the alteration in the development of pseudotachylite and ultramylonite in the Saint-Barthekemy Massif, and suggested that this alterative deformation is restricted to the brittle-ductile transition. However, Hobbs et al. (1986), after investigating the texture of pseudotachylites deformed in a ductile manner in the Redbank Shear Zone, central Australia, proposed that pseudotachylite and associated ultramylonite can develop entirely within the ductile regime as ductile instabilities. The modes and textures show that the fault-generated pseudotachylites are not only generated in brittle regime but also in the ductile regime.

Microscopically, pseudotachylites mostly consist of an ultra-fine grain matrix and dispersed porphyroclasts. There are two main hypotheses concerning the origin of fine-grained matrix; (1) the fine-grained matrix was originally glassy or was microcrystalline formed by frictional fusion with some devitrification overprinted with time (e.g. Park, 1961; Sibson, 1975); (2) his fine-grained matrix was not initially glassy but consists of fine-grained powders produced by mechanical comminution or shock (e.g. Wenk, 1978; Wenk & Weiss 1982; Masch et al. 1985).

The various evidences generally cited to show that the pseudotachylites are of melt origin are the presence of glass or glassy material, microcrystalline and microlites, vesicles and amygdules, flow structure and corroded fragments. Nevertheless, some arguments against each of these evidences have been put forward.

Scott and Drever (1953) described for the first time a rock truly formed by frictional fusion in the Himalaya Langtang thrust fault. The glass, which commonly is brownish or pale yellowish-brown in color, and less commonly colorless, penetrated the interior of the porphyroclasts, is bubbly in appearance, and has a reflective index of 1.492 to 1.508. This was the first conclusive proof that the melting can be generated by frictional heat on a shear plane. Masch et al (1985) re-examined and reaffirmed this vesicular glass of the Langtang Himalaya pseudotachylite by TEM analysis, but they also documented that the glass formed by frictional melting on the landslide surfaces, not along a tectonic fault. Park (1961) described small patches or veinlets of clear pale green or pale brownish isotropic glass present in the pseudotachylites in crush belts of the Gairloch district, Scotland. Philpotts (1964) also described by microscopic observation that the glasses in the pseudotachylites in a fault zone of the Quebec, Canada, have a reflective index of approximately 1.56 and a specific gravity of 2.76-2.78. Glasses or glassy material mainly observed under the microscope have also been described elsewhere such as Gupta (1967), Ermnovics et al. (1972), Sibson (1975), Sibson et al. (1981), Wallace (1976), Allen (1979), Sinha-Roy & Kumar (1985) and Toyoshima (1990). However, Waters & Campbell (1935) argued that the matrix of pseudotachylites is not glass, based on the observation of the abrupt drop in the index of refraction upon fusion of a small piece of

pseudotachylite. They suggested that the isotropic character of the groundmass material could be formed in crushed rocks. Wenk (1978) re-examined the pseudotachylite of the Outer Hebrides, Scotland, studied by Sibson (1975), the Musgrave ranges, South Australia and the Insubric, Italy by TEM analysis, and showed that only minor glass or devitrified textures are observed, so then concluded that the pseudotachylites are products of cataclasis rather than melting. Weiss and Wenk (1983) argued that the fine-grained component of the pseudotachylite would most probably be identified as glass by conventional methods of analysis such as optical microscope. Thus, the presence of point or pocket glass or glassy material is not conclusive evidence for the origin of pseudotachylites.

The presence of microlites usually is considered as one of the commonest characters of pseudotachylite of melt origin and is described in a number of the literature (Shand, 1916; Park, 1961; Philpotts, 1964; Sibson, 1975; Masch et al. 1977; Wallace, 1976; Allen, 1979; Beckholmen, 1982; Macaudiere & Brown, 1982; Maddock, 1983; Magloughlin, 1989; Toyoshima, 1990). The microlites found in pseudotachylites vary morphologically from simple shape to complex, such as acicular, globular, dendritic, skeletal and spherulitic in texture, which are suggested to be the result of supercooling or quenching textures from a melt (e.g. Park, 1961; Philpotts, 1964; Maddock, 1983; Toyoshima, 1990). Most of the microlites described so far consist of plagioclase (An<40). Some of them consist of alkali feldspar, biotite, pyroxene, amphibole and some opaque mineral. Waters & Campbell (1935), however, described that the similar shaped microlites are present in the mylonite of the San Andreas fault and suggested that the microlites were developed by metamorphic

recrystallization. Masch et al. (1985) found that the all dendritic to spherulitic microlites in the pseudotachylites of the Silvretta region in the Alps are albite and concluded that these microlites were formed by metamorphism. They argued that the spherulitic textures could be formed by metamorphism in low grade metamorphic terrain and the microlites may actually be porphyroclasts in pseudotachylites. Nevertheless, the argument against the melt origin can not be accepted in many cases such as those stated by Maddock (1983) and Toyoshima (1990). It is necessary, of course, to study in more detail the morphology, mineral type and textural variation in pseudotachylite vein to determine the origin.

The microstructures of fine-grained groundmass in pseudotachylites were explained in two completely opposite ways. Wenk (1978) examined the fine grained groundmass of the pseudotachylites from the Musgrave ranges, South Australia, the Outer Hebrides Thrust Zone, Scotland and Insubriic Line, Italy first by TEM analysis. He found that the fine grains appear strongly strained and recrystallization is common, and ranging in appearance from small, isolated nuclei to polygonal mosaic texture, and he concluded that these textures were formed by shock rather than by melting. However, Macaudiere et al. (1985) examined the fine grained groundmass of pseudotachylite from the South Harries, Scotland, also by TEM and SEM analyses, and found that the fine grains have polygonal microcrystalline textures showing signs of weak internal deformation and suggested that they were not formed by devitrification, but from a melt at much greater degrees of supercooling than the spherulitic and bow-tie textures. These arguments again show that it is very difficult to obtain conclusive evidence for the origin of pseudotachylite even by TEM analysis.

Vesicles and amygdules found in pseudotachylites are a convincing evidence that clearly indicate a former melt state, although Philpotts (1964) pointed out that the fluidized solid-gas systems stated by Reynolds (1954) could explain the presence of vesicles in pseudotachylites. They have been described in some papers (Scott & Drever, 1953; Philpotts, 1964; Allen, 1979; Beckholmen, 1982; Maddock et al, 1987; Toyoshima, 1990). Philpotts (1964) described that the vesicles and amygdules increase from the margin to center by as much as 25 per cent in volume in pseudotachylite veins. Amygdules are usually filled with some mineral assemblages such as quartz, feldspars, epidote, carbonate and magnetite (Philpotts, 1964; Maddock, 1987). Using the published data relating vesicle abundance and the solubility function for $H_2O$ and $CO_2$, to pressure, Maddock et al (1987) inferred a formation depth of about 1.6 km for the Greenland pseudotachylite.

Flow structures are often observed in some fault-generated pseudotachylites (Scott & Drever, 1953; Park, 1961; Gupta, 1967; Ermanovics et al., 1972; Sibson, 1975; Wallace, 1976; Masch et al., 1977; Allen, 1979; Beckholmen, 1982; Macaudiere & Brown, 1982; Macaudiere et al., 1985; Toyoshima, 1990). These flow structures usually show flow bandings or flow lamellae which are alteration of thin layers and streaks of slightly different composition exhibiting straight line or complex curves in shape. Generally, they are suggested to be formed by a flowing melt (Scott and Drever, 1953; Park, 1961; Macaudiere et al., 1985; Toyoshima, 1990). Reynolds (1954) proposed that the flow structures in pseudotachylite might be formed by a transportation of fine-grained fragments by a gas-solid system.

Various shapes of corroded fragments in pseudotachylites have been explained to be eroded by melt heating in much of literature (Shand, 1916; Scott & Drever, 1953; Park, 1961; Philpotts, 1964; Ermanovics et al., 1972; Sibson, 1975; Wallace, 1976; Allen, 1979; Macaudiere & Brown, 1972; Maddock, 1983; Beckholmen, 1982; Macaudiere et al., 1985; Masch et al., 1985; Toyoshima, 1990). The fragments in pseudotachylites often show sub-angular, rounded and embayed in shape. Sibson (1975) attributed the rounding of fragments in pseudotachylites to three main processes: (1) attrition caused by rotational grinding, proposed by Waters and Campbell (1935) and Reynolds (1954); (2) explosive decrepitation due to fluid expansion during rapid heating; and (3) thermal corrosion by the melt phase. The rounded structures are also not a conclusive evidence for the melt origin.

Shimamoto & Nagahama (1991) made the analyses of clast-size distribution for the pseudotachylite taken from Australia. They found that there is an abrupt decrease in the number of crushed fragments below about 5μm. They concluded from this that the most of fine-grained matrix of pseudotchylites cannot be the crush products and denied the crush origin.

In order to understand whether the isotropic or unisotropic fine-grained matrix is glass or not, Willeme (1937, cited in Francis, 1972) made the first powder X-ray analysis of the pseudotachylite described by Shand (1916), and found that the fine matrix was more typical of a crystalline powder of extremely fine grains than of glass. Macaudiere et al. (1985) and Toyoshima (1990) also made powder X-ray analyses of pseudotachylites, and could not obtain a typical glass diffraction pattern. Hence pseudotachylites examined so far with X-ray diffraction did not contain much glass.

The average chemical compositions of some pseudotachylite veins are very similar to that of host rocks in which they occur (Shand, 1916; Philpotts, 1964; Sibson, 1975; Wenk & Weiss, 1982; Schwarzman et al. 1983; Sinha-Roy & Kumar, 1985; Macaudiere et al., 1985; Magloughlin, 1989). The similarity of compositions between the pseudotachylites and host rocks in which they occur was suggested to be a result of total melting of host rock (Shand, 1916; Philpotts, 1964) or of fine materials derived locally from the host rock (Schwarzman et al., 1983). But, there are some data showing a striking difference between the fine grained matrix of pseudotachylite and the host rocks (Wilshire, 1971; Ermanovics et al., 1972; Sibson, 1975; Masch et al., 1985; Reimold et al., 1987). The difference of compositions between the pseudotachylites and host rocks was explained to be generated by partial melting of the host rock (Ermanovics et al., 1972; Masch et al., 1985). Generally, the relicts of fragments in pseudotachylites are quartz and feldspar. There are no hydrous mineral fragments such as biotite and hornblende even though they are present in the host rock. This was suggested to be formed by the preferential fusion of hydrous minerals (Allen, 1979).

The absolute ages of pseudotachylites have been determined by some workers (Philpotts & Milter, 1963; Reimold et al., 1981, 1987, 1990; Seward & Sibson, 1975; Peterman & Day, 1989). There are only two datings for the fault-generated pseudotachylites. One was made based on the K-Ar dating method by Philpotts & Milter (1963) and a Pre-Cambriam age was obtained. The other was made based on the fission track dating method for the pseudotachylite of the Alpine Fault Zone, New Zealand by Seward and Sibson (1985) and a age of 0.43±0.1 Ma was obtained. For the pseudotachylite of the Alpine Fault Zone, the formation

depth of 2.2±1.0 km was estimated from the dated age (Seward & Sibson, 1985). Pseudotachylites from impact structures have also been successfully dated by Rb-Sr, K-Ar and Ar-Ar dating methods (Reimold et al., 1981; 1987; 1990). The paleomagnetism method has also been used to try to date the pseudotachylite (Piper & Poppleton, 1988). These results show that it is possible to determine the timing of seismic faulting events in a fault zone and impact events.

The presence of the Fuyun pseudotachylites studied here have been reported by Ge et al. (1985) and Du et al. (1987), but there are no detailed descriptions about the field occurrences or petrographic studies for the Fuyun pseudotachylites.

### II-2. Experimental and theoretical studies

Some experiments have demonstrated the frictional melting could indeed occuron a fault zone during seismic slip (Friedmen et al., 1974; Spray, 1987, 1988; Killick, 1990). Spray (1987) used a friction welding apparatus to simulate melting on a fault plane. He reported that a 150 um thick fused layer of rock had been produced by rotating two metadolerite core faces against each other at a mean surface stress of 5 MPa and mean surface velocity of 0.24 m/s for a condition of 11 seconds. This corresponds to the conditions formed at depths shallower than 200m from the earth's surface, during seismic fault motion in a fault zone. But, in the experimental products, there are no actual melting textures such as microlites, spherulites and vesicles. The glass was only identified under microscope. Another experiment was made by Spray (1988) using the same apparatus at an estimated pressure of 0.5GPa to 1 GPa, and at a

velocity of 1.35 m/s, for 10 seconds. In this experiment, the actual melting textures such as vesicles, microlites and spherulites and rounded fragments were generated. The generated temperature was estimated in the range 1000-1400 °C. The frictional melting on a shear plane was also generated by the frictional overheating of a diamond drill in a drilling experiment at estimated slip rates of 1 m/s and shear stress of about 100 bar-190 bar (10 MPa-19 MPa) for 3-10 s (Killick, 1990). The temperature generated was estimated to be 800-1000 °C. These experimental results show clearly that melting can be generated by a frictional heating on a shear plane in a fault zone. But, in these experiments the mechanical mechanism of frictional melt on a fault plane is still unknown.

Weiss & Wenk (1983) made an experiment simulating the process of catastrophic failure of gabbroic rocks under rapidly applied stress in the range 2.0-4.0 GPa. The products formed a brown vein which consist of fine grains and closely resembles some pseudotachylites. No glass material and melting textures could be found by the TEM analysis. They concluded that the comminuted layers are associated with the formation of ractures in initially intact rock.

On the other hand, analyses of frictional heating on a fault have been carried out by Mackenzie and Brune (1972), Richards (1976), Cardwebl et al. (1978), Sibson (1979, 1980) and Voight & Faust (1982). The calculations are generally carried out by supposing that the problem is one-dimensional and provided slip is confined to a narrow zone (<1 cm). The general conclusion is that the production of pseudotachylite friction melt should be a fairly common phenomenon at seismic slip rates, even for shear resistances as low as 100 bars (10 MPa), once slip exceeds a few

centimeters. Sibson (1973, 1980) suggested that the general scarcity of pseudotachylite is due either to seismic faulting taking place with water held roughly at constant volume around the fault plane, or to the distributed deformation within the fault zone during seismogenic fault motion.

In summary, even though much of petrologic evidences seem to support that the melt origin of pseudotachylite is formed by frictional melting, the question of the origin of fault-generated pseudotachylite is by no means solved. An integrated field, petrological and experimental studies are needed to understand the pseudotachylite-generating processes.

# CHAPTER III. FIELD OCCURRENCES OF PSEUDOTACHYLITES AND ASSOCIATED FAULT ROCKS IN THE FUYUN FAULT ZONE, NORTHWEST CHINA

## III-1. Geological setting of the Fuyun region

The Fuyun region is located on the southwestern side of the Aertai mountains, northwest China (Fig. 1). The basement consists of Palaeozoic metamorphic rocks which are crystalline schist, gneiss, metamorphic volcanic rocks, Mesozoic granitic rocks and sediments. The metamorphic rocks of the Fuyun region have experienced two main tectonic events: (i) a Hercynian movement which folded the basement and formed the NW-SE Aertai arch establishing the regional character of the terrain, and (ii), a Mesozoic Yanshan movement which produced the granitic rocks intruding in the Palaeozoic metamorphic rocks (Bei et al., 1985). The K-Ar dating studies show that the intrusion of granitic rocks occurred in 80-110 Ma (Bei et al., 1985).

The Fuyun fault zone, with a NNW-SSE trend, about 180km in length, cuts the NW-SE Aertai arch obliquely, and formed a boundary between the Aertai mountain and Zhunger basin (Fig. 1). The Fuyun fault dextrally displaced the Palaeozoic metamorphic rocks and Mesozoic granitic rocks about 26-30 km from the Tertiary (Ge et al., 1985). This fault also cut and displaced the peneplains formed from the Miocene to the Holocene with different displacements ranging from 1 km to a few

meters vertically (Bei et al., 1985). This means that the Fuyun fault zone formed after the intrusion of granitic rock (80-110 Ma) and the movement continued in the Quarternary as an active fault. In 1931, surface faulting caused by a magnitude 8.0 earthquake occurred along the geological fault zone extending about 180 km in length. The maximum horizontal displacement observed is as large as 14 m locally. The dextral sense of movement, marked by the valley, scarp, trees etc., coincides precisely with geological fault. Trenching studies show that there are six large seismic faulting events along this fault during the Holocene.

The fractured zone generally ranges from a few tens of meters to a few hundreds meters in width, in which the schist, gneiss and mylonites have been cataclastically deformed. Along the fault zone, the granitic rocks have been mylonized from a few tens of meters to one kilometer in width (Bei et al. 1985). The mylonitic foliations are uniformly parallel to those of the schist and gneiss on a regional scale (Lin & Fan, 1984).

## III-2. Fault rocks and field occurrences of pseudotachylites in the Fuyun region, northwest China

### *Fault rocks*

Pseudotachylites occur at two locations, the Haizikou and the Akesanyi along the Fuyun fault zone in the northern segment (Fig. 1). The prominent outcrop of pseudotachylites and associated fault rocks was exposed in the Haizikou location along the shore road of the Keketuohai lake as shown in Fig. 2 and sketched in Fig. 3. The pseudotachylite-bearing fractured zones ranging about 200 m on the western side of the

earthquake fault (Figs. 2,3) are composed of granitic mylonites which have been re-deformed by a brittle mechanism and cataclastic rocks including fault breccias and gouges [Using the terminogy of Sibson (1977) in this study]. The intensity of mylonization observed by the foliation structures in the field increases from the western margin of the fractured zone bounding with the granitic rocks towards the earthquake fault in the Haizikou location.

Microstructurally, cataclastic textures, kink bands, quartz deformation lamellae and dynamically recrystallized grains occur in the granitic mylonite (Fig. 4). Feldspars show generally more obvious cataclastic structure than quartz. Fine recrystallized quartz grains fill in some microstructures. Kink bands occurring in biotite are both single type and conjugate type (Fig. 4B). Kink bands in feldspars generally occur in microclines which often exhibit cataclastic textures (Fig. 4B, C).

Quartz deformation lamellae are one of prominent deformation characteristics in the granitic mylonites (Fig. 4D). The crystallographic orientation of the deformation lamellae which was determined by measuring the angle between their pole and the C-axis, shows that they belong to the Subbasal-I type which forms under moderate temperature and low pressure conditions (Lin & Fan, 1984). Studies of the mineralogy show that mylonization took place under sub-epidote-amphibolite facies conditions at 10-15 km depth (Lin & Fan, 1984).

After formation of the mylonites, progressive brittle deformation developed in the mylonite which was followed by the injection of quartz veins, calcite veins and epidote veins, and the formation of cataclastic rocks including fault breccia and gouge. The progressive brittle deformation of the associated fault rocks through the development of shear fractures

can be divided into following three stages, depending on the characteristics of fractures and the degree of deformation of the rocks.

(1) First stage:- the development of isolated shear fractures along which there is no obvious evidence of displacement. These fractures have been filled by epidote, calcite and quartz veins (Fig. 3). In hand samples, only some small fractures can be observed. In thin section, the veins show an intense cataclastic texture and have highly variable grain size and highly angular grain shape with no shape fabric. This indicates that these veins formed and then cataclastically deformed under depths shallower than 10-15 km, the depth of granitic mylonite formation.

(2) Second stage:- the formation of a complex network of shear fractures accompanied by the pseudotachylite formation. In this stage, many generations of shear fractures occur, often accompanied by induced second order fractures, which generally cut and displace the calcite and quartz veins formed in the early stage. The orientations of the fractures were measured and are shown in Fig. 2. Most of the fractures are oriented in two directions: one is NNW-SSE, parallel to the main trace of the Fuyun fault zone; the other is NNE-SSW, which may be conjugate to the NNW-SSE shear fractures. The slickensides occurring on the NNW-SSE main shear planes show that the shear sense is dextral with a normal displacement (Fig. 3). Pseudotachylites occur at this stage, often as single vein or complex networks (Fig. 3), which also cut and are injected into the calcite and quartz veins. This indicates that the pseudotachylites formed later than the calcite and quartz veins, at a shallow depth by brittle deformation.

(3) Third stage:- intense damage and formation of fault breccia and gouge zones along some main shear fractures (Fig. 3). The width of the

damaged zone which is composed of unconsolidated breccia and gouge zones is variable from a few ten of centimeters to a few meters, in which the width of gouge zone is about a few millimeters to a few ten centimeters. The damaged zone is defined primarily by an increase in fracture intensity. The intensity of deformation in the damaged zone increases towards the fault gouge zone. The continuity of damaged zones is apparent relative to the fractures formed in the early stage, at the scale of individual exposures which range up to a few hundred meters in length. That the damaged zones cut and displace the epidote, calcite and quartz veins and the fractures formed in the early stages, shows that the damaged zones formed at the last stage of the brittle deformation in the Fuyun fault zone. On the main damaged zone, a fresh continuous fault scarp, which cut and displaced the Holocene alluvial, occur ranging up to a few kilometers in length and striking parallel to the earthquake fault trace of 1931. This indicates that the fault along the main damaged zone is active still in the Holocene.

Structures in the intensely fractured basement indicate a complex history with episode of deformation by brittle and ductile mechanisms.

### *Occurrences of the Fuyun pseudotachylites*

The pseudotachylites occur as a single vein or injected complex network veins in some fractured zones (Fig. 3). The shear fractured zones containing pseudotachylite occur over an interval of a few meters to about 20 meters in the section perpendicular to the Fuyun fault zones, and are about a few ten centimeters to a few meters in width. The single veins often occur as a thin layer or film of a few millimeters in width,

locally as a lump on concaves ranging up to 20-30 centimeters in diameter, on the marked shear surfaces (Fig. 5), where the country rocks have been intensely fractured but solidified. Locally, the flow structures characterized by oriented small fragments and colored layers in these single pseudotachylite veins can be observed with the naked eye. They are parallel to the striations occurring on the fault plane (Fig. 5C,D).

One of the typical modes of highly irregular, branching intrusion network pseudotachylite veins has been traced from a field section, using real scale, and is shown in Fig. 6. The network veins injected in fractures never show any regularity or oriented direction (Figs. 6,7A). Some injected veins can be traced back to the parent pseudotachylite-generated shear plane by the continuity of veins. The injected veins progressively branch, and often thin out and terminate blindly or end abruptly (Figs. 3,6,7B. ). The width of pseudotachylite veins are variable from a few millimeters to ten centimeters, but generally from 5-6 mm to 2 cm.

In several locations, the branching pseudotachylite veins cut and are injected into the quartz veins along very small fractures, where there is no obvious displacement (Fig. 7C). The boundary between the quartz vein and the pseudotachylite vein is very sharp, along which the pseudotachylite veins often can be cleaved easily. Cracks perpendicular to the margin of the vein can be observed in this pseudotachylite veins with the naked eye. They are those formed by rapid cooling in volcanic dikes.

Pseudotachylites generally are brown, brown-black and black in color. In some thick veins, the variation in color between the margin and center of vein can be observed with the naked eye. The margin often exhibits a more dull color than the center (Fig. 7D). Some color bands occur in veins with straight lines parallel to the margin or dragged curves, like to similar

fold in shape. This clearly indicates that there is a flowing process during pseudotachylite formation. The contact between the pseudotachylite veins and the country rocks, as seen with the naked eye, is perfectly sharp even on the weathered surfaces, where pseudotachylites generally are aerugo or brown in color. Pseudotachylites generally show a aphanitic, flint-like appearance. Some freshly exposed surfaces of pseudotachylites show an obvious virtrous luster and perlitic cracks similar to those of glassy volcanic rocks such as obsidian or perlite.

# CHAPTER IV. PETROGRAPHY OF PSEUDOTACHYLITES

## IV-1. General description

There are many common characteristics in the Fuyun pseudotachylites. Pseudotachylites generally are opaque and brown to black in color when viewed in thin section of ordinary thickness under the microscope. Therefore, sections must be cut very thin in order to observe the microstructure. Microstructurally, pseudotachylite veins occur both as simple veins and complex networks (Fig. 8A). The contact between pseudotachylites and the country rocks is generally sharp, in some cases, highly irregular. This is the same as that observed in field and hand samples. In some samples, where the new pseudotachylite veins are injected in the old pseudotachylite veins, the contact between these two veins is also sharp and irregular locally (Fig. 8B,). This mode indicates that the pseudotachylite-generated events occurred repeatedly in the same location.

Pseudotachylites are composed of a fine-grained matrix appearing yellowish-brown to brown-dark in color, with numerous rounded or sub-rounded fragments which have come from the country rock. The fine-grained matrix varies from aphanitic, crystalline, microlitic to glass or glassy characters when viewed under the microscope and generally show flow structures. The details are described as follows.

## IV-2. Matrices

Microstructurally, the matrix can be divided into five types by the textures observed under the microscope, the SEM-EDX and from powder X-ray diffraction patterns (described in Chapter-V). There are: glass type (Type-I), cryptocrystalline type (Type-II), microcrystalline type (Type-III), microlitic type (Type-IV) and mixed type (Type-V).

Type-I (glass type): this type of matrix is nearly isotropic under the microscope and variable in color from brown to yellowish brown. It is locally transparent or translucent, and exhibits the optical character of glasses in volcanic rocks (Fig. 9A). The transparent and translucent glass matrix which often occur around the quartz fragments came from the host rocks. Some occur as pockets or slight streaks parallel to the flow streaks in pseudotachylite veins. These consist of pure silica or feldspar component in chemical composition (described in Chapter V). Powder X-ray diffraction data show that the Type-I matrix consist of almost entirely glass or glassy material. In hand samples, it exhibits a very obvious vitreous luster, like that of obsidian.

Type-II (cryptocrystalline type): this type matrix is composed of fine-grained material which is too small to be recognized and separately distinguished, even under the microscope. However, powder X-ray diffraction patterns show that the matrix mostly consists of fine-grained crystals. Using the ordinary thickness of thin section, the matrix appears opaque, from which nothing can be observed. The matrix generally appears brown to brown-black in color (Fig. 9B). No vitreous luster can be observed in this type matrix in hand samples even for a freshly exposed surface.

Type-III (microcrystalline type): the matrix is mainly composed of very fine-grained crystals with some small microlites which can be recognized under the microscope (Fig. 9C). The crystals however are so small that the mineral type can not be identified under the microscope. The matrix varies in color from transparent to brown to brown-black, and some appear transparent or translucent and opaque. Powder X-ray diffraction date show that the matrix mostly consists of crystals.

Type-IV (microlitic type): the microlitic matrix mostly consists of microlites which range from a few microns to a few hundred microns in size (Fig. 9D). The microlites show a variety of morphologies resembling that of microlites found in volcanic rocks. However only plagioclases can be identified under the microscope as most of the other minerals are too small to be identified. The details about microlites are described in later.

Type-V (mixed type): the matrix shows a character between Type-I and Type-III, and is optically unisotropic. Powder X-ray data also show a mixed character between glass and microcrystalline type veins.

The glass and crystalline matrices form separate single veins, and often occupies the marginal zones of microcrystalline, microlitic and mixed type veins.

### IV-3. Microlites

The microlites in the Fuyun pseudotachylites show a wide variety of simple and complex morphologies. The microlites can be divided into four morphological groups: (1) simple shape group, (2) skeletal group, (3)

dendritic group and (4) spherulitic group. These are summarized in Tables 1,2,3 and sketched in Figs. 10, 11.

The microlites vary their sizes and morphologies from the margin to the center of the microcrystalline pseudotachylite vein as shown in Fig. 12A. In the marginal zones where the matrix generally is glass or glassy, appearing opaque under the microscope (Fig. 12B), the microlites are generally small in size, being single crystals, and simple in shape, for instance spiculate and granular. They are usually arranged parallel to the flow lamellae of matrix. Toward the center of pseudotachylite vein, the microlites of single crystal become progressively larger in size and the morphologies become complex ranging from simple shape to skeletal, dendritic and spherulitic shapes (Fig. 12C). In the mixed type pseudotachylite, the single crystal or crystal fiber generally ranging from 1 to 3 microns is smaller than that occurring in the center of the microcrystalline and microlitic pseudotachylite veins. The textural variations from the margin to the center within the pseudotachylite veins are very similar to those of intruded igneous dikes from the chilled margin to the center of the dike. The details of these four group microlites are described as follows.

*Simple shape group*

This group of microlites are relatively simple in morphology, appearing spiculate, granular, trichitic, crossed, acicular-lathy, and spider-like in form (Fig. 10). The microlites of this group vary in size from a few microns to 15 microns in diameter and a few microns to

150 microns in the length of a single crystal or crystal fiber. The main characteristics are summarized in Table 1.

The spiculate microlites are generally distributed near the margin in the mixed type and microcrystalline type pseudotachylite veins where the matrix is glassy or cryptocrystalline, and aligned parallel to the margin of the mixed type pseudotachylite vein (Fig. 13A). They are mainly made up of sanidine and plagioclases ($An_{30-60}$). The chemical compositions are described later.

The granular microlites occur in some concentrated local area in the microcrystalline type pseudotachylite vein where the matrix generally is rich in magnetatic component and appears opaque under the microscope. They consist of magnetatic minerals, ilmenite, some hornblende and spinel. They are never larger than 10 microns in diameter.

The trichitic and spider-like microlites only occur in the glass matrix near the marginal zones of the mixed type pseudotachylite vein. The spider-like microlites consist of two parts: the body part similar to the spiculate microlites and the claws part similar to trichitic microlites (Fig. 13B, C). In the area where the flow lamellae of pseudotachylites were well developed, the spider-like and trichitic microlites are often arranged parallel to the flow lamellae and forming microlite rows which also run parallel to the flow lamellae (Fig.13C). However, the body parts of some spider-like microlites are arranged parallel to the flow lamellae (Fig. 13B), but the claws parts are oblique to or perpendicular to the flow lamellae. Similar trichitic and spider-like microlites are also common in glassy volcanic rocks (Ross et al., 1962). The flow textures of the trichitic and spider-like microlites occurring in the glass matrix which are parallel to the flow lamellae of pseudotachylite veins clearly show that they

were formed by the flow of a melt during the pseudotachylite vein formation. The trichitic microlites and the claws parts of spider-like microlites are too small in size for the mineral composition to be determined. The body parts of spider-like microlites are mostly made up of sanidine and plagioclases (An>40), and generally are smaller than 5-6 microns in size.

Crossed microlites occur in the glass matrix of the mixed type pseudotachylite veins usually accompanying the spider-like microlites, and in the microlitic type pseudotachylite veins. They are mostly composed of plagioclases and rare alkali feldspars, and generally are smaller than 5-6 microns in diameter, for a single crystal, and 20 microns in length.

The acicular-lathy microlites are the commonest form of microlites in the microlitic type pseudotachylite veins, but rare in the mixed type pseudotachylite veins. They vary in size from a few microns to as large as 15 microns in diameter, and 150 microns in length. Most of them are so large that they can be observed well under the microscope. Some of them were concentrated locally and formed microlites clusters (Fig. 13D) and had overgrown on the fragments of both quartz and feldspars. These consist of alkali feldspar, plagioclases in which the twin structure can be well observed, biotite, hornblende and some opaque minerals.

*Skeletal group*

The skeletal group microlites can be divided into four main forms in morphology: tabular-skeletal, dendritic-skeletal, box-skeletal and chain-

skeletal shapes (Figs, 10, 14). They are very similar in morphology to the quench crystals in submarine basalts described by Bryan (1972).

The tabular-skeletal microlites generally are composed of some short skeletal pillarets which form a uncontinued chain (Fig. 14A). They consist mainly of hornblende, biotite, and some other opaque minerals. They range from a few microns to ten microns in size, for a single pillaret crystal, and from a few microns to 100 microns in length.

The dendritic-skeletal and the chain-skeletal microlites which are very similar to the dendritic microlites in form (Fig. 14B-D), are mainly made up of ilmenite, magnetatic minerals, biotite, hornblende and some opaque minerals.

The box-skeletal microlites show incomplete polygon in form which are cacant inside (Fig. 14C). They are almost composed of hornblende and some magnetic minerals. They range from a few microns to 10 microns in size.

*Dendritic group*

The dendritic microlites have extremely complex and highly branched dendritic forms and have seven main shapes: scoplitic, feathery, quartz feathery, plumose, fir-like, branching and pine-like (Figs. 10, 15). They range from a few microns to 20 microns in size for a single crystal or crystal fiber and from a few microns to 200 microns in length. All the dendritic microlites, except for scoplitic microlites, occur in the microcrystalline and microlitic pseudotachylite veins. The main characteristics are summarized in Table 2.

The scoplitic microlites only occur in glass matrix near the marginal zones of the mixed type pseudotachylite veins. They are composed of a number of trichites which are too small (<2-3 microns) to be determined in mineral type, but are rich in Fe content and appear opaque under the microscope.

The feathery microlites are composed of two parts: a central stalk (line) and crystal fibers radiating from one end of the central stalk (Fig. 15B). Feathery microlites vary from a few microns to 8 microns in diameter for a single crystal fiber and from 5-6 microns to 50 microns in length. They are mainly made up of biotite, hornblende, rare grossular and plagioclases.

Feathery quartz microlites are composed of many fine quartz crystal fibers which generally are smaller than 2 microns in diameter for a single crystal fiber. They radiate from the quartz fragments and form multiple feathers locally (Fig. 15B). They only occur in the microcrystalline type pseudotachylite veins generally accompanying the dendritic microlites of plagioclases.

The broomy microlites resemble the feathery varieties in form and are composed of two parts: a broomy stick which consists of plagioclases and feathery parts which are mainly made up of biotites intergrown with plagioclases radiating from the broomy stick (Fig. 15C). Usually, the twin structures of plagioclases of the broomy sticks can be observed well under the microscope. The biotites intergrown with plagioclases range from a few microns to 8 microns in diameter for a signal crystal fiber and from a few microns to 50 microns in length.

The fir-like and pine-like microlites have a general form composed of two parts: a very straight trunk and many thickets (Fig. 16A, B). The trunk generally consists of plagioclases (An>40) and the thickets consist

of biotite, hornblende and plagioclases. The thickets of fir-like microlites, overgrow on and perpendicular to the trunk of plagioclases, are very simple in shape like the acicular-lathy microlites in form. The thickets of the pine-like microlites branch and branch and form complex branches. These textures show they were generated in two or three stages. The trunk of plagioclases form in the first stage, and then the thickets of biotites and hornblendes overgrow the plagioclases in the second stage. Finally, the branched thickets once again overgrow the thickets. The trunk parts generally are larger and longer than the thickets in both width and length of a single crystal ranging from 5 microns to 20 microns in diameter and from a few microns to as long as 100-200 microns in length. The thicket parts are generally smaller than 5-6 microns in diameter and vary from 5-6 microns to 100 microns in length for a single crystal.

The branching microlites are similar in form to the thicket parts of the pine-like microlites (Fig. 16C, D). They usually occur accompanying the spherulites in the microcrystalline and microlitic pseudotachylite veins. They are composed of grossular appearing pale green or pale yellowish green in color under open nicol and hornblende. Generally, they are smaller than 6-7 microns in size and shorter than 50 microns in length for a single crystal.

*Spherulitic group*

The spherulitic microlites, occurring extensively in the Fuyun pseudotachylite veins, exhibit a wide variety of spherulitic forms. The spherulites are generally speaking bodies which are composed of an aggregate of fibrous crystals of one or more minerals radiating from a

nucleus. They can be divided into two groups according to the size of a single crystal or crystal fiber: (i) fine spherulites which are generally smaller than 5-6 microns and (ii), coarse spherulites which ranges from 5-6 microns to 15 microns. The basic spherulitic morphologies found in the pseudotachylite veins are globular, fan, bow-tie, spherulitic and spherical forms in the fine spherulite group; and sheaf, sheaves aggregate, overgrowthing, stellate, dendritic-spherulite and compound spherulitic forms in the coarse spherulite group. These are sketched in Fig. 18 and descriptions are summarized in Table 3. The spherulites are very similar to those occurring in glassy volcanic rocks, described by Lofgren (1971b) and Mackenzie et al. (1987). The globular microlites generally occur in the glass matrix near the marginal zone of mixed type pseudotachylite vein, often accompanying the spiculate microlites (Fig. 13A). They have a gradational relation between the globular form and spiculate microlitic form. It appears that the globular microlites were formed from further crystallization of the spiculate microlites. They are mainly composed of sanidine and plagioclases which are 3-6 microns in diameter. Some trichites overgrow the globular microlites.

Fig. 17(A, B) shows typical examples of the fan, bow-tie, and spherulitic spherulites. All of the fan, bow-tie and spherulitic microlites occur in a concentrated block in the glass matrix of the mixed type pseudotachylite veins. They consist of a dense mass of very fine intergrown needles of both anorthoclase and a mineral rich in Fe which may be biotite radiating from a common nucleus. The fan spherulite has either a single cone or half of a bow-tie spherulite (two cones joined at their apices) that can be gradational to spherulitic spherulites as the

oppositing fans enlarge. These spherulites generally have an irregular outline modified by adjacent crystal growth. They are generally smaller than 4-5 microns in size and shorter than 130 microns in length for a single crystal fiber.

Spherical spherulites are generally composed of (i) a central core that generally is made of the fragments of both quartz and feldspar with a rounded shape, and (ii), several (usually 3-7) concentric circle zones of very fine grained crystals zones, intergrown with very fine crystal fibers zones of biotite, radiating from a common nucleus or a central core (Fig. 17D). As shown in Fig. 17D, the spherical spherulites surrounding a rounded quartz fragment can be divided into three main zones. Zones A and C consist of the fine-grained crystals which have a composition of plagioclases (An<35). Zone B consists of small crystal fibers which are so small (<3 microns) that the mineral type can not accurately be determined, but by comparison with the total composition and the observation on the SEM-BSE (Back-scattered electron image) pictures, the fiber crystals can be inferred to be biotites. The matrices surrounded in these spherical spherulites have the compositions of clay minerals in part, such as montmorillonite and kaoline or zeolite.

Fig. 18A shows a typical example of the sheaf spherulites. The sheaf spherulite is composed of two parts: the central bar and the plumose fibers or trichites that extend from this bar into the plumes. The development of this spherulite was a two-step process. The crystal bar was formed in the first step of growth, and the plumose fibers overgrew both ends of the bar in the second step of growth. Further crystallization of the single sheaf microlite could form a complete spherulite. Fig. 18B shows the microlites grown in middle step between the sheaf and spherulite. This

texture is common in glassy rocks as described by Lofgren (1971a). The sheaves aggregate spherulites are composed of many sheaf spherulites which can be gradational to the sheaf aggregate spherulites (Fig. 18C-D). The fiber bar ranges from a few microns to 15 microns in diameter and 5-6 microns to 150 microns in length. All the sheaf and sheaves aggregate spherulite are made up of plagioclases (An30-60).

The overgrowth spherulite consists of two parts: a central core consisting of fragments of both quartz and feldspar exhibiting a usually rounded shape, and the crystal fibers radiating from the fragment and exhibiting an acicular form (Fig. 19A, B). The faces of the fragments of both quartz and feldspar in the pseudotachylite veins have acted as locations for the nucleation of microlitic overgrowths of feldspars, biotite, hornblende and some other opaque minerals. The acicular crystal fibers of the overgrowth spherulites comprise approximately between ten and thirty elongated crystals of plagioclases, biotite, and hornblende, each with different optical orientation. Fine magnetic crystals overgrown on some of the acicular crystals appear as black spots (Fig. 16B). Generally, the overgrowth spherulites show an open spherulitic form, in the sense that there is much space between individual plagioclase, biotite, and hornblende crystals. The spaces are occupied by microcrystalline matrix, or some small unoriented microlites.

The stellate spherulites are star-like aggregates of acicular crystals radiating from a central point (Fig. 19B, C). The outline of the stellate spherulites has an open spherulitic form similar to that of overgrowth spherulites. They are composed of plagioclases, biotite, hornblende, garnet and some other opaque minerals.

The dendritic spherulites are spherical aggregates of dendrites and exhibit feathery, broomy, fir-like, branching and pine-like in form radiating from a common concentric point. This is either a rounded fragment of both quartz and feldspar, or a small indetermine spot (Figs. 19D, 20A-C). The dendritic-spherulitic spherulites generally are irregular in outline, and show an open spherulitic in form similar to that of overgrowth spherulites. They are composed of plagioclase, grossular, hornblende, biotite and some opaque minerals. A single crystal or crystal fiber varies from a few microns to ten microns in diameter and as long as one hundred microns in length.

The component spherulites are mixed aggregates of acicular and trichitic microlites, spherical, overgrowth and stellate spherulites (Figs. 12B, 20D). The trichitic microlites generally overgrow the spherulites and form a trichitic microlite zone. The acicular microlites intergrowth is inside fragments of both quartz and feldspar. The spherical spherulites intergrowth is inside of the overgrowth and stellate spherulites.

### IV-4. Fragments

Fragments set in fine-grained matrix consist of mostly quartz and very rarely feldspars. Fragments of mafic minerals are extremely rare, a feature characteristic of all pseudotachylites. Near marginal zones of the vein, locally fragments of biotites can occasionally be observed but only by SEM-EDX analysis.

Fragments of quartz commonly have rims showing some transparent or translucent in the glass type vein (Fig. 21A, B) and zoned structures in the microlitic vein (Fig. 17C,D). The transparent rims around fragments of

quartz are isotropic and have a glass characteristic optically similar to the thin section glass. Sometimes, it is very difficult to distinguish the transparent rim and the thin section glass. The transparent rims mainly consist of pure silica and some feldspar components in chemical composition (shown in Chapter V). The zoned rims are composed of fine microlites which only can be observed by SEM-EDX analysis.

Around the fragments of quartz, some opaque material, generally rich in iron, forms a spindle in a shape resembling the pressure shadow observed in mylonitic rocks, arranged parallel to the flow structures (Figs. 16C, 28D).

The rims are variable in width, ranging from a narrow submicron zone, which represents only a small fraction of the total bulk of the grain, to a wide zone which represents most of it.

In appearance fragments generally have a variety of shapes, such as being rounded, embayed and other irregular outlines. The rounded shapes are the most common and are described in more detail later.

The volume percent of fragments larger than 2 microns in size in pseudotachylites were measured and calculated under the microscope and from SEM-BSE photographs by using the measurement method of Shimamoto & Nagahama (1991). Three type veins, type-I, III, V were measured. The results obtained show that the volume percent of fragments in type-I, III and V is 10%, 14% and 16% respectively.

The fragments are generally described as angular to subangular and rounded in shape. In order to quantify the degree of rounding, the Roundness (Ro) (Wadell, 1932) expressing the degree of rounding is used here. Ro is defined by

$$Ro = \sum_{i=1}^{n} ri/nR$$

where ri is the radius of curvature of the corner and R is the radius of the maximum inscribed circle in the plane of measurement as shown in Fig. 22. The larger the roundness (Ro), the better is the degree of rounding. The maximum value for Ro is 1.000 for particle of maximum roundness in the given plane.

The quartz fragments remaining in the Fuyun pseudotachylites were selected for measurement because quartz crystals are very difficult to erode. About one hundred fragments of quartz which are larger than 10 um in diameter, were measured in one area on the SEM-BSE photographs.

The values obtained show that the grains of Ro > 0.5 represent more than 80% of the total grains measured in the Fuyun pseudotachylites (Fig. 23). The Fuyun pseudotachylites were generated under brittle deformation conditions, therefore, there has been no ductile deformation to round the porphyroclasts as in the case of the mylonites. The rounding of fragments in pseudotachylites is generally thought to be formed by melting during pseudotachylite formation (Sibson, 1975). The mechanism of rounding are discussed in more detail in Chapter VIII.

### IV-5. Flow structures

Flow structures generally show a alteration of thin colored layers (Figs. 9C, 13, 18D, 21C-D) and streaks which curve around the fragments (Fig. 21C-D). The changes of color mainly reflect the non-uniform chemical

composition of the matrix. This is described later. The flow streaks are concentrated close to the fragments in a similar way to that of water flowing around large gravels in a river (Fig. 21C-D). Flow streaks are frequently parallel to the margins of pseudotachylite vein. The fragments are generally arranged parallel to the flow streaks (Fig. 21C-D).

Some flow structures are very similar to the similar-fold in shape, in which the flow streaks bend in the center of pseudotachylite vein and become straight flow streaks parallel to the margins, near the margins of pseudotachylite vein. The intervals between the flow streaks become progressively larger close to the center of vein as shown in Fig. 21C. The convex directions indicate the flowing sense of melt during pseudotachylite formation. The difference in intervals between the flow streaks in margins and that in center of the vein can be attributed to a difference of flow velocities of the melt between the center and the margins of a vein. The flow velocity of melt in the center of a vein is larger than that at the margins.

### IV-6. Vesicles and amygdules

Vesicles and amygdules are frequently present in the Fuyun pseudotachylites. The volume proportion of vesicles and amygdules varies from the marginal zone to the center of a 1-2 cm thick vein, ranging from 1% to 5%, with an average value of 3%. The vesicles and amygdules generally show almost perfectly circular, although some are elliptical in shape, and vary from a few microns to a few ten of microns in size. Locally, the amygdules partially overlap each other and form a imperfect circular shape (Fig. 24A, C, E). The boundary between the

matrix and amygdules or vesicles is sharp when viewed under the microscope and on SEM-BSE photographs (Fig. 24B, F).

Most of vesicles have been filled with carbonate (the gray color in Fig. 24F) and an iron-rich material (white color in Fig. 24F) which can be recognized under the microscope and on SEM-BSE photographs as shown in Fig. 24. The amygdules often show a zoned structure formed by the filled fine material (Fig. 24D). The marginal and central zones have a carbonate-rich character while and the middle zone is rich in iron component (Fig. 24D, E). It is possible that this zoned structure was formed in different stages by underground water. Along some microfractures, filled by carbonate which cut the pseudotachylite vein, the amygdules are also only filled by carbonate and are connected with the microstructures (the white color part in Fig. 24B). This indicates that both filled structures were formed by coeval filling of carbonate with the same material source, after pseudotachylite formation.

# CHAPTER V. POWDER X-RAY AND CHEMICAL COMPOSITION ANALYSES

## V-1. Powder X-ray analyses

### *Experimental procedure*

The MXP SCIENCE X-ray diffractometer was used to obtain the diffraction patterns. The experimental conditions are as follows: filtered CuKα (1.54050 Å) radiation, X-ray generator 3 KW, 40 KV, 20 mA, sampling width 0.020 degree, scanning speed 3.0 degree per minute, divergence slit, 1.0 degree, scattering slit 1.0 degree, receiving slit 0.15 mm, θ position 5.0 degree.

In order to obtain a pure glass sample as a calibration substance for quantitative analysis of pseudotachylites, one of the granitic country rocks in which the glass type pseudotachylite occurred was completely fused at 1500 °C for one day and quenched by water. The textures of the fused glass were observed and chemical composition was measured by JSM 804 SEM apparatus with energy dispersive X-ray (EDX) analysis LINK system type AN10/50.

### *X-ray diffraction patterns*

**Diffraction patterns of calibration substances**

The artificially-generated glass fused from the granitic country rock and the granitic country rock were used as standard samples of calibration substance. It was observed by SEM-EDX that there are some vesicles and that no fragment remained in the fused glass. The chemical compositions of the fused glass analyzed by EDX were also the same as that of granitic country rock. This indicates that the rock powders were completely melted.

Six standard samples which are made up of 5, 10, 20, 50 weight percent granitic country rock, complete glass and complete crystalline granitic country rock respectively were prepared by weighing and mixing the powders.

The X-ray diffraction spectra of six standard samples are shown in Fig. 25, and one spectrum of volcanic glass (obsidian taken from the Watatoge volcanic region, central Japan) is also shown for comparison (Fig. 26a). The X-ray diffraction patterns show a very broad band ranging from 2θ 12°to 42° in the spectra (Fig. 25c-g) which are very similar to that of volcanic glass shown in Fig. 26a. It was found that the integrated intensity (Ig) of glass fraction diffraction (broad band) which is the area of oblique line as sketched in Fig. 25a increases with the increase of amount of glass. This will be discussed in more detail later.

It was found that crystalline peaks mainly consist of these of quartz, feldspars and some micas which were also recognized under the microscope. The scattered intensity of peaks in the same 2θ position decreases with the increase in the amount of glass. The peaks of quartz and feldspars can be recognized even if the amount of crystalline material of granitic rock is as little as 5 weight percent, and the peaks of micas can only be recognized when the amount of crystalline material is more than

10 weight percent. This means that if 10 weight percent of the crystalline granitic rock remained in glass, all the quartz, feldspars and micas can be recognized from X-ray diffraction pattern.

**Diffraction patterns of pseudotachylites**

Five type pseudotachylite veins were collected after a careful observation under the microscope. It is impossible to get a pure pseudotachylite matrix free from the fragments. Therefore, the collected samples of pseudotachylites contain both matrix and fragments.

The X-ray diffraction spectra of five type pseudotachylites from the Fuyun fault zone are shown in Fig. 26. All these X-ray diffraction patterns show a very broad band ranging from $2\theta$ 12° to 42° similar to that of standard samples and volcanic glass shown in Fig. 25 (a, c-g). It was also found that the integrated intensity of glass or non-crystalline material (the area of broad band) in the glass pseudotachylite (type-I), as shown in Fig. 26b, is the largest, and that of the mixed type pseudotachylite (type-V), as shown in Fig. 26c, is between that of type-I and type-II, III, IV pseudotachylites. This means that the amount of glass or non-crystal material is the largest in type-I pseudotachylite, and second largest in type-V pseudotachylite. This result is consistent with that of observation under the microscope stated above.

The crystalline peaks in the type-IV pseudotachylites mainly consist of those of quartz, feldspars and a small micas (Fig. 26c). The X-ray spectra of type-II-IV pseudotachylites show that the intensity scattered by micas is weaker then that of granitic country rock shown in Fig.25 b. The spectrum b (Fig. 26) (glass pseudotachylite) shows that there are only

quartz peaks, and no feldspars and micas peaks, which is consistent with that of the observation under the microscope stated above. The absence of micas and feldspars in glass pseudotachylite indicates that they were preferentially fused during melting. It is possible that all or some of the micas and feldspars in the type-II-IV pseudotachylites were formed by crystallization during the pseudotachylite formation.

In order to compare the Fuyun pseudotachylites with other pseudotachylites, the Outer Harry Hebrides and the Musgrave pseudotachylites, which have been well known to be composed of almost entirely fine crystalline matrix and fragments (Macaudiere et al., 1985; Wenk, 1978), were also analyzed by powder X-ray. The X-ray diffraction patterns show that these two pseudotachylites consist of complete crystalline material with rare glass or glassy material (Fig. 27). The crystalline material can be seen to mainly consist of quartz and feldspars from the characteristics of crystalline peaks in the spectra as shown in Fig. 27. These results are consistent with that of TEM analyses made by Macaudiere et al (1985) and Wenk (1978).

### *Quantitative analysis of glass and crystalline fractions*

#### Crystalline and glass matrix content

As shown in Fig. 26, the pseudotachylites produce diffraction patterns containing a broad band and some sharp peaks. These observations are explained by the presence of both crystalline and glass matrices in these pseudotachylites.

It is well known that (i) the total integrated intensity is a constant which is independent of the quantity of crystalline and non-crystalline material and that (ii) the integrated intensity of crystalline material increases with the increase in amount of crystalline material and (iii) the integrated intensity of the glass matrix increases with the content of glass in a material having constant chemical composition (Klug & Alexander, 1954). Therefore, the calibration curves can be obtained by measuring the integrated intensity scattered by non-crystalline or crystalline material in the spectra of the calibration substances, and then quantitative analysis of crystalline and non-crystalline material can be carried out for the test samples.

The integrated intensity of glass fractions in standard samples were measured using the triangle approximate method as shown in Fig. 25 a. The measured data were plotted in the diagram showing the relation between the integrated intensity of glass and the amount of glass (Fig. 28). It is clearly shown that the integrated intensity of glass increases with the amount of glass as a form of linear function:

$$Ig = K\ Wg \quad \text{.....(1)}$$

Ig: integrated intensity of glass or noncrystalline material,

K: coefficient depending on the composition of rock,

Wg: weight percent of glass in measured material.

This curve is used as a calibration curve.

The integrated intensity of glass fractions in the pseudotachylites was measured also using the triangle approximate method as shown in Fig. 25 a and plotted in the calibration curve shown in Fig. 28. The amounts of glass read directly from the calibration curve and calculated using the formula (1) vary from a few weight percent in type-II-V pseudotachylites to as much as 89 weight percent in type-I pseudotachylite. The fragments producing the sharp crystalline peaks represent only 11 weight percent in the glass pseudotachylite. It is possible that the crystalline material contained in type-II-V pseudotachylite veins consists of the relicts of fragments from the granitic country rocks and microlites formed from melt, as well some clay minerals.

**Crystalline material**

As shown in Fig. 25, the scattered intensities of quartz, feldspars and micas peaks in the same 2θ position increase with the increasing amount of crystalline material. In order to determine quantitatively the relation between the scattered intensity and amount of crystalline material, the intensities of quartz peaks in the same 2θ position in the standard samples were measured, as shown in Fig. 25 a, and the results were plotted in the diagram showing the relation between intensity and weight percent of standard samples (Fig. 29). It was also found that the intensity of quartz peaks in the same 2θ position increases with the increase in amount of crystalline material as a form of linear function:

$$Iq = K\ Wq \quad \text{.....(2)}$$

Iq: intensity of quartz in the same 2θ

K: coefficient depending on the composition of rock,

Wq: weight percent of quartz, the total amount of quartz contained in country rock is used as 100 weight percent.

Using this calibration curve, the amount of minerals such as quartz, feldspars and micas respectively contained in country rocks and remaining in the pseudotachylites can be quantitatively determined.

The intensities of quartz peaks in the same 2θ 26-27° position in the type-I-V pseudotachylites were measured and the results were plotted in the calibration curve shown in Fig. 29a. It was read directly that the amount of quartz is 34 weight percent in the glass type pseudotachylite, and 28-80 weight percent in the type II-IV pseudotachylites using total quartz contained in the granitic country rock as 100 weight percent. This means that 66 weight percent quartz was melted in the glass pseudotachylite during the pseudotachylite formation.

In the same way, the calibration curve for feldspars was also obtained by measuring the intensity of the peaks of 2θ (albite peak) 27.5-28° positions, and the amount of feldspars contained in the pseudotachylites was determined as shown in Fig. 29a. It has been known from observation under the optical microscope and SEM-EDX as stated above that the feldspars consist of fragments and microlites in the type-II-IV pseudotachylites which are composed of complicated solid solution. The weight percentages varying from 17 to 72, therefore, there is a mixed amount of some feldspars, which shows clearly the difference in feldspars

between the pseudotachylites and country rocks. There are no feldspar peaks in the glass type pseudotachylite.

As stated above, the volume percentages of fragments remaining in the pseudotachylites is about 10 volume percent corresponding to 10 weight percent (using an average density of 2.70 g/cm$^3$ for quartz, and granitic country rock) in the glass pseudotachylite. This is consistent with the results of the quantitative analysis from the X-ray diffraction data. The amount of glass fraction in the type-II-V pseudotachylites varies from a few weight percent to 34 weight percent can be explained by the fact that the crystallization was advanced in the original melt and only some melt was quenched to form the glass during the pseudotachylite formation. The presence of microlites as high temperature indicators such as sanidine, anorthoclase, pyroxene, grossular and amphibole and biotite with high Ti component, which are not present in the granitic country rock also demonstrates that they were crystallized originally from melt by frictional melting and only some of melt was quenched and remained as glass.

## V-2. Chemical compositions

### *Pseudotachylite and country rock chemistry*

The average bulk chemical compositions of pseudotachylites and the associated country rocks analyzed by XRF on ignited dry material are shown in Tables 4 and 5. The water contents were determined independently by ignition loss which were corrected for oxidation of iron using the FeO contents as shown in Tables 4 and 5. The analyses of glassy

matrices of pseudotachylites were carried out by SEM-EDX and are given in Tables 6 and 7.

Shand (1916) was the first to note that pseudotachylites have a composition similar to the rocks in which they occur. The average bulk compositions of pseudotachylite veins including fine-grained matrix and fragments of country rocks are also very similar to those of the country rocks in the Fuyun fault zone. The variations in main oxides such as $SiO_2$, $Na_2O$, FeO, MgO, CaO, $Na_2O$ and $K_2O$ between the pseudotachylite veins and the country rocks are not so clear (Fig. 30). It is doubtlessly shown that the pseudotachylites have been formed from the rocks in which they occur from this similarity between the chemical composition of the pseudotachylites and the country rocks and the field occurrences.

Pseudotachylites are, in general, chemically very heterogeneous, not only from vein to vein, but also in different parts of a single vein as shown in Fig. 31. The chemical heterogeneity in pseudotachylite is also described in the literature (Ermanovics et al., 1971; Masch et al., 1985; Toyoshima, 1990). Although there is similarity in chemical composition between the pseudotachylite veins and the country rocks, there is, in general, a significant change in composition between the fine-grained matrix -glass matrix and the country rocks. As shown in Fig. 31, the glass matrices in type-I and V veins are generally poorer in $SiO_2$ component than those of the country rocks, except for local pure $SiO_2$ composition glass. The average weight percentage in $SiO_2$ component is 60-64 Wt.% in glass matrices which are about 10 Wt.% poorer than that of the country rocks. The chemical compositions of glass matrices represent the initial compositions of the melt formed during pseudotachylite formation. The poorness of $SiO_2$ component in glass

matrix indicates that some quartz crystals remained as fragments in pseudotachylite veins, so that the glass matrices have a lower $SiO_2$ component than those in the country rocks.

The glass matrices are generally 3-5 Wt.% higher in $Al_2O_3$ than those of the country rocks, and have a component range of feldspars contained in country rocks. Locally the transparent glass has a plagioclase (albite) composition (Fig. 32). There is generally a gently increasing tendency in CaO and $K_2O$ contents from the country rocks, pseudotachylite veins to glass matrices. FeO and MgO components are also higher in glass matrices than those of the country rocks.

As stated previously, the fragments remaining in the glass pseudotachylite veins are almost entirely quartz, although the feldspars and biotite are main rock-forming minerals in the granitic country rocks. The low $SiO_2$ and high $Al_2O_3$ and high CaO, $K_2O$, FeO and MgO natures of the chemical composition of glass matrices indicate that the melt was formed by the preferential melting of biotite and feldspars rather than total melting of the country rocks.

The flow layers and streaks in the glass matrix, showing a variation in color, mainly reflect the change of chemical composition in mafic components such as FeO and MgO. The total component of oxides FeO and MgO ranges from 0.5 Wt.% to 15 Wt.% from the transparent, translucent to opaque layers or streaks. This indicates the melt formed by the fusion of single mineral had flowed but was not sufficiently mixed.

In the type-IV vein, where the biotite microlites occur, the fine-grained matrix around or near the microlites has a composition similar to that of biotite (Table 8, Column Ma1). Where the plagioclase microlites occur,

the fine-grained matrix around or near the microlites has a composition similar to that of plagioclase (Table 8, Columns Ma2-Ma5).

This concentration of mineral-forming elements also occur in the zoned structures around the fragments as shown in Figs. 17C-D. The zone a contacting with the fragment and zone c have a composition similar to that of plagioclase (Table 8, Columns 6,7), and the zone **b** has a composition similar to that of biotite (Table 8, Column 9). A similar zoned structure around quartz xenocrysts, called a corona, is common in basalt or andesitic volcanic rocks (Sato, 1975). The formation of these coronas around the fragments are explained by the preferred crystallization of some minerals in a melt and by a diffusion model (Sato, 1975). It is possible that the coronas which consist of a glassy or fine-grained matrix in pseudotachylites could also be explained in terms of concentration of some elements tending to preferentially crystallize.

The water contents in the pseudotachylite veins and country rocks are shown in Tables 4, 5 and Fig. 33. Here the crystalline water ($H_2O^+$) and fractured water ($H_2O^-$) were measured respectively independently by ignition loss. The crystalline water ($H_2O^+$) contents in type-I--V veins have a small variation range between 2.0-2.65 Wt.%. These are 1.5-2.0 Wt.% higher than that of the country rocks which contain about 0.5 wt.% ($H_2O^+$) as shown in Fig. 33. As stated previously, the glass matrices, in which the vesicles and amygdules are frequently present, were not metamorphosed. Therefore, it can be supposed that the crystalline water contents in type-I and V veins represent the initial water contents entering the melt as hydroxyl ions formed by quenching of the melt. These high crystalline water contents and the presence of vesicles and amygdules indicates that the melting took place under water-saturated

conditions rather than dry conditions. The water-saturated condition demonstrates that some water was previously present in fractures in the country rock.

### *Microlite chemistry*

#### Feldspars

The feldspar compositions of the microlites and fragments analyzed by EDX method are shown in Tables 9-17 and plotted on the An-Ab-Or diagram in Fig. 34. The plagioclase microlites have a much larger compositional range, from albite to betonite ($An_{17}$-$An_{70}$). The plagioclase fragments all fall within a small range of oligoclase composition ($An_{21}$-$An_{29}$). The alkali feldspar microlites vary widely in compositional range from $Or_{17}$ to $Or_{93}$ which are the compositions of anorthoclases, sanidines and probably some orthoclases and microclines. The anorthoclase microlites have high Fe content (up to 4.87 wt.% FeO*) (Table 9). By the observation of the BSE picture, it is very clear that the fine biotite microlites have intergrown within the anorthoclase. It is probable that some of the compositions of the intergrown biotite which were analyzed were mixed with anorthoclase microlites in composition, and therefore show high Fe content in the measured compositions of anorthoclase microlites. The alkali feldspar fragments all fall within a small range of microcline composition ($Or_{89}$-$Or_{97}$), which also can be recognized optically under the microscope. All the plagioclases comprise albite ($An<30$) as shown in Tables 16 and 17. The presence of anorthoclase, sanidine and plagioclases of high An content ($An_{40}$-$An_{70}$)

microlites, which are not present in the country rocks, indicates that these microlites were formed under higher temperature conditions than that of the country rocks.

### Biotites

The biotite microlites usually occur with hornblende and plagioclase microlites and show acicular-lathy in form in the microlitic and microcrystalline pseudotachylite veins. Most of biotite microlites have higher Ti content than in fragments (Tables 18, 19 and 20, Fig. 35A). The presence of the high Ti content of biotites may be the indication of high water content and high temperature.

### Hornblendes

The hornblende microlites often show skeletal and spherulitic forms. The hornblende microlites usually have higher Ti content than those of fragments, as shown in Tables 21 and 22 and Fig. 35B. The presence of hornblende microlites with high Ti content also indicate that these microlites were formed under high water content and high temperature conditions.

### Pyroxenes

The pyroxene microlites usually occur in the center of the microlitic pseudotachylite veins as dendritic and spherulitic forms. All the pyroxene microlites usually have low Ca and extraordinarily high Al

contents (Table 23), and fall within the compositional range of clinohyperthene and magnesian pigenite (Fig. 36). Extraordinarily high Al contents of the pyroxene microlites were also reported in the microlites in the Hidaka pseudotachylites and suggested to be formed by nonequilibrium crystallization of a melt (Toyoshima, 1990). The acicular and dendritic pyroxene microlites also often occur in volcanic glassy rocks (Ross, 1962; Lofgren, 1971a; Bryan, 1972; Shiraki and Kuroda, 1977) and lunar rocks (Lofgren, 1971a). The high Al contents and the presence of the dendritic and spherulitic pyroxene microlites in the pseudotachylites indicate clearly that the pseudotachylites were formed by the quenching of a melt.

**Garnets**

All the garnet microlites fall within the compositional range of grossular and have low Ca contents (Table 24, Fig. 37). Generally the garnet microlites occur coexisting with the pyroxene microlites and show dendritic-spherulitic forms.

**Ilmenits**

The chemical composition of the ilmenite microlites are shown in Table 25. The ilmenite microlites often occur coexisting with the biotite, spinel, and magnetic mineral microlites and show dendritic-skeletal forms.

**Spinel, apatite and magnetic minerals**

The spinel, apatite and magnetic mineral microlites rarely occur rarely, coexisting generally with the ilmenite microlites and are granular in form. The chemical compositions are given in Table 25.

# CHAPTER VI. EXPERIMENTALLY-GENERATED PSEUDOTACHYLITES IN GABBROS AND GRANITES

## VI-1. Experimental conditions and procedure

The descriptions in preceding chapters demonstrate that the Fuyun pseudotachylites were formed by frictional melting on fault plane during seismic fault motion. In order to understand the mechanical mechanism and melting process of the fault-generated pseudotachylite formation, in this part of the programme, high-speed frictional experiments have been conducted. on two types of rocks. The first type are quartz-rich rock consisting of fine-grained and medium-coarse grained granitic rocks coming from India and an unknown area. The other type are quartz-poor rocks which are fine-grained and medium-gained gabbros from South Africa. The fine-grained and medium-grained granitic rocks are mainly composed of quartz, feldspars and biotite. The coarse-grained granite mainly consists of quartz, feldspars and pyroxenes. The gabbros mainly consist of pyroxenes, plagioclases, micas and very rarely quartz. Many pseudotachylites found in the world so far occur in quartz-rich granitic rocks, therefore, conducting high-speed frictional experiments in granitic rocks would provide important information in understanding the mechanical mechanism and process during which natural pseudotachylite forms. The reason for using the gabbros is to understand the mechanism of frictional melting in quartz-poor and hydrous minerals-rich rocks.

The rotary-shear high-speed test machine was designed by Dr. Toshihiko Shimamoto of the Earthquake Research Institute, University of Tokyo for understanding the high speed frictional property of rocks in fault zones (Fig. 38A). Friction is generated on the interface by rotating one cylindrical sample against another under an axial pressure. The machine is capable of producing slip rates of up to 2 m/s, corresponding to the revolution rate of 1,500 r.p.m., under the axial forces of up to 1 tonne. Thus a normal stress up to 100 MPa, which is close to the uniaxial strengths of most rocks, can be applied if anvil-shaped samples are used. Observation of the experiment can be made through the transparent window cover as shown in Fig. 38B.

The variations of displacement, axial load, temperature of the frictional surface, light intensity of light emitted during the slip and torque during experiment are automatically recorded using an 8 channel recorder. However, the friction at the thrust bearing, the axial load, tured out to be large, so that the reliable measurements of friction could not be made in the present study. Hence only the textures and chemistry of experimentally produced pseudotachylites will be treated in this paper.

Cylindrical samples between 4.80-5.00 cm in length and 2.45-2.50 cm in diameter were prepared. No through-going fracture could be observed either by the naked eye or under the microscope for all the cylinder samples used in these experiments. The faces of the cylinders were polished on wattled glass with F1200 Aloxite powder, and the faces were made completely square to the length. The samples were washed for about 20 minutes by an ultrasonic cleaner and dried at room temperature.

Two cylindrical samples were set in the steel holders and adjusted to come into complete contact. The faces were then rotated against each

other, for 10-15s for the samples of granitic rocks and 20-40s for the gabbro samples, at 1200-1500 r.p.m. and at axial loads of 50-75kg. This corresponds to a velocity of 0.75-1.90 m/s and a mean normal stress of 10-15 bars (1-1.5 MPa). This is similar to the conditions of a fault zone at 40-70 m depth during seismic faulting of a large earthquake.

After deformation, the two facing parts of the cylindrical samples with intact pseudotachylite veins were indurated with petropoxy for the two gabbro experiments in order to observe the original morphology and textures of pseudotachylite veins. Sections were cut normal to the sliding surface and subparallel to the sliding direction.

In all the experiments, some of the melt generated by frictional heating was squeezed out from the shear zone. The melt products of four samples, two fine-grained gabbros, the other two samples are fine-grained and medium granitic rocks, were picked up for analysis by X-ray powder diffraction and some flacks were polished for analyzing the textures and chemical composition by SEM-EDX.

In order to obtain the pure glass sample as a calibration substance for quantitative analysis of pseudotachylites, the gabbro and granitic rocks were completely fused at 1500 °C for one day and quenched by water. The experimental conditions of X-ray diffraction pattern analysis are the same as that described in Chapter V.

## VI-2. Experimentally-generated pseudotachylites

### *Microstructures in gabbro-pseudotachylites*

In the high-speed frictional experiments of gabbros, it was observed that the sparks and dust began to come off within a few seconds after the initiation of fault motion in all directions from the interface of shear zone and this continued to the end of experiment (Fig. 38B). The interface glowed sherry red after 5-7 s starting and a pungent burnt rock smeech was smelled. 9-11 s after starting, a cherry red melt was extruded out from the interface, in the form of needles or small sticks with some branches, which continued until the end of experiment.

Two cylindrical samples were separated as soon as the experiment ended, and the original shear surfaces and the fused layer were examined under the stereoscopic microscope and SEM-EDX. In one experiment, the cylinder samples were not separated after the experiment ended, so the two cylinders were cemented to each other by the melt. Therefore, the original texture of the melt zone normal to the shear zone could be examined under the microscope and electron microscope on cemented sample.

An overall view of one shear surface is shown in Fig. 39A. The circular shear surface can be divided into three distinct ring zones by its textures: a central zone, a middle zone and an edge zone (Fig. 39B). The central zone and edge zone are the areas of built up of fragments cemented with a little melt material and shows a glass luster locally. The middle zone occupies about half the radius of the circular surface and shows a typical morphology of fresh lava, exhibiting vesicular, cavities and roughness like a ploughed field and is black in color. This indicates that the cataclastic deformation is the main mechanism of deformation at the central and edge zones, and frictional melting is the main mechanism at the middle zone. This can be explained as the displacement rate was too small

to generate enough heat to melt the rock at the central zone and the heat generated escaped so quickly that the temperature could not increase sufficiently to melt the rock at the edge zone where the rock contact directly with air. Frictional melting was achieved mainly at the middle zone where the displacement rate was large enough to generate heat and the temperature was sufficient to melt the rock within a short time of a few to a few ten seconds. The most striking feature of the shear surface morphology is its flow structures, vesicular, relative roughness and glass luster (Fig. 40A-C).

SEM-BSE photomicrographs of a polished section cut normal to the gabbro cylinder surface and sub-parallel to the edge of circular surface are shown in Fig. 41A-C. It can be clearly observed that there is a main fused zone exhibiting as a single vein parallel to the shear zone, ranging from a few microns to 120 microns in width, and branched veinlets, ranging from submicrons to a few ten microns in width appearing as a single vein and complex networks injected into the host gabbro. The modes which are very similar to the fault veins and injection veins in the fault-generated pseudotachylites described by Sibson (1975) and have been successfully simulated. The main fused zone has irregular boundaries with the host gabbros and pinch and swell along the shear zone. In contrast to main fused zone, the branching veins tend to be far less regular in form and generally much thinner, being submicron in width. The injected veins progressively ramify through the host gabbros and up to several millimeters from the shear zone along the fractures generated during the rapid frictional experiment. Generally they can be traced to the shear zone. The injected vein generally is wider near the branching point, from

where the fracture shows a tension crack feature, than that far from the branching point.

The fused layer mainly comprises sub-angular to rounded porphyroclasts of pyroxene and feldspars derived from the host gabbros set in glass matrix (Fig. 41). Although the porphyroclasts are composite in size, they are never larger than 40 microns in diameter. The porphyroclasts tend to be aligned in a preferred direction parallel to the shear sense on the interface and in the thin section parallel to the shear sense (Fig. 41B, C). The glass matrix appears relatively homogeneous texturally. There is a uniform contrast intermediate between the bright crystalline fragments of pyroxene and the darker crystalline fragments of feldspars and a gradual color change between that of the pyroxene and that of feldspars, which are the main gabbro-forming minerals in the BSE photographs (Figs. 41B, 42). Locally, they have a color of feldspars or pyroxene in BSE photographs. Most vesicles are spherical, but some are ellipsoid, generally with diameter smaller than 50 microns. No crystallines, such as microlites formed from the melt, as described by Spray (1988), can be observed in this fused material.

### *Microstructures in granite-pseudotachylites*

Three type granitic rocks were used in this experiments: fine, medium and coarse-grained.

In the high-speed frictional experiments on granitic rocks, during the first 5-6 s, sparks and dust were produced and flung off in all direction from the interface, similar to that observed in the gabbro experiments, described above. 7-9 s after starting, the interface glowed cherry red and

a partial cherry melt flew out from the shear zone. Meanwhile, some fragments ranging from a few microns to one centimeter in size, burst and the cylinders near the interface completely disintegrated.

It is very difficult to obtain a sample to make thin section cut normal to the interface because the samples had disintegrated in these granite experiments. One circular product was obtained consisting of fragments from the granitic hot rock ranging from submicrons to a few millimeters in size, cemented by the glass matrix. This circular product was cemented onto the granitic host rock which had been fractured into fragments with no cohesion and forming a circular ring. This was thrown out from the holder when the cylindrical samples broke during the frictional experiment. This indicates undoubtedly that the frictional melt formed before the specimens broke down in this experiment. There were only a few hair-like melt products in the coarse-grained granite samples, as observed under the stereoscope and microscope.

The frictional shear surface of a fragment was examined in plan view under the stereoscope (Fig. 43A-B). The frictional surface is very rough. Lumpy dots of material, between which irregular spaces and cavities occur, are accompanied by scored indentations of broadly concentric form.

Some biotites were fused and flowed with the shear sense on the shear surface as black bands (Fig. 43B). The transparent or translucent melts also flowed with the shear sense as fine sticks (Fig. 43A). The fused material mainly comprises angular, subangular to rounded quartz and feldspars set in a glass matrix. The flow structures can be well observed on SEM-BSE photographs (Fig. 44).

***Chemical compositions***

Bulk compositions of all the samples used in this experiments analyzed by XRF are shown in Table 26. The chemical compositions of fused material generated from gabbros and granites are described as follows.

## Gabbros

The gabbro samples used in this experiments are fine-grained and medium-grained and massive with no evidence of a tectonic fabric. The medium-grained gabbros mainly are composed of pyroxene and plagioclases, and the fine-grained gabbros mainly consist of pyroxene, plagioclases and biotite. The glass matrix in the medium-grained gabbro samples is very heterogeneous in chemical composition, most of which are different to the bulk compositions of the host rocks but similar to that of plagioclases and pyroxenes contained in the host rock of the gabbro (Table 27, Figs. 45,46). This indicates that the melts formed by the fusion of plagioclases and pyroxenes, and were not mixed, were quenched into glass.

The matrix in fine-grained gabbro sample is very homogeneous in chemical compositions having a composition similar to the average bulk composition of the host rock of gabbro (Table 28; Figs. 45, 47)

## Granites

The fused material comprises porphyroclasts of the quartz and feldspars set in glass matrix in granite samples. No biotite fragments can be found under the microscope and using SEM-EDX analysis.

The chemical compositions of all the host granitic rocks and glass matrices are shown in Tables 29-31. All the glass matrices of the fused material in the three type granitic rock samples show a common characteristic in that the matrices are a few weight percent to 30 weight percent lower in $SiO_2$ component than that of the host granitic rocks as shown in Figs. 48, 49. The poorness of $SiO_2$ components in the matrix is also found in the Fuyun pseudotachylites as described in preceding chapter. This probably shows that the glass matrix compositions formed by preferential melting of the low melt point minerals such as biotite and feldspars rather than total melting of the granitic rocks. The quartz crystals are very difficult to melt and generally remained as fragments. This is not surprising because the quartz has a high melting point up to 1723 °C which is 200-600°C higher than that of feldspars and biotite.

The chemical compositions of glass matrix in coarse granite sample are mainly concentrated in two areas: one is the composition similar to that of pyroxene, the other is similar to that of plagioclase (Fig. 48). The variation diagrams of oxides $SiO_2$, $Al_2O_3$, FeO, MgO, CaO, $Na_2O$ and $K_2O$, given in Fig. 50, also show a characteristic of two concentrated areas. This shows that the pyroxene and plagioclases both melted but remained almost unmixed.

There is also a relatively large variational range in the chemical compositions of the glass matrices in the fine-grained and medium-grained granitic rock samples (Tables 30, 31; Figs. 51, 52). The $Al_2O_3$ content is almost the same as that in the plagioclases contained in the host granitic

rocks. Generally, the FeO and MgO contents are about 2.0 Wt.% higher than those in the bulk composition of the host granitic rocks. The CaO, $Na_2O$ and $K_2O$ contents are also a little higher. In general, the chemical compositions of the matrices are very similar to that of the alkali feldspars and plagioclases contained in the host granitic rocks. The biotite has been preferentially assimilated into the melt, therefore, the glass matrix has a higher FeO and MgO contents than that of the host granitic rocks.

### VI-3. Powder X-ray diffraction analyses

In order to confirm the presence and features of the fused material obtained from the high-speed frictional experiments, four samples: two fine-grained granite and two fine-grained gabbro were elected for analyzing by powder X-ray diffraction method. The measurement conditions of the powder X-ray analysis are the same as that described in Chapter V. To obtain the pure glass samples used as a calibration substance for the quantitative analyzing, the host rocks of fine grained granites and fine-grained gabbros were fused at 1500 °C for about one day using the high-temperature furnace.

The powder X-ray diffraction spectra of the experimental pseudotachylite gabbro samples 007 and 025 and granite samples 027 and 033 are shown in Fig. 53 b, c and Fig. 54 b, c. For the sake of reference, the spectra of the host rocks of fine-grained gabbro and fine-grained granite are also shown in Fig. 53a and Fig. 54a. All the X-ray diffraction spectrograms of the melt samples exhibit a very broad band ranging from 2 $\theta$ 15° to 42° (Figs. 53b, c; 54b, c), which are very similar to those of the glass type veins in the Fuyun pseudotachylite. This is a typical diffraction

pattern of glassy volcanic rock. But, there is no broad band in the spectra of the host rocks of gabbro and granite (Figs. 53a; 54a), which clearly indicates that glass or non-crystalline material is present in these experimentally-generated pseudotachylite samples.

The peaks scattered by crystalline show the presence of the pyroxene and feldspars in gabbro melt samples, and feldspars and quartz in granite melt samples which are fragments derived from the host rocks. The integrated intensities of all peaks in the melt samples are weaker than that of their host rocks in the same 2 θ position as shown in Figs. 53, 54. This shows that crystals have partially melted into glass both in the gabbro and granite samples. The mica peaks in 2θ 9-10° position are very clearly observed in both the host rocks of gabbro and granite (Figs. 53a, 54a), but, the mica peaks can not be recognized in the X-ray spectra of four melt material samples. The disappearance of the peaks of micas crystals and the presence of other minerals which are present in the host rocks show that the micas crystals were preferentially melted into glass and the other minerals were partially melted.

***Quantitative analysis***

The X-ray diffraction data demonstrate that the glass matrices are present in the experimentally-generated pseudotachylites in gabbro and granite samples. To understand quantitatively the contents of the glass matrices, a quantitative analyses are also carried out for the experimental pseudotachylites. The principles of the quantitative analysis method and the experimental procedures are described in Chapter VI.

The standard samples are prepared by adding 10, 20, 50, 75 weight percent glass fused from the gabbro and granite respectively to the complete crystalline host rocks of gabbro and granite. Six standard samples containing 0, 10, 20, 50, 75 and 100 weight percent glass were measured for granite and gabbro respectively. The X-ray diffraction spectra of the standard samples in the gabbro and granite are shown in Figs. 55 and 56. All the spectra, except those of the host rocks of gabbro and granite samples ( no glass, Figs. 55a, 56a), show a broad band ranging from 2θ 12° to 42°, which are very similar to that of the glass vein in the Fuyun pseudotachylites. The areas of the broad bands indicate the integrated intensity generated by the glass material, which clearly increase with the contents of the glass as shown in Fig. 55 and Fig. 56 from spectra a to e. The peak intensities scattered by crystallines in the same 2θ position in these spectra decrease with an increase of the glass content.

The integrated intensities of glass (Ig) in the standard samples were measured using the method described in Chapter IV and plotted against glass content (Wg:weight percent) in the Ig-Wg diagram as shown in Figs. 57, 58. The straight lines of calibration curves were obtained by calculation, using the method of least squares (Figs. 57, 58). By fitting the calibration curve parameters into the equation for a straight line, the following relations were obtained:

$$Ig = 1.118 + 0.500\ Wg \quad \text{..... (3)}$$

for the gabbro samples and

$$Ig = -2.449 + 0.896\ Wg \quad \text{..... (4)}$$

for the granite samples. The coefficient of correlation calculated by the method of least squares from the measured date is 0.9978 for the equation (3) and 0.9982 for the equation (4).

The integrated intensities of the experimentally-generated pseudotachylite melt samples in gabbro and granite were measured and plotted in the Ig-Wg diagrams of Fig. 57 and Fig. 58 respectively. The glass contents (Wg) were calculated using equation (3) for gabbro samples 007 and 025 and equation (3) for granite samples 027 and 033. The results show that there are 44.49-52.23 weight percent glass matrix in the gabbro samples and 43.38-43.60 weight percent glass matrix in the gabbro samples. This means that there are about 50 weight percent fragments mixed in the melt material, which can be observed under the microscope and the electron microscope as stated above.

The crystals of the main minerals such as quartz and feldspars remaining in the melt material of the granite samples were also quantitatively analyzed using the method stated in chapter VI. The integrated intensity (Iq) of quartz peaks in the 2θ 27°-28° position in the spectrograms b-f shown in Fig. 55, which are the strongest in the quartz peaks were measured and plotted against the quartz content contained in the standard samples as shown in Fig. 59. Using the quartz crystal content contained in the host granite sample as 100 weight percent, and the quartz crystal content contained in complete glass standard sample as 0 percent,

the calibration curve was obtained by calculation using the method of least squares (Fig. 59), and the equation of straight line was obtained:

$$Iq = 1.29 + 0.78\ Wq \quad \text{.....(5).}$$

The coefficient of correlation is 0.988.

The Integrated intensities of the quartz peaks in the spectra shown in Fig. 58 were measured and plotted in the Iq-Wg diagram (Fig. 59). The glass contents were calculated using the equation (5). The calculated results show that there is 45.53 weight percent quartz crystalline in the sample 027 and 82.96 weight percent quartz crystalline in the sample 033.

In the same way, the calibration curve was also obtained for the feldspars (using the peaks of 2θ 26-27° position of albite crystal) from the spectra of standard samples shown in Fig. 58. The equation of a straight line was obtained:

$$If = -0.383 + 0.864\ Wf \quad \text{.....(6)}$$

The correlation coefficient is 0.995.

The integrated intensities of the peaks of albite were measured and plotted in the If-Wf diagram (Fig. 60), and the albite contents were obtained by calculation using equation (6). The results show that there is about 35 weight percent albite crystals remaining in samples 027 and 033.

The peaks of micas can be recognized in the spectra a-e of the standard samples in Fig. 55. This indicates that even if the content of the crystals in the melt material is as little as 10 weight percent (e spectrum in Fig. 55), the peaks of micas can be recognized in the spectrograms of the granite samples. There are no clear peaks of micas in the spectra of melt samples (Fig. 53b, c; 54b, c). This indicates that the micas were all or almost all melt.

The results of quantitative analyses demonstrate that the micas were melted preferentially, followed by the feldspars, but the quartz were very difficult to melt in the granites. This indicates that the frictional melting was formed by preferential melting of low melting temperature minerals such as the micas and feldspars rather than total melting of the host rocks of granites.

# CHAPTER VII. HIGH-SPEED FRICTIONAL MELTING EXPERIMENTS IN ALBITITE-QUARTZITE AND ANORTHOSITE

The studies of natural and experimental pseudotachylites described in preceding chapters demonstrate that the fault-generated pseudotachylites can be formed by frictional melting of the host rocks during seismic faulting. The results document that the melting was formed by preferential melting rather than total melting of the host rocks. But, there are no data showing whether the melting formed under equilibrium conditions or not. It is very important to determine the melting conditions during the frictional melting from mineralogical data. If the frictional melting occurs under a non-equilibrium condition, the minerals contained in the host rocks would melt at their respective melting points. This means that mineral of low melting point would melt more easily than those of high melting point to foster the preferential melting of minerals with low melting points. If the frictional melting was formed under an equilibrium condition, the rocks would melt at a relatively low temperature, lower than the melting point of a single mineral contained in the rock.

To clarify if the frictional melting is an equilibrum process or not, high-speed friction experiments have been conducted on three types of rock samples have been used: albitite, quartzite and anorthosite.

experiment. However to obtain much more melt material, the samples were rotated for a longer time, up to 40 s for the anorthosite sample.

### VII-2. Microstructures

In the high-speed frictional experiment on the albitite-quartzite pair, 6-7 s after starting, white sparks flamed and dust flew off in all directions from the interface of shear zone. This continued to the end of the experiment. 10 s after starting, the small fragments flew out from the edges of samples, meanwhile, a small cherry red melt was extruded out from the interface and quickly quenched into glass at room temperature. After 14-15 s, some large fragments, ranging from a few ten microns to 0.5 cm in size were burst, while the cylindrical samples of albitite and quartzite were completely disintegrated.

Only a little melt material formed in this experiment, the melt material being so small that it is very difficult to recognize with the naked eye. The melt material appears as translucent or transparent small pieces and hair-like or small stick-like (Fig. 61C, D), locally exhibiting a glass luster. This was picked up under the stereoscope and made into a thin section.

In the anorthosite pair experiment, 2-3 s after starting, white-yellowish color sparks were thrown out from the interface, continuing to the end of the experiment. After 4-5 s, the interface glowed cheery red. A cherry red melt material was extruded out and flew from the interface after 7-8 s, resembling a blazing fireworks, and continuing to the end of experiment. Only the edges of two cylindrical samples were damaged at the end of the experiment. The phenomena observed during the experiment are very

similar to those observed in the gabbro experiments, described in Chapter VI.

The melt material extruded from the interface appears as small pieces and fine twisted sticks or complex dendritic branches observable even with the naked eye (Fig. 61A,B). The melt material comprises many fragments with a translucent or transparent matrix exhibiting a glass cluster, with many small caves or vesicles. On the shear surfaces, flow structures parallel to the rotation direction can be found locally.

Under the electron microscope, it could be observed clearly for the albitite-quartzite pair and anorthosite samples that the fragments range from submicron to a few hundred microns and are set in the glass matrix, exhibiting angular, sub-angular to rounded in shape. The vesicles ranging from submicrons to a few ten microns in size are frequently present in the anorthosite samples. These are almost all spherical in shape, and rarely ellipsoidal.

## VII-3. Chemical compositions

### *Albitite-quartzite*

The chemical compositions of albitite, quartzite and anorthosite are given in Table 26. The albitite is composed of about 80.27 Wt.% $SiO_2$, 12.14 Wt.% $Al_2O_3$ and 6.94 Wt.% $Na_2O$, corresponding to 55 mole percent albite (Ab) and 45 mole percent quartz (Qz). The quartzite consists of almost pure $SiO_2$. The albitite-quartzite pair is made up of a albite-quartz ($NaAlSi_3O_8$-$SiO_2$) two component system, which is a binary eutectic system. Thus, the chemical composition of matrix in albitite-

quartzite samples can be plotted in the phase equilibrium diagram of the albite-silica (Ab-$SiO_2$) system Fig. 62. In this system, if the frictional melting was formed under equilibrium conditions, the initial melt should have a composition near the eutectic point, where the temperature is 1062 °C. If the frictional melting occurs under non-equilibrium conditions, the composition of the initial melt does not have to be the same as that at the eutectic point.

The chemical compositions of the matrix in the melt sample of albitite-quartzite are shown in Table 32 and plotted in the albite-silica binary equilibrium diagram in Fig. 62. Most of the matrix has a composition of the albite, although, the matrix has a composition of that near the eutectic point locally. A possible reason is that some small quartz fragments were measured together with the glass matrix, thus, the local matrix shows a chemical composition with a high $SiO_2$ content plotted in the area near the eutectic point in the phase equilibrium diagram.

The chemical compositions shown in Fig. 62 indicate the initial melt was mainly formed under non-equilibrium conditions. It is not surprising that as the melt was formed by frictional heating in only a few seconds, there was no enough time for a chemical reaction to reach an equilibrium state. There is no silica composition glass in the matrix. This indicates that the temperature did not reach the melting point of quartz during the frictional melting. It is estimated that the temperature was lower than the 1723°C of quartz and higher than the 1118°C of melting point of albite. The albite was preferentially melted by frictional heating in this experiment in the albite-silica (Ab-$SiO_2$) system.

***Anorthosite-anorthosite***

The anorthosite is mainly composed of 51.52 Wt.% $SiO_2$, 30.27 Wt.%% $Al_2O_3$, 14.35 Wt.% CaO and 3.12 Wt.% $Na_2O$, corresponding to 72 mole percent anorthite (An) and 28 mole percent albite (Ab). This is a almost pure albite-anorthosite (Ab-An) solid solution binary system.

The phase diagram for melting in Ab-An system (Fig, 63) can be used for determining the melting process and melt temperature in the anorthosite experiment. In this phase diagram, the upper curve is the liquidus curve, which connects the melting point of An at 1553°C to that of albite at 1118°C, and gives the composition of the liquid at any temperature. The lower curve is the solidus curve, likewise connecting the melting points, which gives the composition of the crystalline solution of plagioclase feldspar at any temperature.

The chemical compositions of the matrices are shown in Table 33 and plotted in the Ab-An phase diagram (Fig. 63). If the melt was formed under equilibrium conditions, the initial melt composition should have a composition at B ($An_{72}$) in the Ab-An phase diagram Fig. 63. But, it is clearly shown that all the chemical compositions of the matrices are concentrated near the chemical composition line of the host anorthosite. This indicates that the glass matrices were formed by the melting of the host anorthosite and underwent no chemical reaction during fractional melting. These results doubtlessly demonstrate that frictional melting in the albite-anorthosite (Ab-An) system was formed under non-equilibrium conditions. The minimum melting temperature was estimated to be about 1400°C from the An-An phase diagram (Fig. 63). The overshooting of temperature above the melting point and the temperature might have been higher than 1400°C during the frictional melting.

These experimental results clearly indicate that the frictional melting is not an equilibrium phenomenon, and this must be kept in mind when one estimates the physical conditions such as temperature reached during the formation of pseudotachylite in nature and in experiment. Estimates of temperatures obtained and pressure based on petrological data under equilibrum conditions thus are not precise.

## CHAPTER VIII. DISCUSSIONS

The origin of the fault-generated pseudotachylite will be discussed firstly in the light of the field and petrographic features of natural pseudotachylites. Then the pressure-temperature conditions of the Fuyun pseudotachylite formation will be estimated. Finally, the pseudotachylites-generating processes will be discussed based on the field, petrological and experimental results.

### *Origin of pseudotachylite*

The most important problem related to the origin of pseudotachylite is whether or not the matrix of this rock is melt formed by frictional heating on shear plane. Wenk & Weiss (1982) suggested two possiblilities: (1) the matrix of pseudotachylite consists mostly of glass by frictional fusion of rocks during seismic fault motion, although it might have been devitrified with time, (2) the matrix orinally consists of mostly ultrafine crush products due to severe shock deformation during rapid fault motion. They pointed out that there is insufficient evidence availabe to permit a clear choice between these alternatives.

The Fuyun pseudotachylite described herein is about the fifirst case in the world in which the melt origin of the matrix of pseudotachylite is clearly documented. Evidences for the melt origin include the presence of glass, even detectable with X-ray diffraction, and the formation of microlites of intermediate to high temperature exhibiting a great variety of crystal

forms, vesicles and amygdules, flow bandings and corroded or partly melted inclusions. The details are discussed below.

**Glass or glassy matrix**

Weiss & Wenk (1983) argued that the fine-grained component of the pseudotachylite would most probably be identified as glass by conventional methods of analysis such as optical microscope and X-ray diffraction. The X-ray powder diffraction patterns have been used to determine whether the isotropic or unisotropic fine grained matrix in pseudotachylites is glass or not (Willeme, 1938; Macaudiere et al., 1985; Toyoshima, 1990), but, no typical glass-diffraction pattern has been found in the fine-grained matrix so far, even when the size of the fine-grained matrix is submicron (Macaudiere et al., 1985).

We also undertook the X-ray diffraction analyses for the famous Outer Hebrides pseudotachylite described by Sibson (1975), Maddock (1983) and Macaudiere et al (1985) and the Musgrave pseudotachylite described by Shimamoyo & Nagahama (1991), but found only crystalline diffraction patterns and no glass-diffraction pattern, although the grain size of most of the fine grained matrix identified by TEM (Maddock, 1983) is as small as submicrons.

Generally, it is impossible to obtain the fine-grained matrix free from clasts, therefore it is also impossible to obtain a typical glass-diffraction pattern even if some glass remained in the pseudotachylite. In most cases, the pseudotachylite was crystallized during the pseudotachylite formation or devitrified after the pseudotachylite formation, therefore there is no

glassy material or only a little glass remaining which could not give a typical X-ray diffraction pattern of glass material.

The X-ray diffraction patterns of the Fuyun pseudotachylites clearly show glass or non-crystalline material diffraction patterns which are very similar to those of volcanic glass and artificially-generated glass fused from the granitic country rock. Of course, this glass X-ray diffraction pattern cannot completely deny the posibility that the matrix consists of mostly of ultrafine clasts (<submicrons). But, this possibility can be denied as following reasons.

(1) If the matrix was mostly composed of finely crushed clasts of the country rocks as pointed out by Wenk (1978), there would be the characteristic crystal peaks of micas and feldspars in the X-ray spectrum such as those occurring in the X-ray spectrum of the country rocks. But, excepting the quartz peaks, no other mineral crystal peaks can be clearly recognized in the glass type pseudotachylite. So, it is not possible that the matrix showing non-crystal diffraction pattern was the assemblage of the crushed clasts of the country rocks.

(2) The results of quantitative analysis show that the matrices in the Fuyun pseudotachylites have a gradation from almost complete crystalline to complete glass varying from a few Wt.% to 89 Wt.% of the veins. In the glass type pseudotachylite, there are only 11 percent crushed clasts which are larger than 2 microns in size, and about 90 percent matrix which shows a typical glass X-ray diffraction pattern. If the matrix is the assembage of ultrafine crushed clasts, about 90 percent clasts in the pseudotachylite must be smaller than submicron in size. Generally, the fine clasts are generated simutaneously with those coarse clasts (Shimamoto &

Nagahama, 1991). Thus, the matrix in the glass type pseudotachylite cannot be regarded as the assemblage of crushed ultrafine clasts.

(3) Furthermore, the flow structures, vesicles or amygdules and rounded fragments show a fore-melt state during the pseudotachylite formation and the characteristic of complete imperviousness to light under crossed nicol shows a glass state optically.

Therefore, the X-ray glass-diffraction patterns were formed by glass matrix rather than fine-grained crushed clasts in the Fuyun pseudotachylites. The presence of the glass pseudotachylite veins undoubtedly demonstrates that the Fuyun pseudotachylites were formed by frictional melting other than crushing of the host rocks.

**Microlites**

Acicular, dendritic and spherulitic microlites are ubiquitous existence in pseudotachylites. Waters and Campbell (1935) stated that microlites although common in volcanic glasses, also develop in cherts, other fine grained materials and metamorphic rocks. Masch et al (1985) found that the dendritic-spherulitic microlites present in the pseudotachylites of the Silvretla, Alps are pure albite and suggested that they are metamorphic minerals. They argued that the spherulitic structures are not uncommon in low grade metamorphic terrain and microlites may be actually porphyroclasts. In the Fuyun pseudotachylite, we can completely reject the possibility of metamorphism and porphyroclast for following reasons:

(1) The presence of high temperature minerals such as sanidine, anorthoclase, plagioclase ($An_{40-70}$), pyroxene, grossular which are never

present in the host rocks and cannot form during metamorphism or alteration.

(2) From the margin to the center of veins in the microcrystalline and the microlitic pseudotachylite veins, the size of microlites become progressive larger and the shape varies from simple shape such acicular to a complex dendritic-spherulitic morphology.

(3) In the glass matrix of type-IV veins, the microlites almost consist entirely of sanidine, anorthoclase and plagioclase (An>40), and the single crystal or crystal fiber is generally smaller than that developing in the crystalline matrix.

(4) The biotites and hornblendes with high Ti component intergrew and overgrew the plagioclase microlites (An>40-70) show complex dendritic and spherulitic textures.

(5) The spider-like microlites show clearly flow textures which are parallel and oblique or perpendicular to the flow streak-like flow structures in the pseudotachylite veins.

The presence of sanidine, plagioclase (An>40-70), anorthoclase, clinopyroxene, grossular and high Ti biotite and hornblende undoubtedly prove their high temperature origin. In metamorphic rocks, these high temperature minerals of sanidine, anorthoclase and pyroxene indicate the metamorphic conditions of granunite-eclogite facies (Miyashiro, 1965; 1973). The anorthite component in plagioclase generally increases with the temperature in metamorphic rocks (Sen, 1959) and in the experimental results of crystal growth (Lofgren, 1974). The An components are smaller than 30 percent in the plagioclase fragments came from the country rocks, but the microlites have a high An component varying from An30 to

An70. This indicates that the plagioclase microlites formed at much higher temperature than the plagioclases in the country rocks.

The analyses of microstructure of fault rocks and deformational history suggest that the granitic mylonites distributed in the Fuyun fault zone where the pseudotachylites were injected, mainly formed at the metamorphic conditions of sub-epidote-amphibole facies corresponding to a depth of about 10-15 km (Lin & fan, 1984). The later cataclastic zone has been formed in the mylonites along the fault zone where the carbonate veins, quartz veins and chlorite veins were injected. The Fuyun pseudotachylite veins have cut the quartz veins as stated above. This indicates that the depth of formation of the Fuyun pseudotachylite is never greater than 10 km. Assuming a continental geothermal gradient of 30 °C/km, the temperature of country rocks was under 300 °C before the formation of the Fuyun pseudotachylite. Therefore, it is impossible that the high temperature minerals such as sanidine, anorthoclase, high An plagioclase and pyroxene can be formed by metamorphism in those shallow depth conditions.

The crystal morphologies such as skeletal, dendritic and spherulitic shapes have been confirmed to be a function of the rate of cooling or the degree of supercooling of the liquid in which the crystal grew by direct experiment for the feldspars, pyroxene and olivine (Lofgren, 1980). Experimental results in the laboratory on crystal growth have shown that the morphology of crystals grown from an An-Ab-$H_2O$ system with the degree of undercooling (Lofgren,1974, 1980; Doherty, 1980). As the degree of undercooling increase, the single crystal fiber becomes finer and finer and the morphology changed from polyhedral through dendritic and finally to spherulites. This can explain the changes of

morphologies and size of microlites from margin to center of the vein and from glass matrix to crystalline the matrix in the Fuyun pseudotachylites. That the microlites developed in the glassy margin of the vein are small in size and simple in shape indicates they formed primarily by supercooling or quenching of a melt, and the complex dendritic and spherulitic textures are the final products under different stages of cooling the melt.

The overgrowth of biotite and hornblende on the plagioclase with have An content clearly indicates that it formed in two-step processes. The plagioclases with high An content formed in the first stage, and then the biotite and hornblendes overgrew the plagioclase. The textural variation between the outward edge and center in the same sheaf plagioclase microlites also indicates that it formed in different stages. These textures are common in glassy volcanic rocks (e.g. Lofgren, 1971) but rarely reported in the metamorphic rocks. Therefore, it is postulated that that these textures are the products formed in different stage during supercooling of the melt.

That the body bars of spider-like microlites found in the glass matrix are mostly arranged parallel to the flow structures in the pseudotachylite veins and that the trichites grown on the edge of body bars of spider-like microlites were bent, accompanied by the flow streak-like flow structures in the pseudotachylite veins shows clearly that these textures formed by flowing of a melt during the injecting of the pseudotachylite veins. That some trichites grown at the edge of body bars of spider-like microlites are oblique or perpendicular to the body bars and flow structures also indicates that they formed in a two step processes. In the first stage, the body bars formed and were arranged in the flow structures during

injecting of a melt. In the second stage, the body bars became new nuclei of crystal, and the trichites were formed on the side faces of the body bars after the flowing had stopped. The similar flow textures of microlites are also described for glassy volcanic rocks (Ross, 1962). It is not possible that thermal metamorphism could form these flow textures at the shallow depth at which the glass was preserved. Therefore, we assume that the flow textures of the spider-like microlites are the products of flowing of a injected melt during the pseudotachylite formation.

Although the devitrified experimental results have shown that the spherulitic textures can be formed by devitrification of the glasses of volcanic rocks (Lofgren, 19771a), this also can be rejected by the observation (1)-(5) stated above. The textures and the presence of the microlites of high temperature clearly indicate that they formed by quenching or supercooling of a melt.

**Vesicles and amygdules**

Vesicles generally form by the exsolution of gas from a melt. The presence of vesicles and amygdules occasionally found in pseudotachylite is one of the most convincing pieces of evidence clearly indicating a former melt state. Although Philpotts (1964) pointed out that the fluidized solid-gas systems proposed by Reynolds (1954) could explain the presence of some vesicles in pseudotachylite, this could not explain the textural variations found in the Fuyun pseudotachylites. That volume percents of vesicles and amygdules increase from the margin to the center of the vein as described by Philpotts (1964) and in this study, shows unequivocally that they formed at a different cooling rate of a melt. The elliptical

amygdules ranging parallel to the flow structures in their long axes show that they were formed from a melt by flowing during pseudotachylite vein formation. From the volume per cent of vesicles and amygdules, the estimate of formation depth of pseudotachylite can be made (Maddock et al., 1987). This will be discussed later.

**Flow structures**

A flow structure in a pseudotachylite vein showing a change in banded color, in composition similar to that occurring in extrusive rocks are frequently proposed to be formed by viscous flow in a molten state (Philpotts, 1964; Wallace, 1976; Toyoshima, 1990). Reynolds (1954) suggested that transportation of fine grained fragments in a gas-solid system could form such a turbulent flow structure. But, this gas-solid system can not explain the formation mechanism of the similar-fold flow structures in the pseudotachylites found in the Fuyun fault zone, the Alpine fault (Wallace, 1976) and the Hidaka metamorphic belt (Toyoshima, 1990). The pseudotachylites of crushing origin injected into fractures in the country rocks as single and complex veins, might be formed by a gas-solid system, but there are no clear flow structures such as flow streaks and similar folds.

We explain that the flow structures resembling the similar-fold described in this study were formed during the formation of pseudotachylites from a melt by the Bagnold effect, wall effect or Magnus effect (Komar, 1972; Barrier, 1976). For the Bagnold effect, the velocity in the longitudinal cross-section of a channel in a flowing newtonian fluid can be calculated from the equation:

$$U=U_{max}(2RY-Y^2)/R^2 \qquad \text{(Barrier, 1976)}$$

where U (cm) is the velocity of a Newtonian suspension in a lamellar flow at a Y distance from the margin; $U_{max}$ is the velocity of the center of channel, 2R is the width of channel (Fig. 64). The velocity of near center, $U_{max}$, is always larger than that far from the center and the difference of flow velocity between the margin and center forms the U shape flow banding. Together many of these flow bandings can form the flow bandings resembling similar folds observed in this study.

The flow structures of the spider-like microlites discussed above also show a flowing mechanism of the melt during pseudotachylite formation.

**Fragments**

The rounded fragments found in pseudotachylites generally have been attributed to three possible process (Sibson, 1975): (1) attrition caused by rotational grinding, (2) explosive decrepitation due to fluid expansion during rapid heating, and (3) thermal corrosion by the melt phase. The roundness of 80% of fragments are larger than 0.5. It has been shown above that the Fuyun pseudotachylites formed under brittle deformation conditions, therefore, there are no ductile deformation mechanism to round the porphyroclasts as occurred in the mylonites.

The grains of quartz in the fault gouges generally show conchoidal and cleavage fractures in shape (Kanaori et al., 1980). The observation of the quartz grains in experimental and natural gouges show that the large grains can be rounded slightly by abrasion during fault slip, but the small grains of submicrons to microns are relatively unaffected (Olgaard & Brace, 1983). Therefore, it is very difficult to form a great many rounded fragments of roundness >0.5 in the attrition caused by rotational gliding and abrasion in the fine quartz grains as small as submicrons to a few ten microns in size.

Kanaori et al (1980) described surface textures of quartz observed with SEM, from gouge zones of various ages. They classified four groups of textures according to degree of corrosion by groundwater. None of these textures were observed for the Fuyun pseudotachylites. It is unlikely, therefore, that the rounded grains were caused by groundwater corrosion after pseudotachylite formation.

In the light of the above arguments, the presence of glass pseudotachylite veins, high-temperature microlites showing quenching or supercooling textures, vesicles or amygdules, rounded fragments and flow structures undoubtedly demonstrates that the Fuyun pseudotachylites formed by frictional melting rather than crushing of the country rocks.

### *Depth of the pseudotachylite formation*

The presence of vesicles, amygdules and glass matrix implies a shallow depth of pseudotachylite formation. The solubility function of water related to pressure in the experiments of andesite melting has been used to estimate the depth of pseudotachylite formation (Toyoshima,

1990). The problem concerning the use of this method is how to determine the water content formed during the pseudotachylite formation. Although Toyoshima (1990) estimated the water content for the Hidaka pseudotachylites from the total amount of oxides in the bulk composition determined by the microprobe analysis, the heterogeneous fine matrix however makes it difficult to determine water content accurately by the microprobe analysis. Toyoshima (1990) also showed a variation from 86 Wt.% to 100 Wt.% of the total amount of oxides in pseudotachylites compositions.

The Fuyun pseudotachylites contain 2.3 wt.% to 2.65 wt.% water ($H_2O^+$) contents which are the initial water contents in the melt during the pseudotachylite formation. The largest water content of 2.65 wt.% is used to estimate a maximum depth of the pseudotachylite formation here. Although the matrices are heterogeneous in chemical compositions, most of the them have a composition similar to andesitic composition as shown in Tables 6,7. Using the graph of weight percent of water against pressure in andesitic glass (Hamilton et al., 1964), a maximum lithostatic pressure of about 400 bars is obtained corresponding to a depth of about 1.5 km.

Vesicles form by the exsolution of gas from a melt. The pressure under which the vesicles form can be estimated from the model (Macpherson, 1984) by measuring the total volume percent of the vesicles in the submarine pillow basalt. Maddock et al. (1987) used this model to estimate the depth of the Ikeraqu pseudotachylite formation by measuring the total volume percent of vesicles in the pseudotachylite. The matrices of the Fuyun pseudotachylites generally have a andesitic composition, so this model made from basalt melt can not directly used to estimate the depth. Herein, we modify the model of Macpherson (1984) by

using the relationship between the solubility of water and pressure in andesitic melt. For details of the calculation procedure and methods refer to Macpherson (1984).

$H_2O$ and $CO_2$ are supposed to be the major vapor components in the andesitic melt. The solubility function of water was obtained by taking an approximate lineation function from the graph determined by Hamilton et al. (1964). The relationships so obtained are

$$Wp(H_2O) = ( P + 360.12 ) / 310.95 \quad (P>260.8 \text{ bars}) \quad .....(1)$$

$$Wp(H_2O) = ( P + 5.663 ) / 133.27 \quad (P<260.8 \text{ bars}) \quad .....(2)$$

where the Wp ($H_2O$) is the weight percent of water that is soluble in a andesitic melt under a pressure (P). The model solubility function of $CO_2$ used here is the empirical relationship determined by Harris (1981):

$$Wp(CO_2) = 0.0005 + 0.059 \text{ P (kb)} \quad .....(3)$$

where the $Wp(CO_2)$ is the weight percent of $C0_2$ soluble in a andesitic melt.

The amount of a volatile component in the vapor W(V) is then given simply by

$$W(V) = W^*(H_2O) + W^*(CO_2) - [\, Wp(H_2O) + Wp(CO_2) \,] \quad ....(4)$$

where $W^*(H_2O)$ and $W^*(CO_2)$ is the weight percent of $H_2O$ and $CO_2$ initially in solution respectively.

The volumes ( V ) of $H_2O$ and $CO_2$ vapors per liter andesitic melt were calculated independently using the idea gas law as described in Macpherson (1984). Thus,

$$V\ (\text{vesicles}\ \%) = 100\ \frac{[\, V(CO_2) + V(H_2O)(\text{liters})]}{[\, V(CO_2) + V(H_2O)(1\ \text{liter})]}$$

The modified model curves for vesicles in the glassy andesitic pseudotachylites were obtained and are shown in Fig. 65, assuming initial dissolved $CO_2$ contents of 0.1 and 0.2 Wt.% respectively, and a range of initial $H_2O$ contents.

The volume of vesicles often varies from the margins to the center of the pseudotachylite veins (Philpotts, 1964) and also varies from injected veins to those remaining on the fault surfaces (this study). It is more convincing that the vesicle content of the pseudotachylite remaining on fault surfaces reflects the lithostatic pressure of vesiculation during the pseudotachylite formation. Here, the vesicle volumes were measured on

microphotographs directly on the samples obtained on the fault plane, and an average volume percent of 3.0% was obtained.

The Fuyun pseudotachylites contain 2.3 to 2.65 Wt.% water content($H_2O$). The initial water in the melt would be higher than or equal to 2.65 Wt.%. Using the maximum water content as an initial water content, a minimum pressure estimate of 350 bars (35 MPa) was obtained. Although the initial water content is not known clearly, it is assumed to be formed at a condition near that of solidification of the melt. When we used the 3.5 Wt. % line as an upper limit of initial water content, a 450 bars (45 MPa) maximum pressure estimate was obtained. The estimated pressure ranging from 350-450 (35-45 MPa) bars obtained from this model relating vesicle volume to pressure is consistent with that estimated by the relationship between the solubility of water in andesitic melt and pressure.

***Temperature***

The vesicles and amygdules in the matrix indicate the presence of an excess fluid phase. Using the experimental results in the system $SiO_2$ (Kennedy et al., 1962), an estimate of minimum temperature of 1450 °C was obtained for the melt generated by frictional heating during the pseudotachylite formation by the presence of pure $SiO_2$ composition glass at the depth of 1.5 km. The melt formed by frictional melting has a very transient existence, with cooling half-lives for injection veins of 1cm in width of the order of 40 s (Sibson, 1975), therefore, considerable overstepping of the temperature was necessary for melting the quartz grain in a melt. Thus, the estimated 1450 °C represents a minimum temperature estimate of the melt.

*Melting process*

As stated above, it is clear that the Fuyun pseudotachylites have been melted. It is necessary to determine how the melting took place during pseudotachylite formation.

The average chemical compositions of pseudotachylites are often similar to those of the rocks in which they occur, therefore it is often suggested that frictional fusion invokes total melting rather than selective melting of the country rocks (e.g. Philpotts, 1964; Ermanovics et al., 1972; Masch et al., 1985; Toyoshima, 1990). Because it is impossible to free the clasts from the pseudotachylites, the average composition of matrix and fragments, of course, has a similar composition with the country rock. The similarity of the chemical compositions between the melt material generated by the frictional melting experiment on amphiboles and the host rock was also found and suggested to be formed by total melting of the host rock (Spray, 1988).

However, it is often found that the chemical compositions of the matrix or pseudotachylites generally have a lower $SiO_2$ component than that of the country rock in which pseudotachylites occur (e.g. Shand, 1916; Sibson, 1975; Ermanovics et al., 1972; Toyoshima, 1990). The average chemical compositions of the Fuyun pseudotachylite are very similar to those of the granitic country rock, but the chemical compositions of matrices are 5-10 weight percent lower in $SiO_2$ component than those of the granitic country rocks. The X-ray data indicate that 11 weight percent quartz fragments were remaining and micas and feldspars completely disappeared in the glass pseudotachylite. This can explain why the matrices

have a lower $SiO_2$ component than that of the granitic country rock. It means that the lower melting point mineral, such as micas and feldspars, were completely melted and the high melting point quartz crystals remained as fragments during the pseudotachylite formation.

The chemical compositions of matrices in the experimentally- generated pseudotachylites by frictional melting on granite samples also show a characteristic of low $SiO_2$ component, which are 5-15 Wt.% lower than those of the host rocks of granites. The powder X-ray quantitative analysis results show that all micas, 17-44 Wt.% quartz and 65 Wt.% albite in the granite samples and all micas in the gabbro samples were melted in the artificially-generated pseudotachylites. This indicates that the micas and albite crystals were melted more easily than the quartz crystals, and the quartz still remained even when the micas and feldspars completely melted.

It is important to determine whether or not the frictional melting formed at chemical equilibrium for understanding the formation mechanism of the fault-generated pseudotachylites. If the melting formed at an equilibrium condition, the rocks could be melted at a relatively low temperature, such as an eutectic point. In this case, the rocks would be melted easily. For example, the granitic rocks which are mainly Qz-Or-Ab-$H_2O$ system can be melted at about 800 °C at 500 bars (50 MPa) under an equilibrium condition (Tuttle & Bowen, 1958). But, if it were not the case, the melting temperatures would be controlled by the melting points of the rock-forming mineral, and the rocks could be melted only at relatively higher temperatures, for example, between 1110°C-1700 °C, which are the melting temperature of plagioclases and quartz for granites.

Wallace (1976) has suggested that the hyalomylonites formed by frictional melting in the Himalaya Thrust Zone and the Alpine Fault Zone were neither generated by preferential melting of a low-melting point fraction nor by total melting, by plotting the chemical data in the phase diagram of Qz-Or-Ab system at 1 kb $P(H_2O)$. But, the pressures are unknown, this phase diagram can not be used directly to determine whether the melting process is in equilibrium or not. The results of frictional melting in albitite-quartz pair (Ab-Qz system) and anorthosite pair (Ab-An system) indicate that the frictional melting occurred non-equilibrium conditions. Although the eutectic point in Ab-Qz system is lower than the melting point of albite, most of the melt has an albite composition rather than a composition near the eutectic point, as shown in Fig. 62. This indicates clearly that the albite crystals have been preferentially melted under non-equilibrium conditions. Generally, the melting and cooling time during the pseudotachylite formation was so short that there was not enough time to allow chemical diffusion and to reach equilibrium.

The X-ray diffraction data and chemical compositions of natural and experimental pseudotachylites demonstrate that the fault-generated pseudotachylites formed mainly by selective melting rather than total melting or partial melting of the country rocks under non-equilibrium conditions.

*Role of water and rock types*

The role of water in the genesis of pseudotachylite in modifying frictional resistance during faulting has been discussed by a number of workers (Francis, 1972; Ermanovics et al., 1972; Sibson, 1973, 1975,

1980; Wallace, 1976; Allen,1979; Lachenbruch, 1980)). Sibson (1973, 1980) suggested that the general scarcity of pseudotachylite arises due to most seismic faulting taking place with water held roughly at constant volume around the fault plane. Frictional heating would tend to expand the pore fluid and cause a transient pressure increase, which could induce a sharp decrease in both the effective normal stress and dynamic friction on the fault surface (Sibson, 1980; Lachenbruch, 1980). The assumption of a pore fluid pressure was made based on the hypothesis that the water was held on the fault plane and did not migrated away quickly from the fault plane. By the observations during the frictional melting experiments in this study, melts formed by frictional melting on the sliding plane accompanying many small thermal cracks forming on both sides of sliding plane, and the melts were injected into the cracks. This implies that it is difficult to hold a large enough pore fluid pressure on the fault plane during seismic faulting at shallow depths. The frictional experimental results also show that the frictional melting can be generated under a low normal stresses as small as 10 bars (1 MPa), by rapid sliding. Thus, it is difficult for the pore fluid pressure to inhibits the generation of frictional melting on the fault plane during seismic faulting at shallow depths (<4-5 km) except when the pore fluid pressure is large enough to make the fault plane separate or lose contact completely. Melts formed by frictional fusion have a transient existence, with cooling half-lives for injection veins of 1 cm width of the order 40 s (Sibson, 1975). In the rapid frictional melting experiments, it has been shown that the melts were generated soon after sliding (2-5 s) in gabbro and granite samples. Under such condition, water will be critical to melting, not only because it reduces the temperature of fusion and lowers

the viscosity of the resultant melt, but also primarily because it acts as a catalyst during fusion (Allen, 1979).

The analysis of water contents also clearly indicates the presence of water during the Fuyun pseudotachylite formation in this study. The water contents of the pseudotachylites are about 2 wt.% larger than that of country rocks. On the other hand, the presence of vesicles and amygdules also indicates a water-saturated state in the melt during the pseudotachylite formation. It is impossible that the total water in the pseudotachylites came from the hydrous minerals of country rocks because of the lower water contents of country rocks. Thus, the Fuyun pseudotachylites were generated under water-saturated conditions in a fault zone rather than dry conditions. The dry condition is not a necessary condition for the formation of fault-generated pseudotachylite.

That the presence of hydrous minerals such as biotite is in favor of the pseudotachylite generation has been discussed ( Scott & Drever, 1953; Allen, 1979). It is postulated that the most suitable rock types for pseudotachylite generation will be quartz-rich rocks with a significant biotite content, the proportion of melts phase produced largely depending on the percentage of the biotite in the rock (Allen, 1979). The quartz-rich rocks are considered to be have high shear strength. The results of frictional melting experiments in this study show that biotite was preferentially melted during friction melting in granite and gabbros. Spray (1988) described that the hydrous minerals, such as amphibole, were the most susceptible to melting in his frictional melting experiment in gabbro sample. This experimental results demonstrates that the hydrous mineral-containing rocks are in favor of the pseudotachylite formation.

But, the experimental results in this study also show that the quartz-rich rocks hinder the generation of melting. The proportion of melts phase produced largely depends on the percentage of quartz in the rock in the same conditions. In the experiments on gabbro and anorthosite samples which rarely contain quartz, melting was generated in the first 2-3 s, and continued for 20-40 s to the end of the experiments. Amounts of melt were generated and the samples were not greatly broken. In the experiments on granites and albitite samples which contain a few ten percent quartz, for the first 5-6 s of sliding, amounts of small powder or fragments were formed; a little melts were generated after 5-8 s of sliding. The samples completely broke down after 9-15 s. In the experiments on quartzite and chert samples, the samples completely broke down in 10 s, and no melts could be obtained. The melting point of quartz is much higher than other mineral in granites. It is possible that when the temperature rose, many thermal cracks formed in the quartz crystals which made the samples break down before the temperature reached the melting point of quartz crystals. It is more like, therefore, that the quartz-poor rocks favor for the generation of pseudotachylite rather than the quartz-rich rocks at shallow depth.

## CHAPTER IX. CONCLUSIONS

In light of the above arguments, the following conclusions can be obtained.

(1) The Fuyun pseudotachylites formed by frictional melting rather than crushing of the granitic rocks.

(2) Powder X-ray studies demonstrate that the matrices in the Fuyun pseudotachylites have a gradation from complete glass vein to almost crystalline vein (several to 90 Wt.%).

(3) The microlites exhibiting quenching or supercooling textures, such as simple, skeletal, dendritic and complex spherulitic forms, are found in the Fuyun pseudotachylites and proved to be primary crystals formed from a melt during pseudotachylite formation.

(4) The presence of vesicles and amygdules and the high content of water indicates that the Fuyun pseudotachylite formed under water-saturated rather than dry conditions.

(5) Using the published data relating the solubility function of water against pressure, an estimate of 400 bars (40 MPa), corresponding to a depth of about 1.5 km, was obtained for the Fuyun pseudotachylites.

(6) Using the experimental results of the $SiO_2$ system, a minimum temperature of 1450 °C estimate was obtained by the presence of pure $SiO_2$ for the Fuyun pseudotachylites.

(7) Single vein and network pseudotachylite veins were successfully simulated by high-speed frictional experiments.

(8) The experiments show that the fault-generated pseudotachylite can be generated by frictional melting on the fault plane during seismic faulting even at depths as shallow as several ten of meters under earth's surface of deformation is concentrated at thin planar zones.

(9) The chemical compositions of glass and X-ray diffraction data of the natural and experimental pseudotachylites show that the frictional melting during pseudotachylite formation mainly formed by selective melting with a chemical non-equilibrium process rather than by total melting or partial melting.

(10) Quartz is the most resistant to melting, biotite the least resistant and feldspars intermediate in the frictional experiments on granite samples.

## REFERENCES


America Geological Institute (1980) Glossary of Geology. Edited by Bates,R.L. and Jackson,J.A., 751.

Allen,A.R. (1979) Mechanism of frictional fusion in fault zones. *J. Struct. Geol., 1*, 231-243.

Barrier,M. (1976) Flowage differentiation:Limitation of the "Bagnold effect" to the narrow intrusions. *Contrib. Minerl. Petrol., 55*, 39-145.

Beckholmen,M.(1982) Mylonites and pseudotachylites associated with thrusting of the Kolo Nappes, Tannforsfaltet, central Swedish Caledonides. *Geologiska, Foreningens i Stockholm Forhandlingar, 104*, 23-32.

Bei,M.X., Wu,T.W., Fan,F.T. and Luo,F.Z.(1985) Neotectonic active of Aertai Fault. The Fuyun Earthquake Fault Zone in Xinjiang, China. Edited by Ding, G., 142-162.*

Bowen,N.L.(1913) The melting phenomena of the plagioclase feldspars. *Am. J. Sci., 210*, 577-599.

Brandl,G. and Reimold,W.U (1990) The structural setting and deformation associated with pseudotachylite occurrences in the Palala shear belt and Sand River gneiss, northern Transvaal. *Tectonophysics, 171*, 201-220.

Bryan,W.B.(1972) Morphology of Quench crystals in submarine basalts. *J. Geophys. Res., vol.77, 29*, 5812-5819.

Cardwell,R.K., Chinn,D.S., Moorw,G.F. & Turcotte,D.L. (1978) Frictional heating on a fault zone with finite thickness. *Geophs. J. R. astr. Soc., 52*, 525-530.

Doherty,R.(1980) Dendritic growth. Phisical Magmatic Process. Edited by Hargraves R.B., 576-600.

Du,Y., Ma,S. and Ma,J.(1987) Keketuohai-Ertai shear zone and analysis of geneseismic tectonics. *Xinjiang Geology. 1*, 43- 54.*

Ermanovics,I.F., Helmstaedt,H. and Plant,A.G.(1972) An occurrence of Archean pseudotachylite from Southeastern Manitoba. *Canadian J. Earth Sci., 9*, 257-265.

Francies,P.W.(1972) The pseudotachylyte problem. *Comments Earth Sci., Geophys., 3*, 35-53.

Ge,S.M., Qian,R.H. and Gu,J.Z.(1985) Analysis on the stress of earthquake faults. The Fuyun Earthquake Fault Zone in Xingjiang, China. Edited by Ding, G., 82-87.*

Griggs,D.T.(1936) Deformation of rocks under high confining pressure. *J. Geol., 44*, 541-577.

Grocott,J.(1981) racture geometry of pseudotachylite generation zones: a study of shear fractures formed during seismic events. *J. Struct. Geol., 2*, 169-178.

Gupta,L.N. (1967) pseudotachtlites from central gneisses, Dharmsala. *The Indian mineralogist, 8, Nos.1-2*, 75-77.

Hamilton,D.L., Wayne Burnhm,C. and Osborn,E.F.(1964) The solubility of water and effects of oxygen fugacity and water content on crystallization in mafic magmas. *J. Petrol., 5*, 21-39.

Hobbs,E.B., Ord,A. and Teyssier,C. (1986) Earthquakes in ductile regime? In: Internal Structure of Fault Zones (edited by Chi-yuen Wang), 124, Nos1/2, 309-336.

Kennedy,G.C., Wasserburg,G.J., Heard,H.C. and Newton,R.C.(1962) The upper three-phase region in the system $SiO_2$-$H_2O$. *Am. J. Sci., 260*, 501-521.

Killick,A.M.(1990) Pseudotachylite generated as a result of a a drilling "Burn-in". *Tectonophysics, 171*, 221-227.

Klug H.P. and Alexander L.E. (1954) X-ray diffraction procedures. London. Chapman and Hall, Limited. 716.

Komar,P.D.(1972) Flow differentiation in igneous dikes and sills:profiles of velocity and phenocryst concentration. *Geol. Soc. Am. Bull., 83*, 3443-3448.

Karaori,Y., Miyakoshi, K. and Kakuta, K. and Satake, Y.(1980) Dating fault activity by surface textures of quartz grains from fault gouges. *Eng. Geol., 16*, 243-262.

Lachenbruch,A.H.(1980) Feictional heating, fluid pressure, and the resistance to fault motion. *J. Geophys. Res., 85*,6097-6112.

Lin,A.(1990) ESR and TL datings of active faults in the Iida area of the southern Ina valley. *Active Fault Research, 7*, 49- 62.**

Lin,C.Y. and Fan,F.T. (1984) Microstructural analysis of Fuyun Fault Zone, Xingjiang, China. *J. Seis.,.2*, 1-8.**

Lofgren,G.(1971a) Spherulitic textures in glassy and crystalline rocks. *J. Geophys. Res., vol.76, 23*, 5635-5648.

Lofgren,G. (1971b) Experimentally produced devitrification textures in natural rhyolitic glass. *Geol. Soc. Am. Bull., 82*, 116-124.

Lofgren.G.(1974) An experimental study of plagioclase crystal morphology: isothermal crystallization. *Am. J. Sci., 274*, 243-273.

Lofgren,G.(1980) Experical studies on the dynamic crystallization of silica melts. Physical Magmatic Process. Edited by Hargraves, R. B., 487-551.

Macaudiere,J. & Brown,W.L.(1982) Transcrystalline shear fracturing and pseudotachylite generation in a meta-anorthosite (Harris, Scotland). *J. Struct. Geol., 4*, 395-406.

Macaudiere,J., Brown,W.L. and Ohnenstetter,D.(1985) Microcrystal-crystalline textures resulting from rapid crystallization in a pseudotachylite melt in a meta-anorthosite. *Contrib. Miner. Petro., 89*, 39-51.

Mackenzie,D. & Brune,J.N.(1972) Melting on fault plane during large earthquakes. *Geophys. J. R. astr.Soc., 29*, 65-78.

MacKenzie,M.S., Donaldson,C.H. and Guilford,C. (1987) Atlas of igneous rocks and textures. Longman Scientic and Technical, 170.

Macpherson,G.J.(1984) A model for predicting the volume of vesicles in submarine basalts. *J.Geol.,92*,73-82.

Maddock,R.H.(1983) Melt origin of fault-generated pseudotachylites demonstrated by textures. *Geology, 11*, 105-108.

Maddock,R.H., Grocott,J. and Van Nes,M.(1987) Vescles, amygdulesand similar structures in fault-generated pseudotachylites. *Lithos, 20*, 419-432.

Magloughlin, J. F. (1989) The nature and significance of pseudotachylite from the Nason terrane, North Cascade Mountains, Washington. *J. Struct. Geol., 11*, 907-917.

Masch,L. (1977) Deformation and fusion of two fault rocks in relation to their depth of formation: the Hyalomylonite of Langtang (Himalaya) and the pseudotachylites of the Silvretta nappe (Eastern Alps). *U. S. Geol. Surv. Open-File Rep., 79-1239*, 528-533.

Masch,L., Wenk,H.R. and Preuss,E. (1985) Electron microscopy study of hyalomylonites-evidence for frictional melting in landslides. *Tectonophysics, 115*, 131-160.

Miyashiro,A. (1965) Metamorphic rocks and metamorphic zone. Iwanami shoden. 458.#

Miyashiro,A. (1973) Metamorphism and Metamorphic Belts. London, George Allen & Unwin. P492.

Olgaard,D.L. & Brace,W.F.(1983) The microstructure of gouge from a mining-induced seismic shear zone. *Int. J. Rock Mech. Min. Sci. Geomech. Abstr., 20*, 11-19.

Park,R.G. (1961) The pseudotachylite of the Gairloch district, Ross-shire, Scotland. *Am. J. Sci., 259*, 542-550.

Passchier,C.W.(1982) Pseudotachylite and the development of ultramylonite Massif, French Pyrenees. *J. Struct. Geol., 4*, 69-79.

Passchier,C.W.(1984) The generation of ductile and brittle shearbands in a low-angle mylonite zone. *J. Struct. Geol., 6*, 273-281.

Peterman,Z.E. & Warren,D.(1989) Earty Proterozoic activity on Archean faults in the western Superior province-evidence from pseudotachylite. *Geology, 17*, 1089-1092.

Philpotts,A.R and Miller,J.A.(1963) A pre-Cambrian glass from St. Alexis-des-monts., Quebec. *Geo. Mag., 4*, 337-345.

Philpotts,A.R.(1964) Origin of pseudotachylites. *Am. J. Sci., 262*, 1008-1035.

Piper,J.D.A. & Poppleton,T.J.(1988) Paleomagnetic dating of pseudotachylyte formation in the Lewisian Complex. Scott.. *J. Geol., 24*, 267-272.

Rechards,P.G.(1976) Dynamic motions near an earthquake fault: a three-dimensional solution. *Bull. Seis. Soc. Am., 66*,1-32.

Reimold,W.U., Grieve,R.A.F. and Palme.H.(1981) Rb-Sr dating of the impact melt from east Clearwater, Quebec. *Contrib. Mineral. Petrol., 76*, 73-76.

Reimold,W,U., Oskierski,W. and Huth,J.(1987) The pseudotachylite from Champagnac in the Rochechouart meteorite crater, France. *J. Geophys. Res., 92*, 737-748.

Reimold,M.U., Jessberger,E.K. and Stephan,T.(1990) Ar- Ar dating of pseudotachylite from the Verdefort dome, South Africa: a progress report. *Tectonophysics, 171*, 139-152.

Reynolds,D.L.(1954) Fluidization as a geologicalprocess, and its bearing on the problem of intrusive granites. *Am. J. Sci., 252*, 577-614.

Ross,C.S. (1962) Microlites in glassy volcanic rocks. *Am. Miner., 47*, 723-740.

Sato,H.(1975) Diffusion cornoas around quartz xenocrysts in andesite and basalt from Tertiary volcanic region in northestern Shikoku, Japan. *Contrib. Miner. Peter.,50*,49-64.

Schwarman,E.C., Meyer, C.E. and Wilshire, H.G.(1983) Pseudotachylite from the Verdefort Ring, South Africa, and the origins of some luner breccias. *Geol. Soc. Am. Bull., 94*, 926-935.

Seward,D. and Sibson,R.H.(1985) Fission-track age for a pseudotachylite from the Alpine Fault Zone, New Zealand. *J. Geol. Geophys., 28*, 553-557.

Scott,J.S. and Drever,H.I. (1953) Frictional fusion along a Himalaya thrust. Proc. Royal Soc., Edinburgh (part2), 121- 142.

Sen,S.K.(1959) Potassium content of natural plagioclases and origin of antiperthites. *J. Geol., 67*, p, 495.

Shand,S.J. (1916) The pseudotachylite of Parijs (Orange Free State), and its relation to 'trap-shotten gneiss' and 'flinty crush-rock'. *Quart. J. Geol. Soc. London,72*, 198- 221.

Shimamoto, T. and Nagahama, Y. (1991) The origin of pseudotachylites and the state-of-stress. *Earth Monthly (Chikyu), 13*, 416-427.

Shiraki,K. and Kuroda, N. (1977) The boninite revisted. *J. Geograpy., 96*, 34-50.##

Sibson,R.H.(1973) Interactions between temperature and pore-fluid pressure during earthquake faulting and a mechanism for partial or total stress relife. *Nature Phys. Sci., 243*, 66- 68.

Sibson,R.H. (1975) Generation of pseudotachylite by ancient seismic faulting. Geophys. *J. Royal Astro. Soc., 43*, 775-794.

Sibson,R.H.(1977) Fault rocks and fault mechanisms. *J. Geol. Soc. London, 133*, 191-213.

Sibson,R.H.(1980) Power dissipation and stress levels on faults in the upper crust. *J. Geophys. Res., 85*, 6239-6247.

Sibson,R.H., White,S.H. and Atkinson,B.K. (1981) Structure and distribution of fault rocks in the Alpine Fault Zone. New Zealand. In: Thrust and Nappe Tectonics (edited by McClay,K.R and Price, N.J.), *Sped. Publs geol. Lond., 9*, 197-210.

Sinha-Roy,S. and Ravinra Kumar,G.R. (1985) Pseudotachylites of the Bavali fault zone, Cannanore District, north Kerala. *J. Geol. Soc. Indian, 26*, 182-190.

Spray,J.G.(1987) Artificial generation ofpseudotachylyte using friction welding apparatus:simulation of melting on a fault plane. *J. Struct. Geol., 9*, 49-60.

Spray,J.G.(1988) Generation and crystallization of an amphibolite shear melt: an investigation using radial friction melting apparatus. *Contrib. Miner. Petro., 99*, 464-475.

Stel,H. (1981) Crystal growth in cataclasites: diagnostic microstructures and implications. *Tectonophysics, 78* 585- 600.

Swanson,M.T.(1988) Pseudotachylite-bearing strike-slip duplex structures in the Fort Foster Brittle Zone, S.Maine. *J. Struct. Geol., 8*,813-828.

Takagi,H.(1990) Earthquake fossile-pseudotachylite. *Chishitsu News, 437*, 15-25.

Toyoshima,T.(1991) Pseudotachylite from the Main Zone of the Hidaka metamorphic belt, Hokkaido, nerthern Japan. *J. Meta. Geol.,8*, 507-523.

Tuttle,O.F. & Bowen,N.L.(1958) Origin of granite in the light of experimental studies in the system $NaAlSi_3O_8$-$KAlSi_3O_8$-$SiO_2$-$H_2O$. *Geol. Soc. Am. Memoir., 74*, 145.

Voight,B. & Faust,C.(1982) Frictional heat and strengh loss in some rapid lanslides. *Geotechnique, 1*, 43-54.

Wadell,H.(1932) Velume, shape, and roundness of rock. *J. Geol., 40*, 443-451.

Wallace,R.C. (1976) Partial fusion along the Alpine Fault Zone, New Zealand. *Geol. Soc. Am. Bull.,87*, 1225-1228.

Waters,A.C.and Campbell,C.D.(1935) Mylonites from the San Anderess Fault Zone. *Am. J. Sci.,29*, 473-503.

Watts,M.T. and Williams,G.D.(1979) Comments on 'Are pseudotachylites products of fracture or fusion?'. *Geology, 7* , 162.

Wells,P.R.A. (1977) Pyroxene thermometry in simple and complex systems. *Contrb. Miner. Petro.,62,* 129-139.

Weiss,L.E. and Wenk,H.R. (1983) Experimentally produced pseudotachylite-like veins in gabbro. *Tectonophysics, 96*, 299-310.

Wenk,R.H. (1978) Are pseudotachylites products of fracture or fusion. *Geology 6*, 507-511.

Wenk,R.H. & Weiss,L.E.(1982) Al-rich calcic pyroxene in pseudotachylite: an indicator of high pressure and high temperature?. *Tectonophysics, 84*, 329-341.

Willemse,J. (1938) On the old granite of the Vredefort region and some of its associated rocks. *Geo. Soc. South Africa. Trans., 40*, 43-119.

Wilshire,H.G.(1971) Pseudotachylite from the Verdefort ring, South Africa. *J. Geol., 79*, 195-206.

Wood,B.J. and Banno,S.(1973) Garnet-orthopyroxene and orthopyro- xene-clinopyroxene relationships in simple and complex systems. *Contrub. Minera. Petrol., 42*, 109-142.

Yang,Z.,Ying,S., and Yu,L.(1981) Characteristics of fault rocks and their potential evidences seismic events. *Seis. Geol., 3*, 1-18. **

Yund,R.A., Blanpied,M.L., Tullis,T.E. and Weeks,J.D. (1990) Amorphous material in high strain experimental fault gouges. *J. Geoph. Res.,95, No.B10*, 15, 589-15, 602.

* In Chinese.

** In Chinese with English abstract.

# In Japanese.

##In Japanese with English abstract.

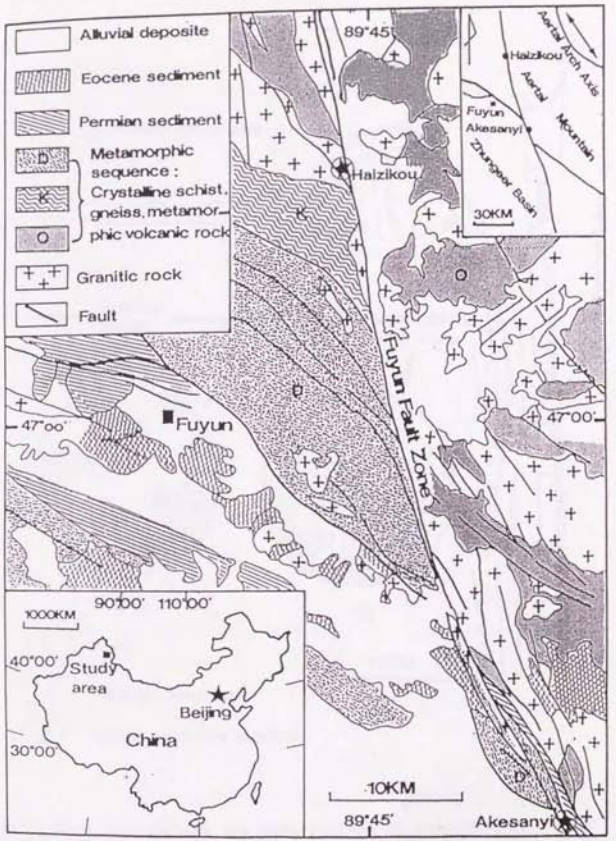


Fig. 1. Simplified geological map in the Fuyun region, northwest China. Star shows the location of pseudotachylite from the Regional Surving Team of Xingjiang Geological Bureau (1978).

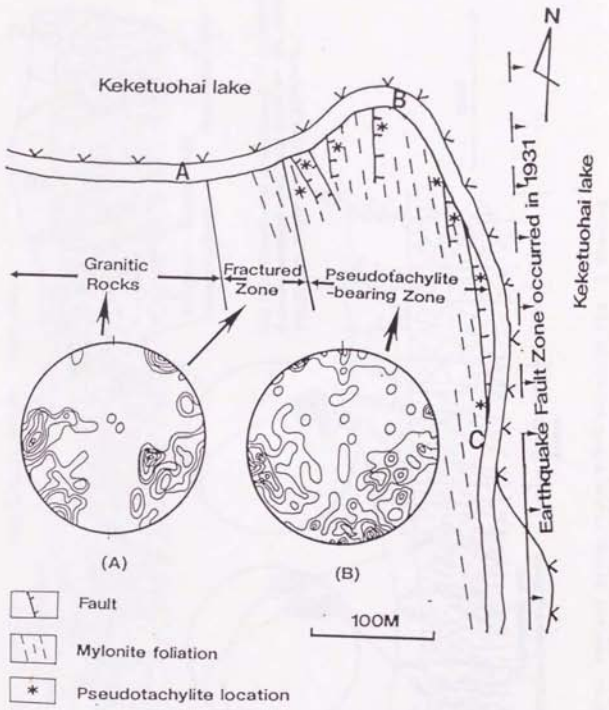


Fig. 2. Route map showing the distribution of pseudotachylites on the outcrop of the Haizikou location. (A),(B): Equal area projections of fractures (lower hemisphere). Counters (per 1% area) 1, 3, 5, 7, 9, 11.

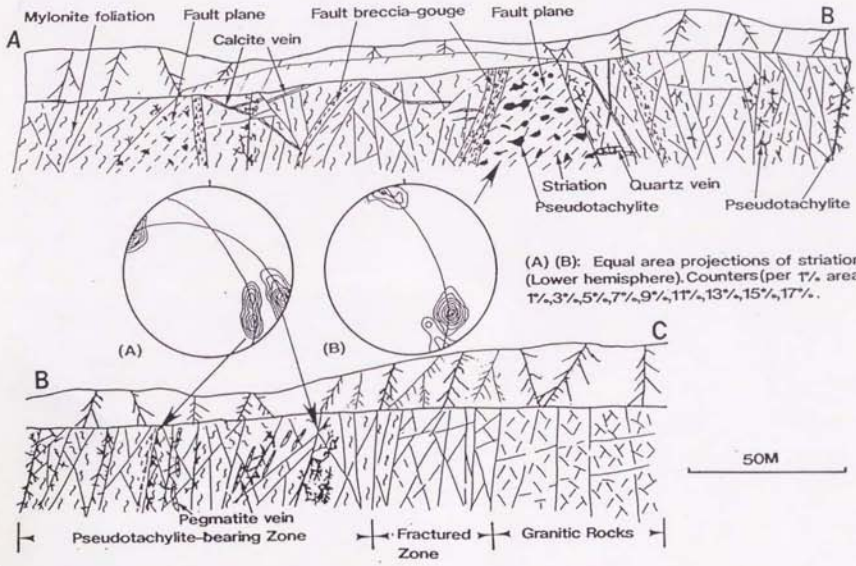


Fig. 3. Outcrop section along route A-B-C shown in Fig. 2 showing the distribution of pseudotachylites.

Fig. 4. Photomicrographs showing microstructures in the granitic mylonites where the pseudotachylites injected in. (A) Cataclasitic textures. (B), (C) Kink bands in biotite and microcline. (D) Quartz deformation lamella. (A),(B), (C):PPL (plane polarized light ), (D): CPL (crossed polarized light).

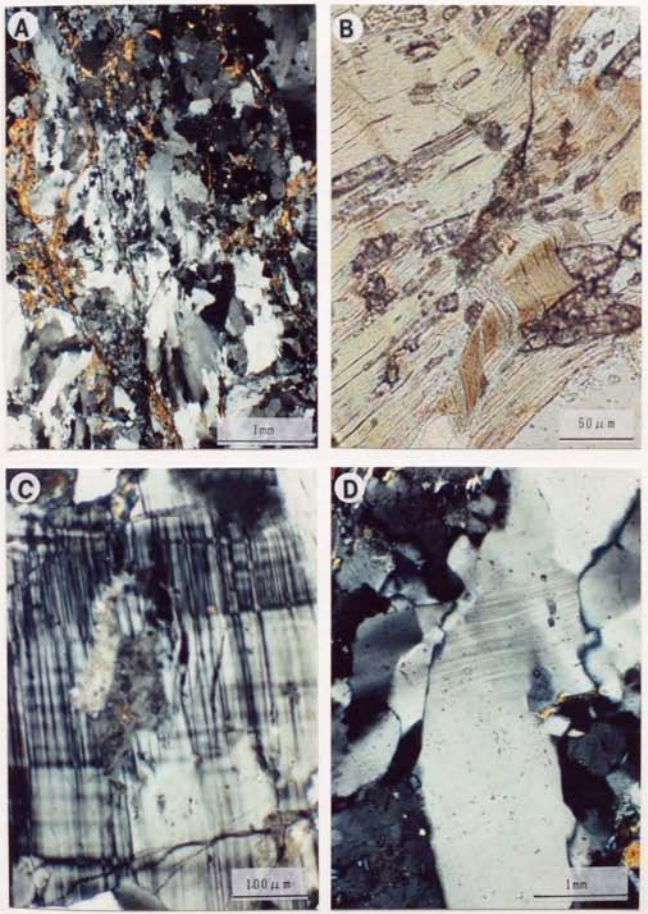

Fig. 5. Photographs of outcrop showing the occurrences of pseudotachylites remaining on the fault plane. (A) Outcrop of the fault plane where pseudotachylites remaining on. (B), (C) and (D) Pseudotachylites remaining on the fault plane.

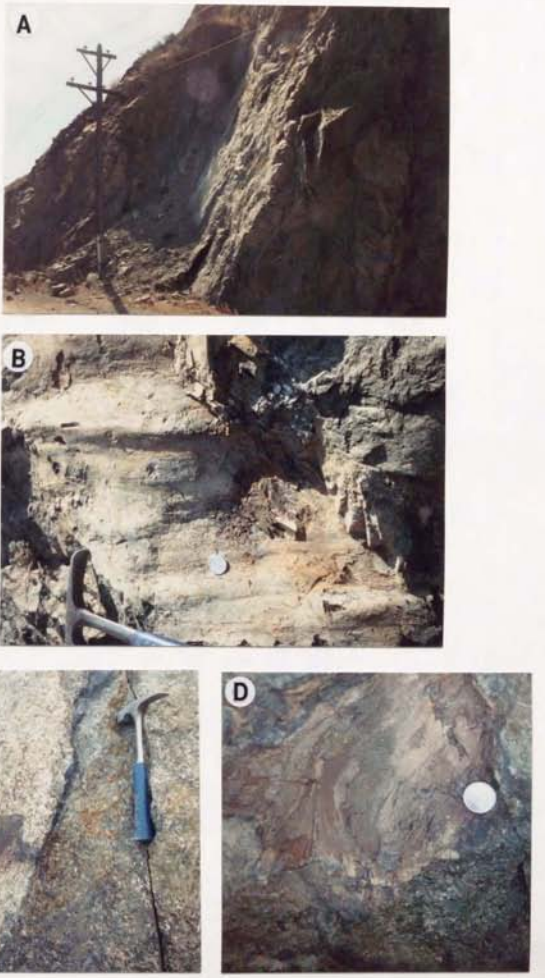


Fig. 6. Drawing of outcrop section from field showing the occurrence of irregular network pseudotachylite veins injected in granitic mylonite.

Fig. 7. Photographs showing the occurrence of single veins and network pseudotachylite veins injected in country rocks. (A), (B) and (D) Pseudotachylite veins injected in the mylonites. (C) Pseudotachylite veins cut and injected in the quartz vein.

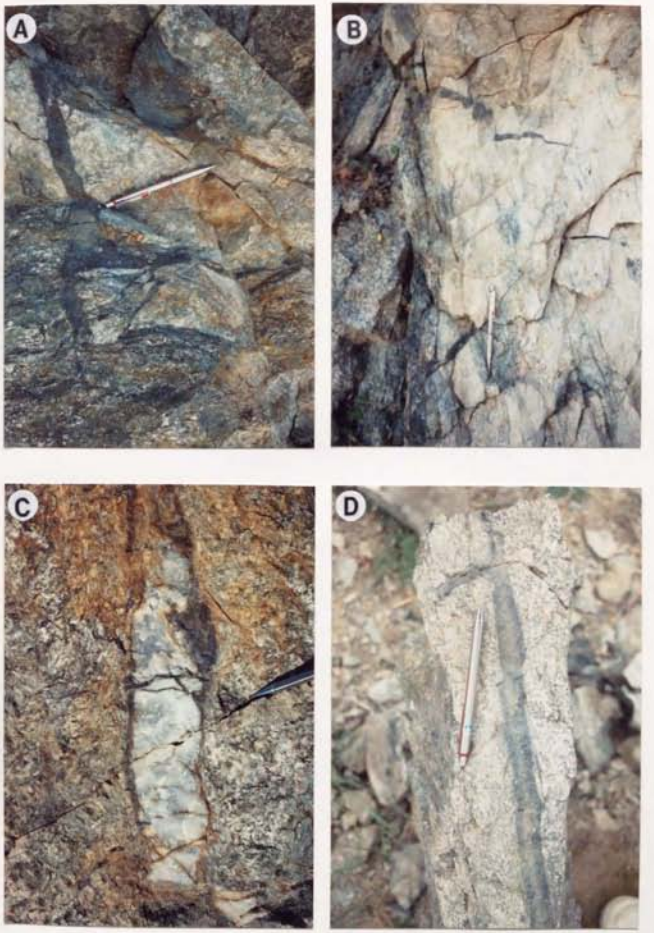

Fig. 8. Photomicrographs showing textures of pseudotachylites. (A) Network pseudotachylite veins (CPL). (B) New pseudotachylite vein injected into old pseudotachylite (PPL).

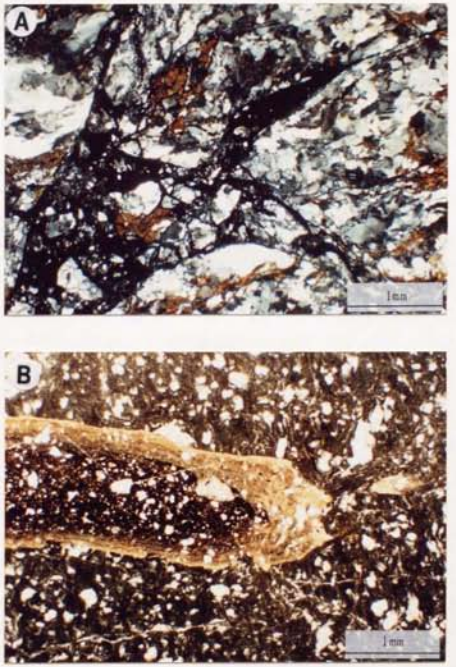

Fig. 9. Photomicrographs showing the general characters of matrices in pseudotachylites (PPL). (A) Glass matrix (Type-I). (B) Cryptocrystalline matrix (Type-II). (C) Microcrystalline matrix (Type-III). (D) Microlitic matrix (Type-IV).

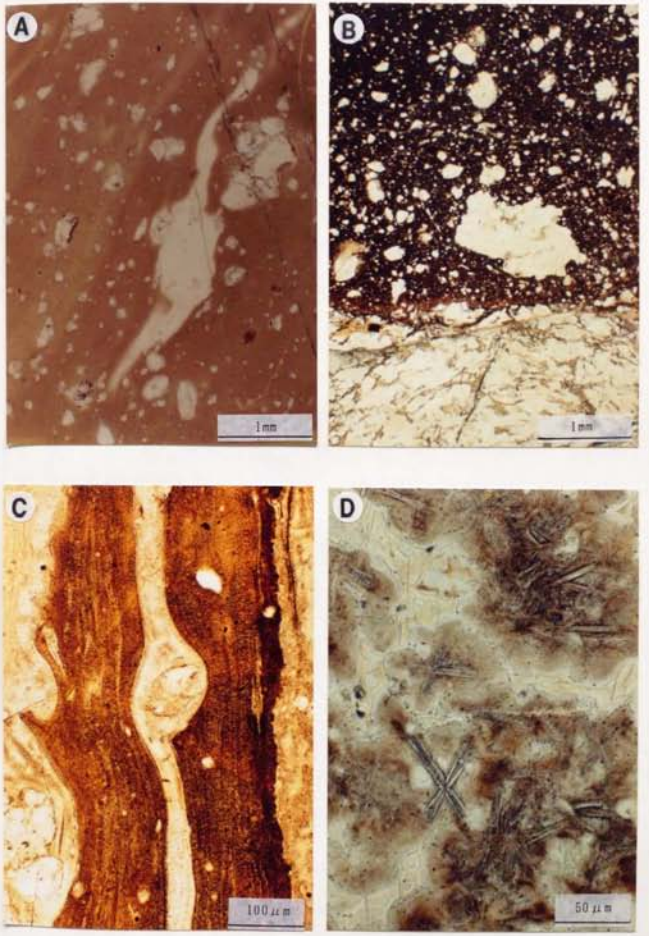

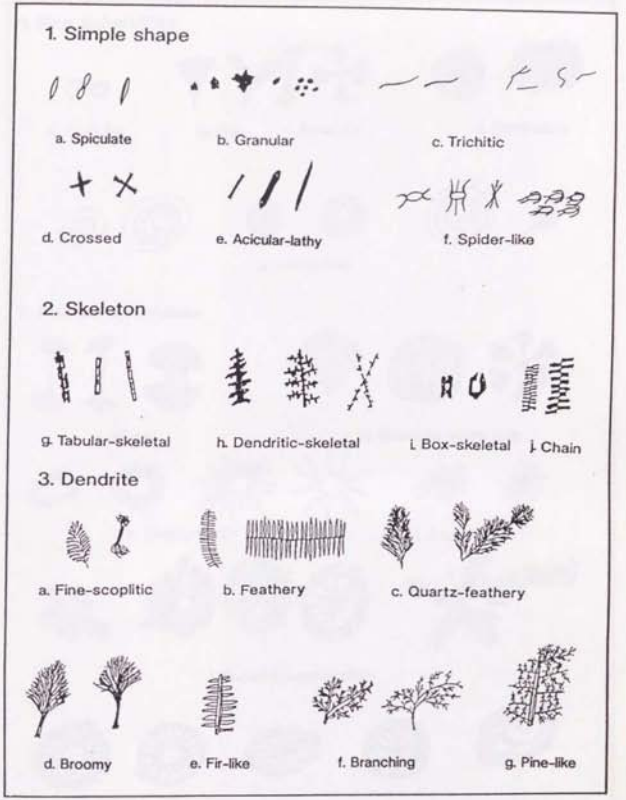


Fig. 10. Sketches of microlite shapes from photomicrographs showing simple shape, skeleton and dendrite forms.

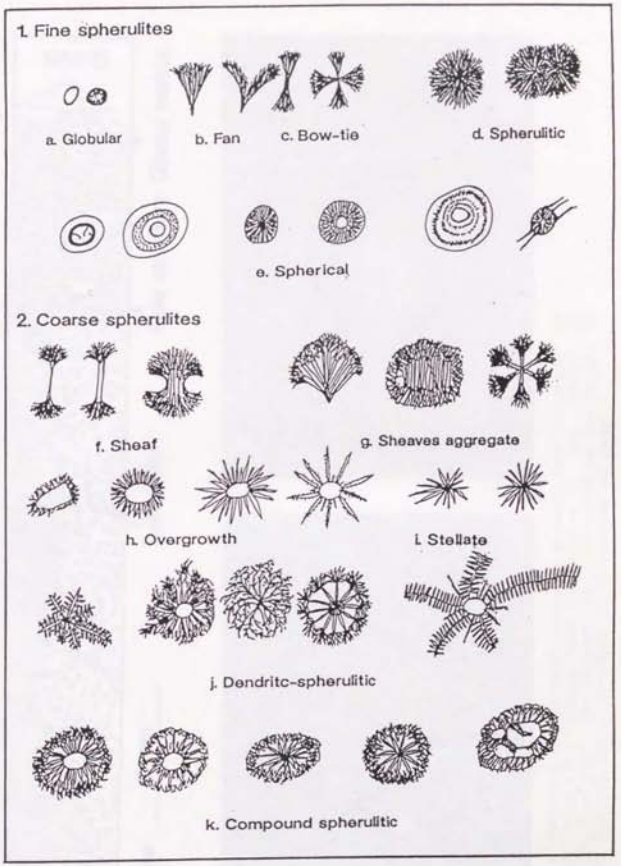


Fig. 11 Sketches of microlite shapes from photomicrographs showing the spherulite forms.

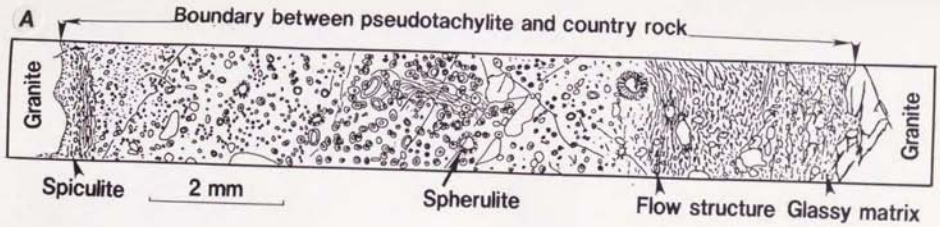


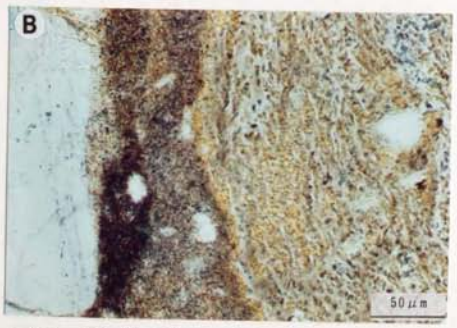


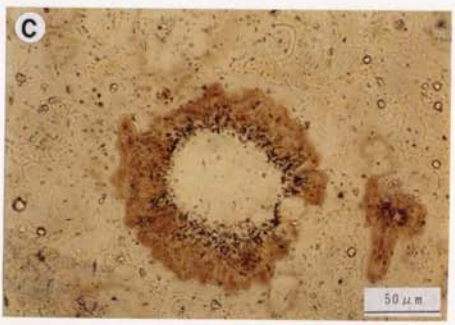


Fig. 12. Sketches and photomicrographs showing the variation of microlite size and shapes from the margins to the center of pseudotachylite vein. (A) Sketch. (B) microlites in the margin of vein. (C) Spherulitic microlites in the center of vein.

Fig. 13. Photomicrographs showing the textures of simple shape microlites (PPL). (A) Spiculate microlites aligning parallel to the flow lamellaes in glass matrix. (B) Spider-like microlites in the glass matrix. Note that the trichites (claws parts of spider-like microlites) are oblique or perpendicular to the flow lamellaes in glass matrix. (C) Trichitic and spider-like microlites aligning parallel to the flow lamellaes in the glass matrix. (D) Acicular-lathy microlites clusters.

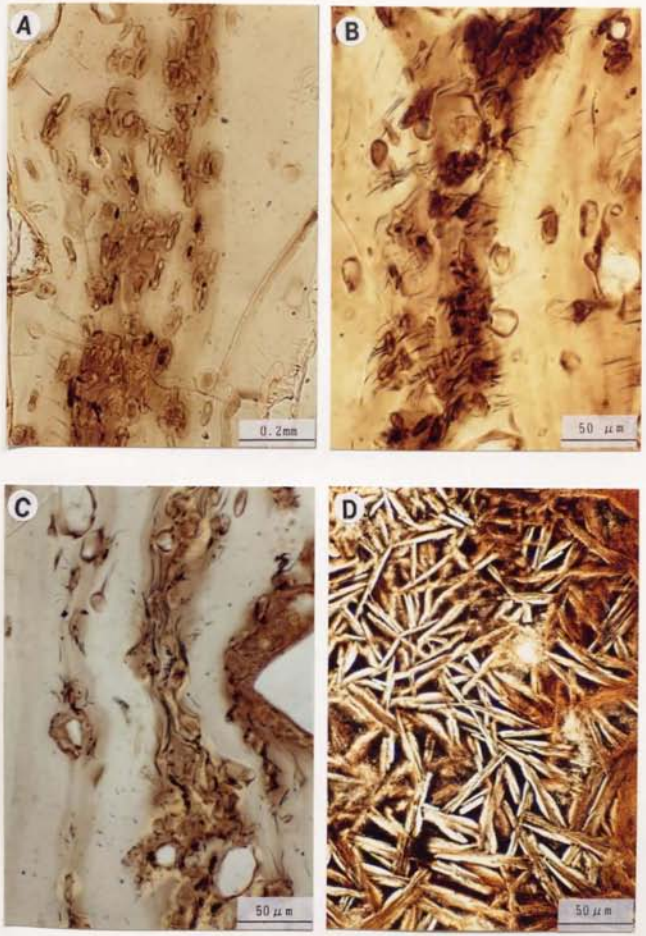

Fig. 14. Photomicrographs showing the skeletal textures. (A) Tabular-skeletal textures of hornblendes (BSE:back-scattered SEM image). (B),(C) Dendritic-skeletal (PPL). (D) Chain textures of hornblendes (BSE).

Fig. 15. Photomicrographs showing dendritic textures. (A) Quartz feathery microlites overgrown on quartz fragment(CPL: crossed polarized light). (B) Feathery (PPL). (C) Broomy (PPL).

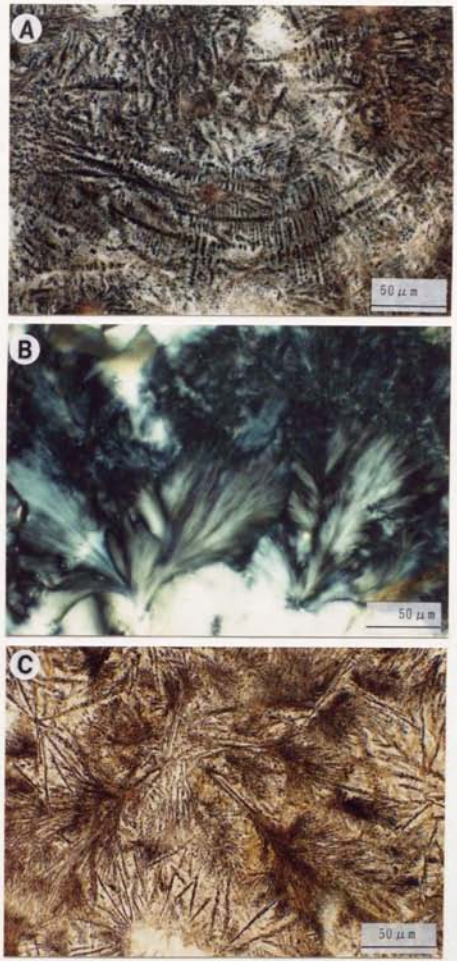

Fig. 16. Photomicrographs showing dendritic textures (PPL). (A) Fir-like. (B) Feathery. (C) Pine-like. (D) Branching.

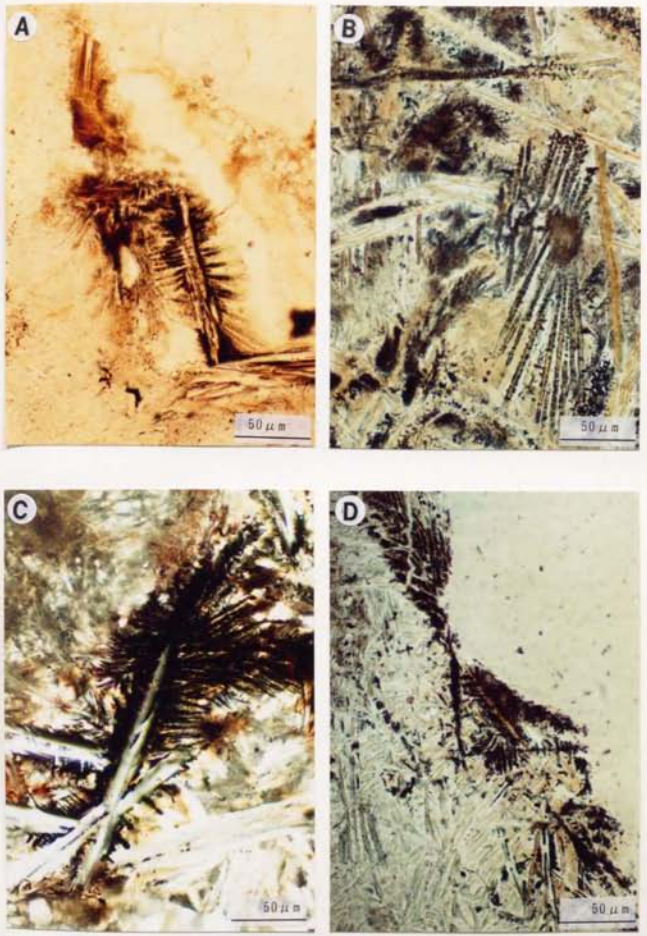

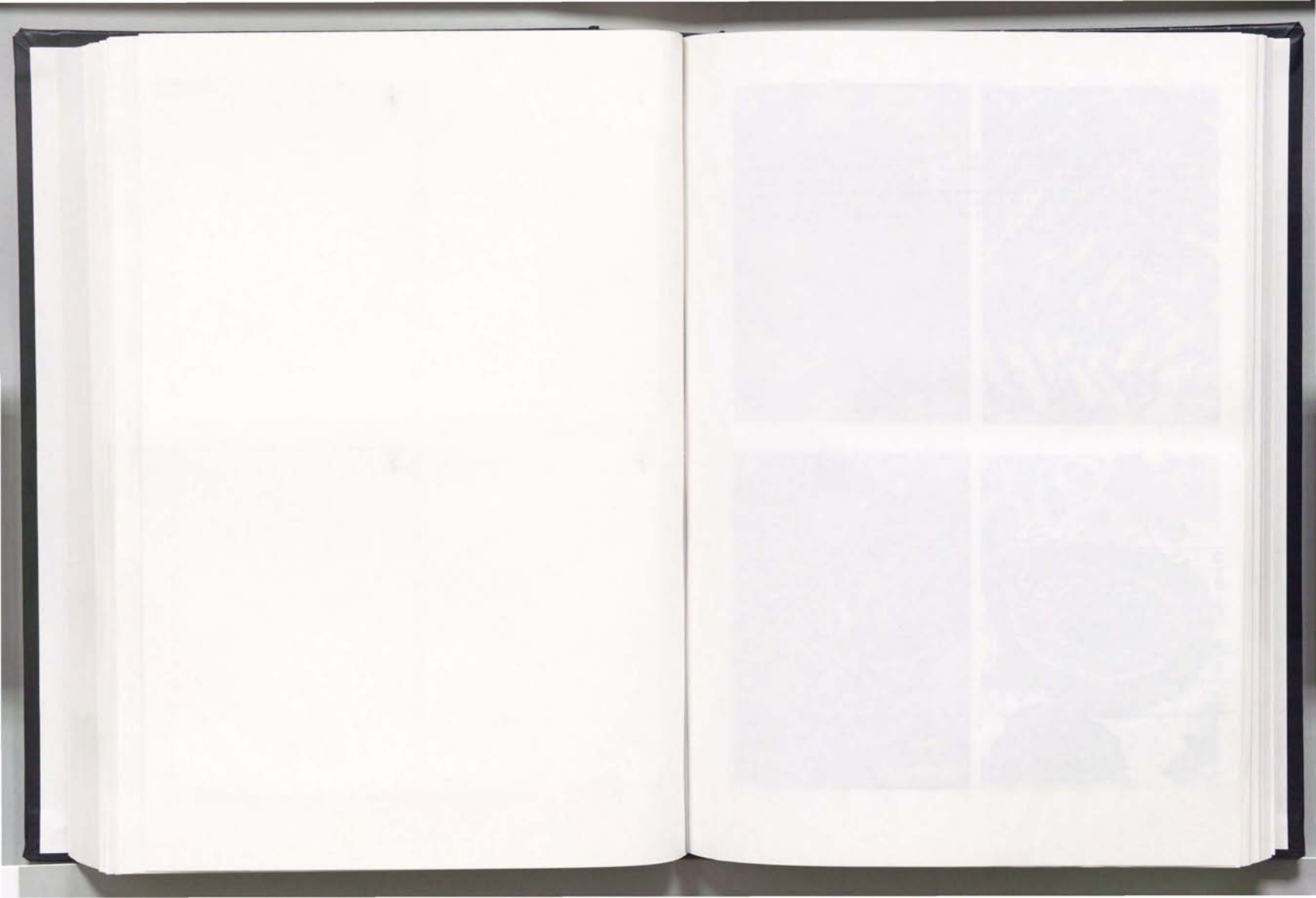

Fig. 17. Photomicrographs showing fine spherulitic textures. (A) spherulitic textures of anorthoclase (PPL). (B) Fan and bow-tie textures of anorthoclases (CPL). (C) Spherical textures (PPL). (D) Spherical textures showing zoning structure around the quartz fragment (BSE). Zones A and C have a chemical composition similar to albite. Zone B has a chemical composition similar to biotite.

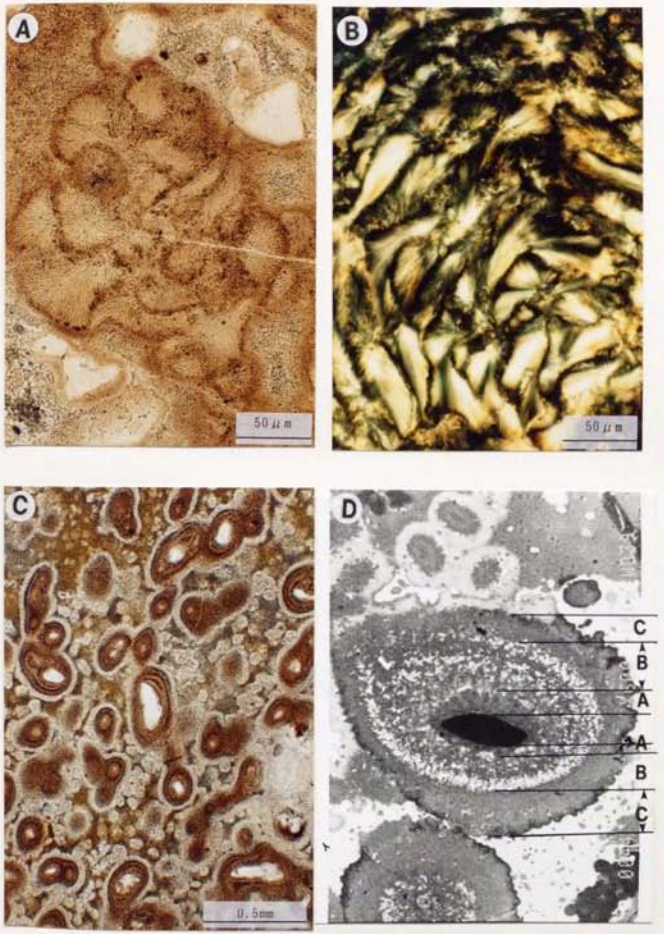

Fig. 18. Photomicrographs of coarse spherulitic textures in feldspars microlites (PPL). (A) Sheaf texture. (B),(C),(D) Sheaves aggregate textures.

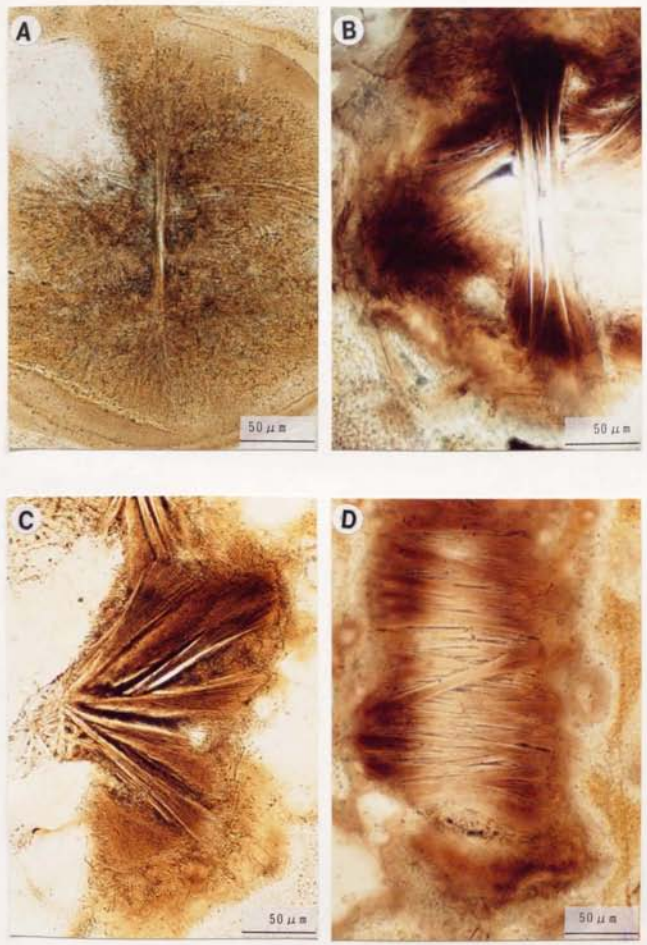

Fig. 19. Photomicrographs showing coarse spherulitic textures. (A),(B),(C) Overgrowth textures. (A),(B):(PPL). (C):(CPL) (D) Dendritic-spherulitic textures (PPL).

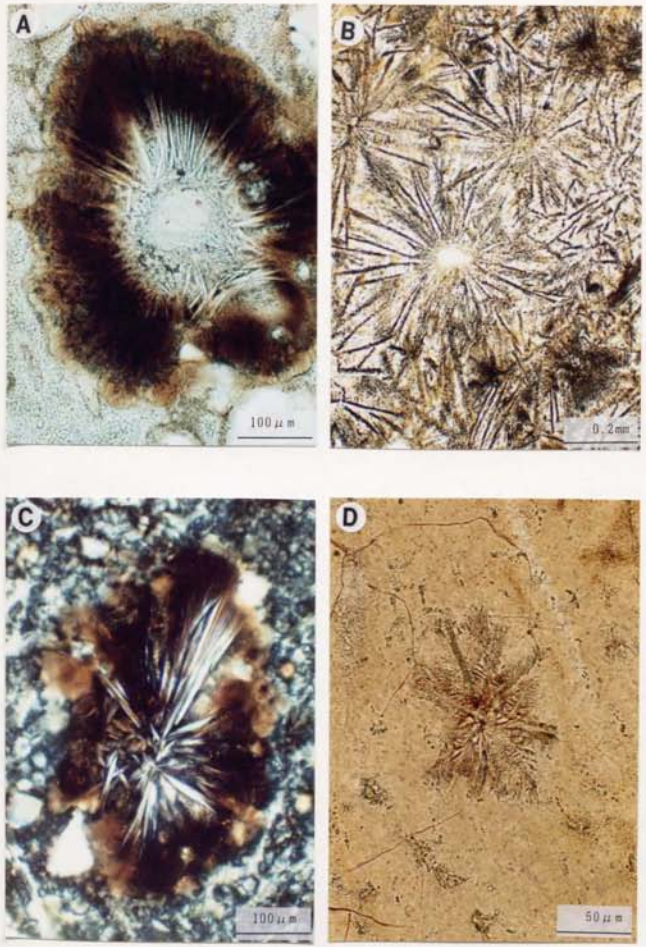

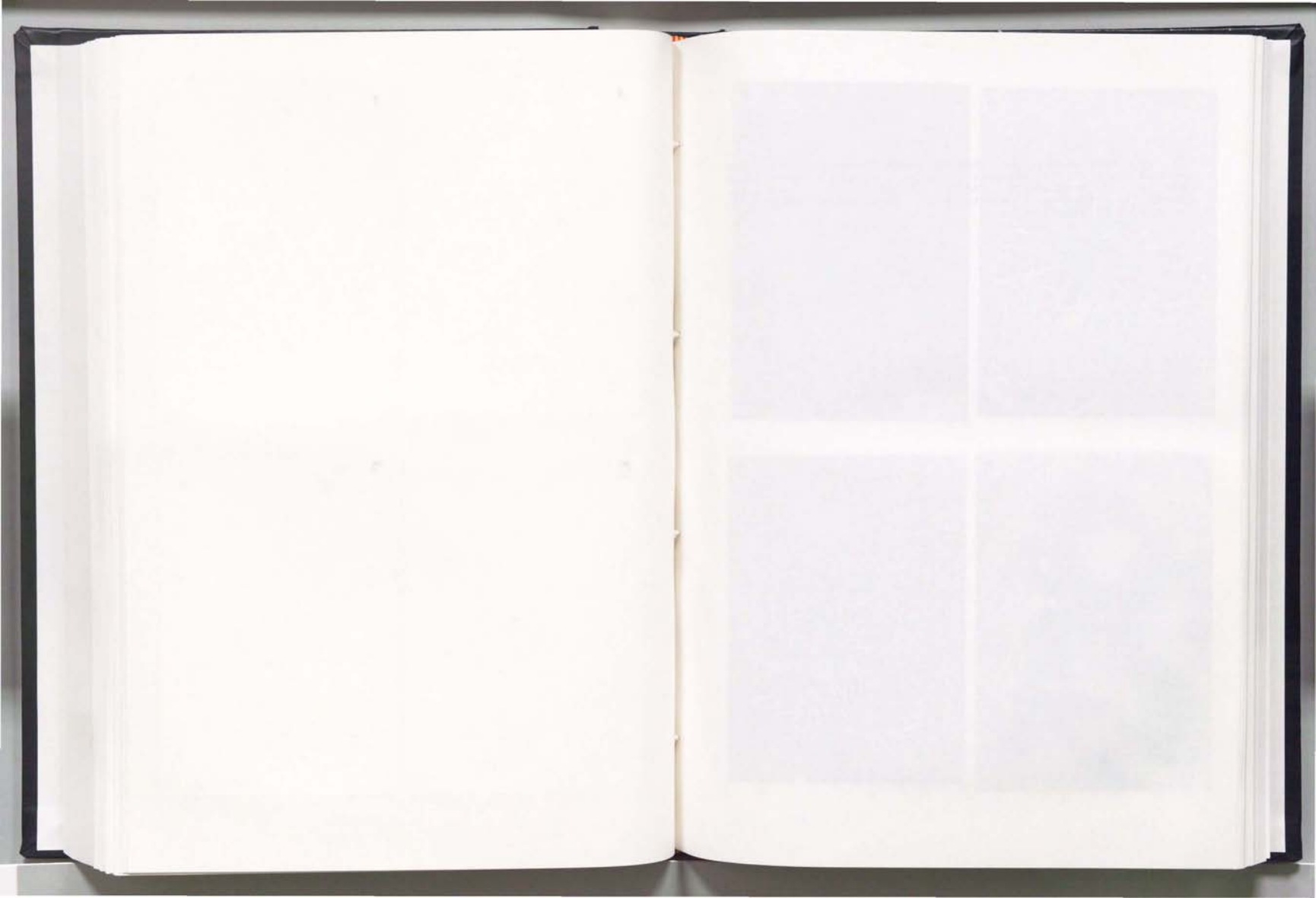

Fig. 20. Photomicrographs showing dendritic-spherulitic and compound spherulitic textures. (A),(B) Dendritic-spherulitic textures of hornblendes. (A:PPL). (B:BEI). (C) Dendritic-spherulitic textures of Garnets (BSE). (D) Compound spherulitic textures of feldspars (PPL).

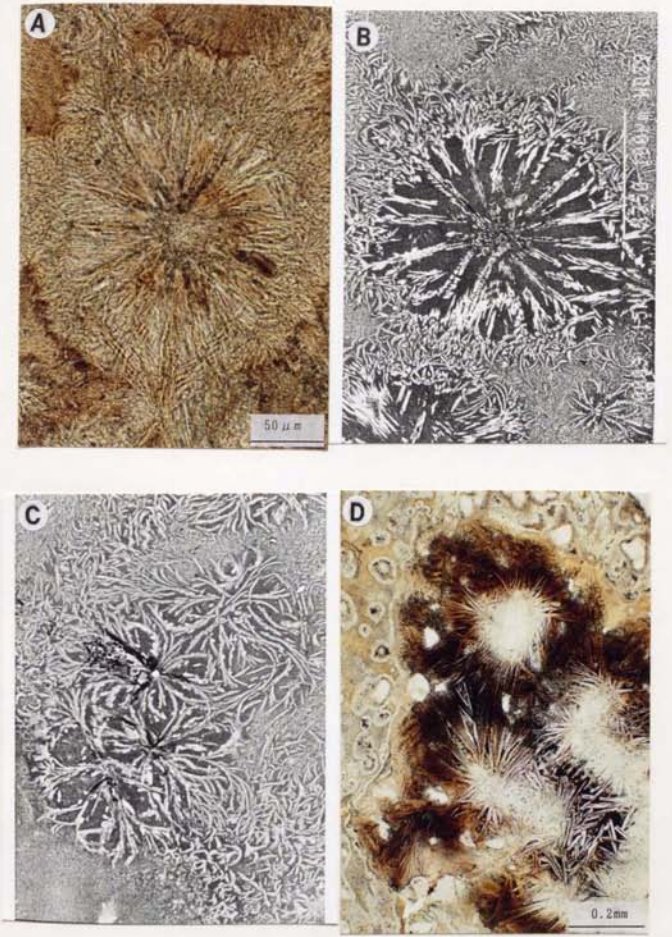

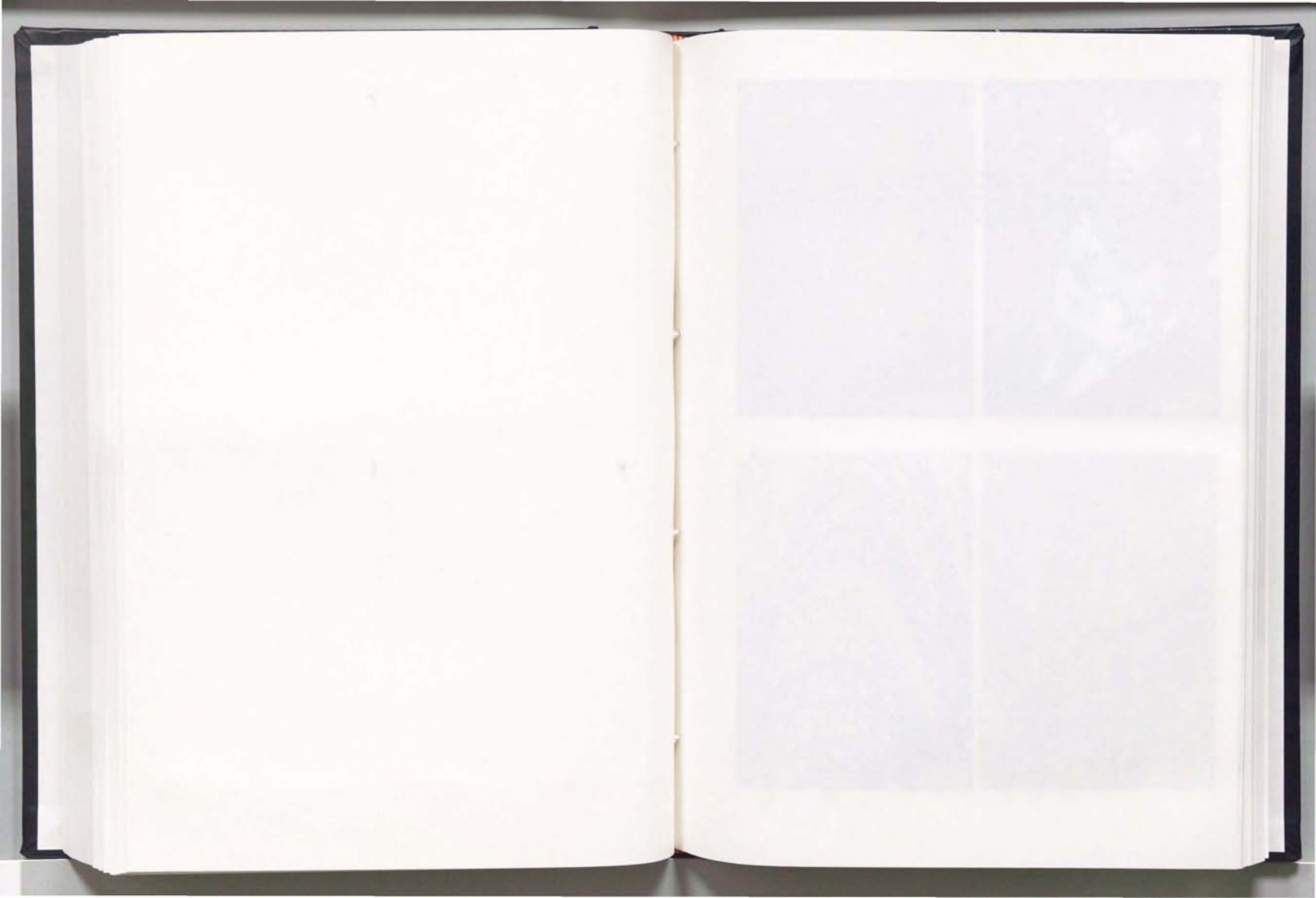

Fig. 21. Photomicrographs showing transparent glass having a silica composition and flow structures. (A),(B) Transparent glass having a silica composition around quartz fragments (PPL. CPL). (C) Flow structure similar to similar fold structure (PPL). (D) Flow lamellaes in glass matrix (PPL)

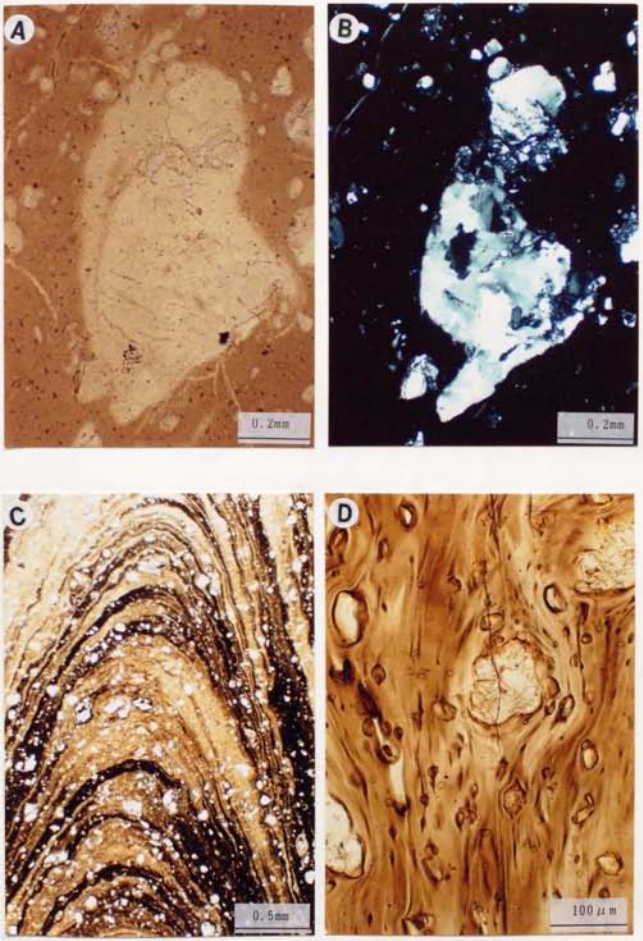

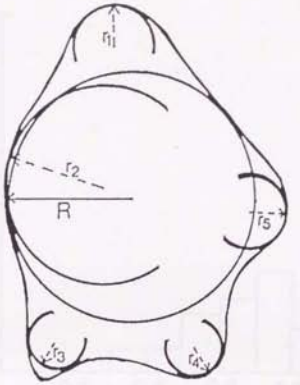


Fig. 22. Sketch showing roundness (Ro) of fragments. $Ro = \sum_{i=1}^{n} r_i / nR$.

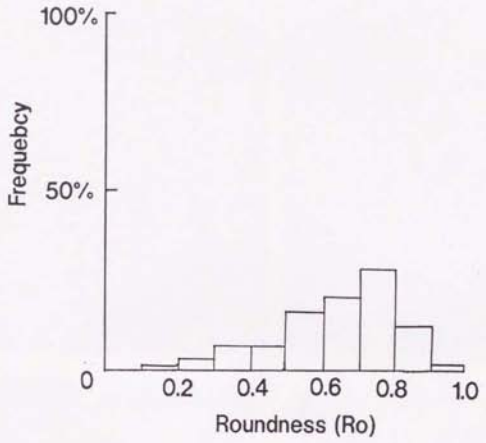


Fig. 23. Roundness-frequency diagram showing the roundness of fragments in the Fuyun pseudotachylites.

Fig. 24. Photomicrographs showing vesicle and amygdule textures in microcrystalline matrix (A:PPL, E,F:BSE) and glass matrix (B:PPL, C,D:BSE).

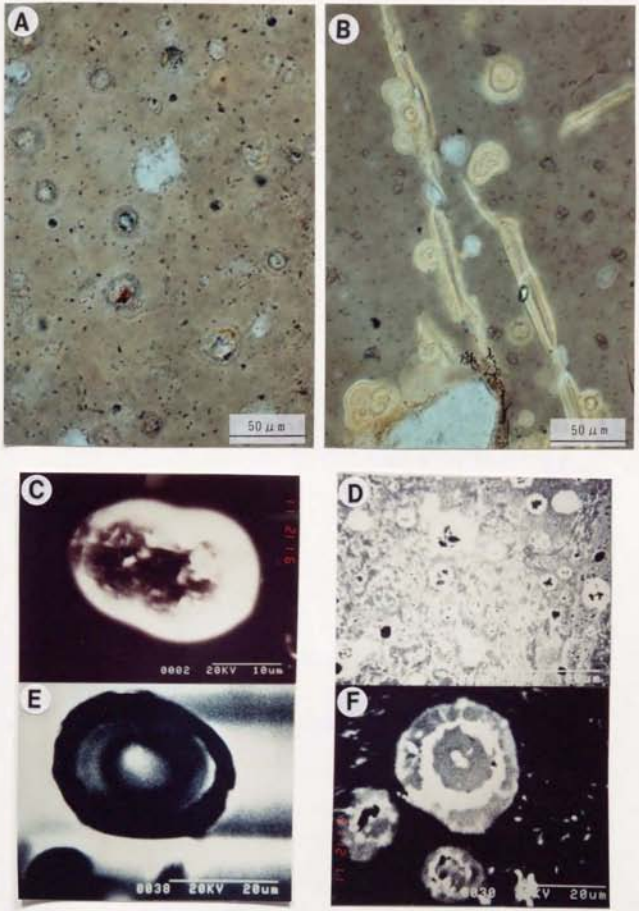

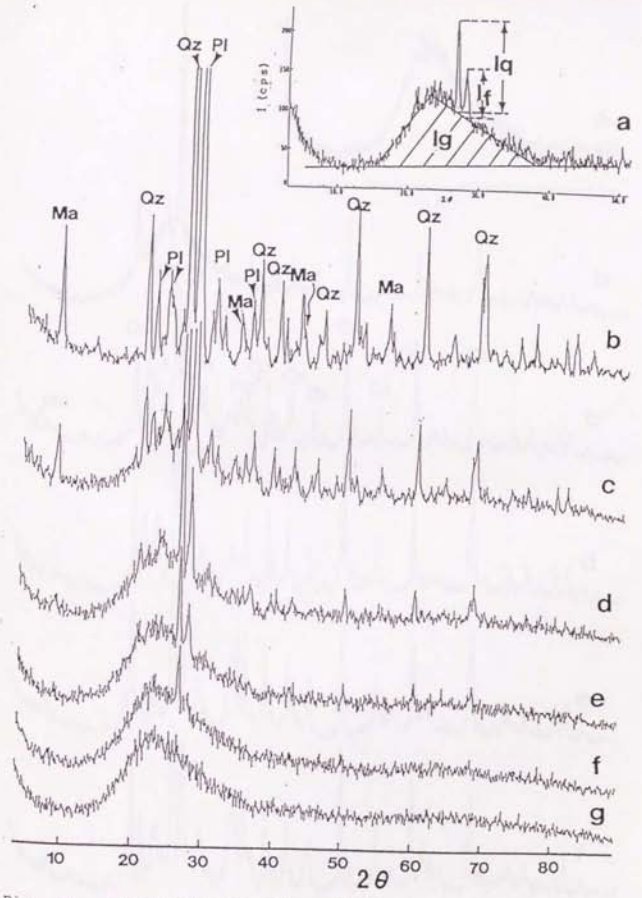


Fig. 25. Spectra of powder X-ray diffraction patterns of the standard samples. b-g represent the samples contained 0, 50, 80, 90, 95, 100 weight percent glass content respectively. Ig: integrated intensity of glass; Iq:intensity scattered by quartz; If:intensity scattered by feldspars (albite). Ma:micas; Qz:quartz; Pl:feldspars.

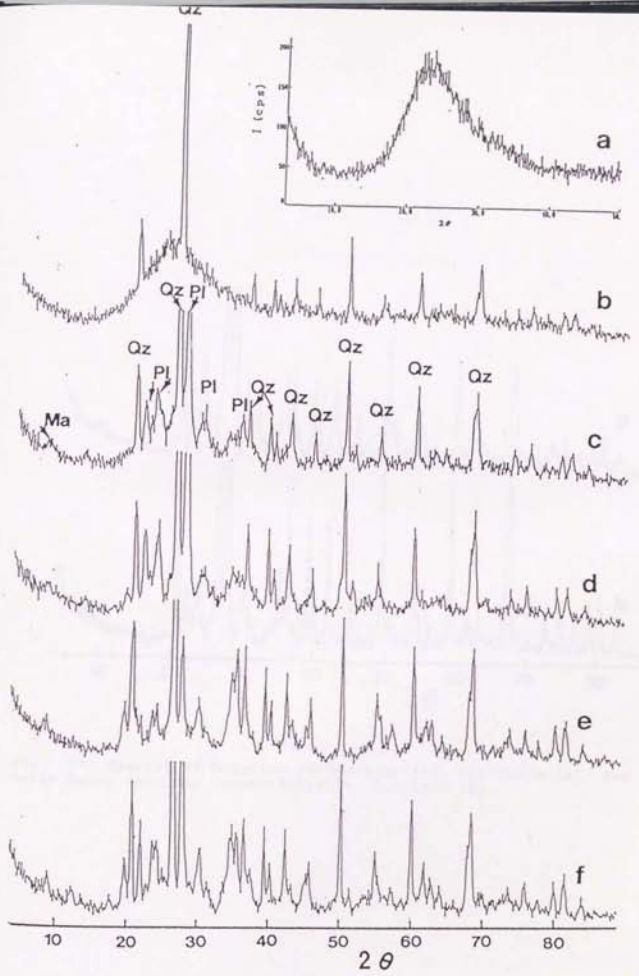


Fig. 26. Spectra of powder X-ray diffraction patterns of the Fuyun pseudotachylites. a:obsidian from Watatoke, central Japan; b:type-I vein; c:type-V vein; d:type-II vein; e:type-III vein; f:type-IV vein.

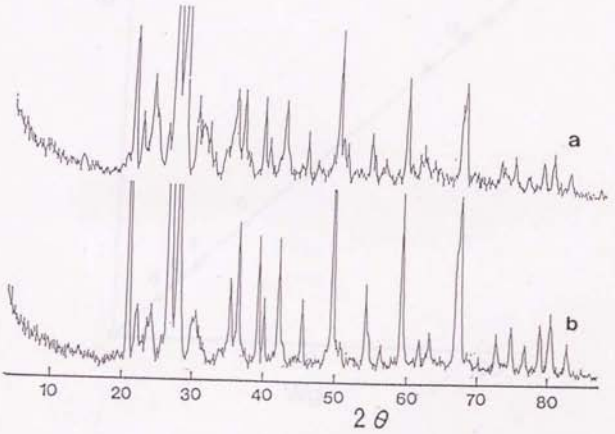


Fig. 27. Spectra of Musgrave pseudotachylite, Australia (a) and Outer Harry Hebrides pseudotachylite, Scotland (b).

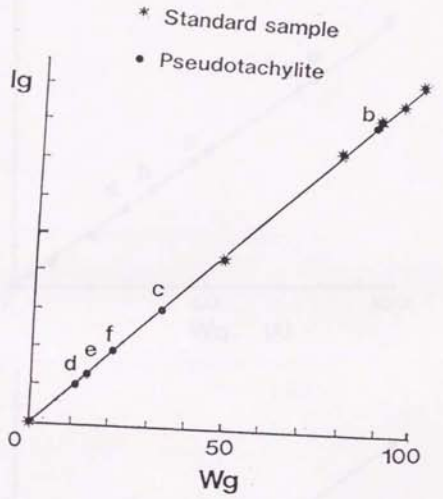


Fig. 28. Calibration curves of glass matrix. b-f corresponding to that shown in Fig. 26.

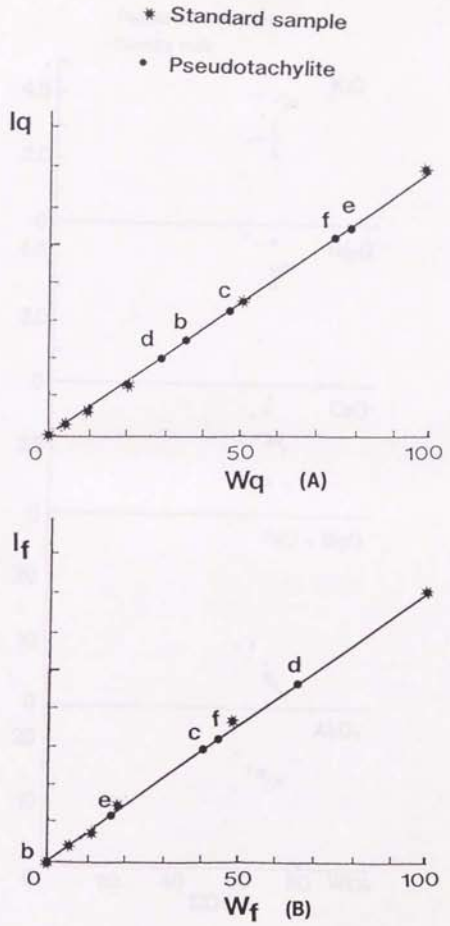


Fig. 29. Calibration curves of quartz crystalline (A) and feldspar (albite) crystalline (B). b-f corresponding to that shown in Fig. 28. b-f.

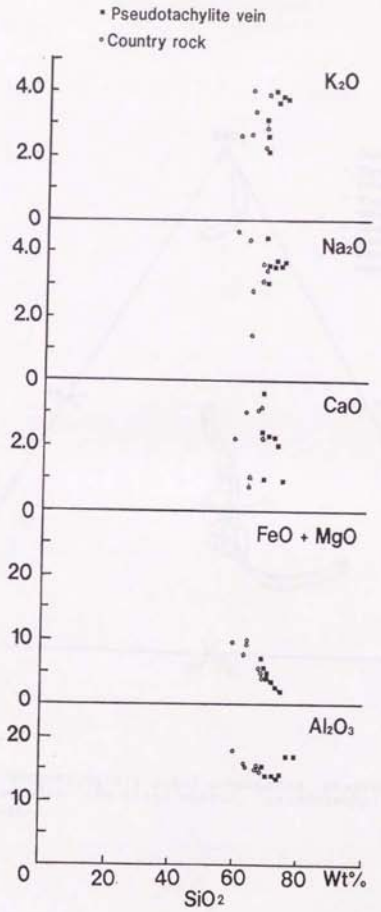


Fig. 30. Variation of oxides in the pseudotachylites and country rocks.

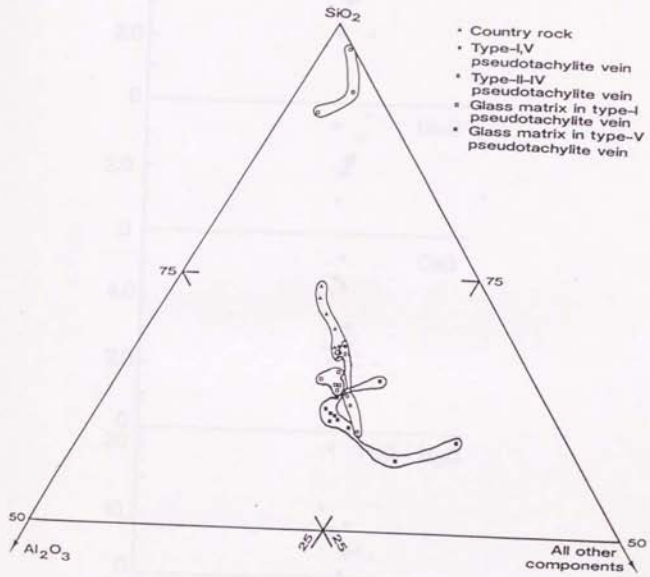


Fig. 31. $SiO_2$-$Al_2O_3$-all other components diagram showing the relation between the glass matrix, pseudotachylite veins and country rocks.

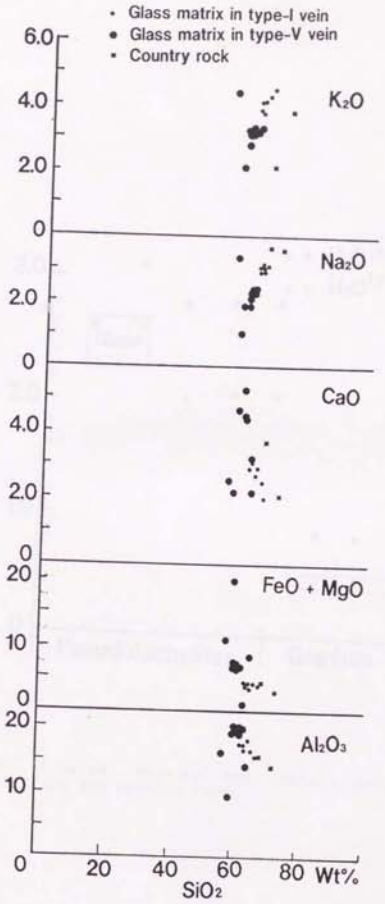


Fig. 32. Variation of oxides in glass matrices and country rocks.

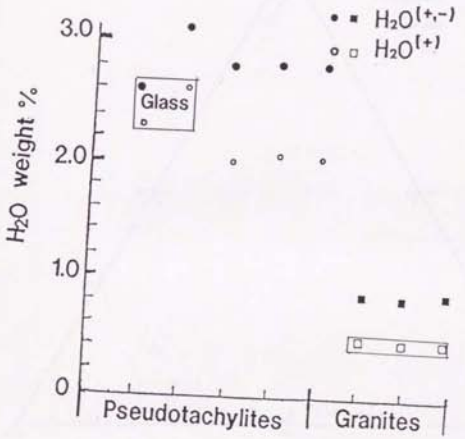


Fig. 33. Diagram showing the Water contents in the pseudotachylites and country rocks.

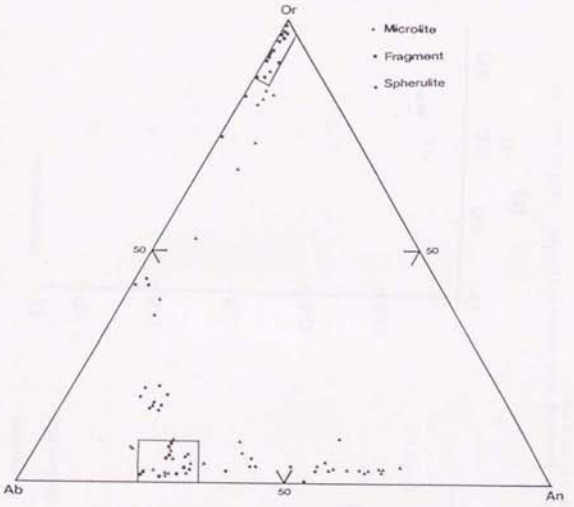


Fig. 34. Or-Ab-An diagram showing the compositional variation of feldspar microlites.

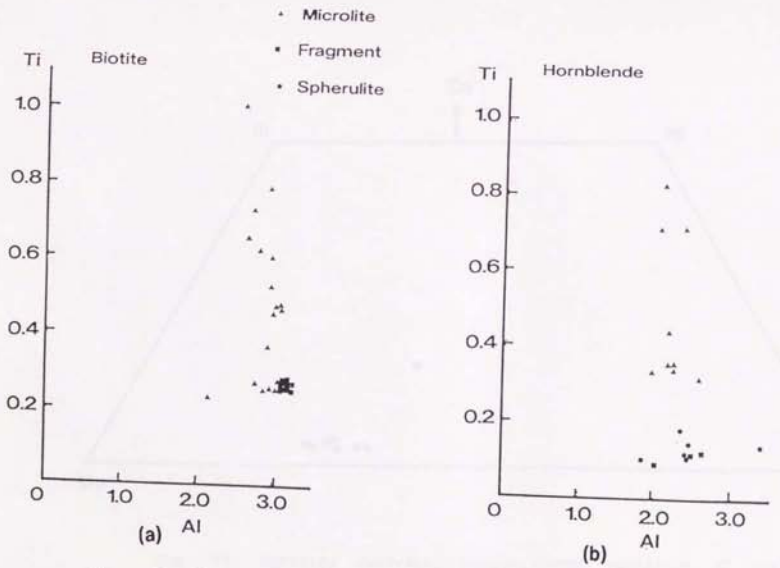


Fig. 35. Ti-Al diagrams showing the compositional variation of biotite and hornblende microlites.

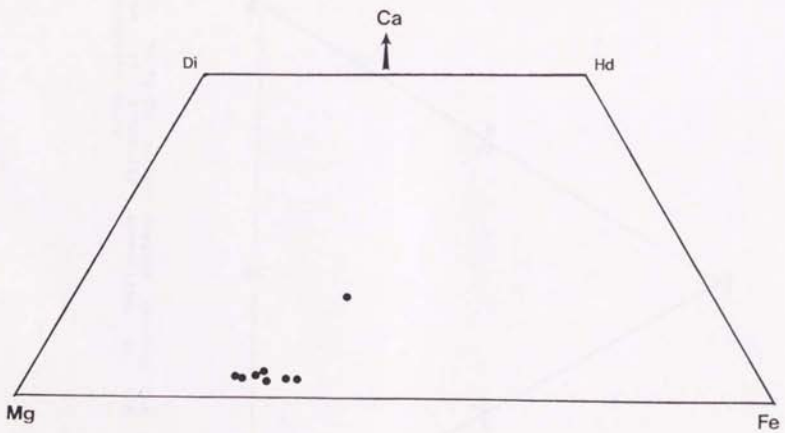


Fig. 38. Pyroxene quadrangle compositional variation of the pyroxene microlites in the microlitic pseudotachylite veins.

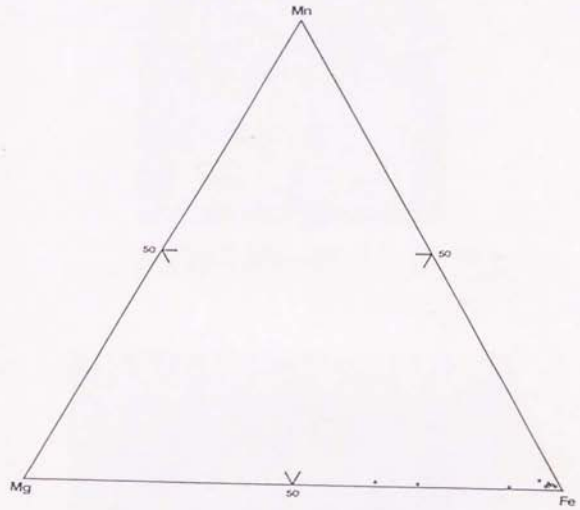


Fig. 37. Mn-Mg-Fe ternary diagram showing the compositional variation of grossular microlites in the microlitic pseudotachylite veins.

Fig. 38. Photographs showing the high-speed frictional testing machine. (A) High-speed testing machine; (1) a servo-motor (5.5 kw), (2)torque (3)torque gage, (4)electromagnetic clutch, (5)cylindrical specimen of 25 mm in diameter, (6)actuator for applying axial force, (7)motor controller. (B)The sparks generated by frictional heating flung out from the interface of two cylinder samples during experiment in gabbro sample.

A

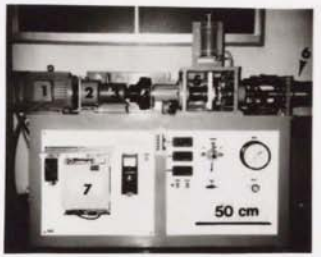


B

a
b
b
c
c

Fig. 39. Photomicrographs (A) and sketch (B) showing the texture of frictional surface generated in experiments. a:Center zone; b:middle zone; c:margin zone.

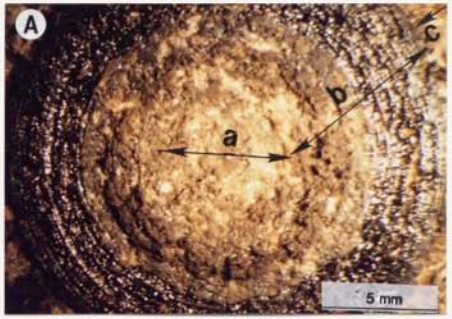


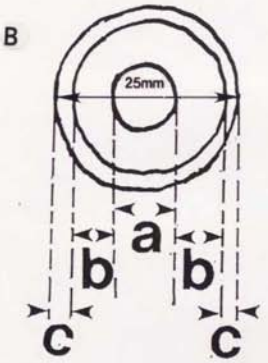

Fig. 40. Photomicrographs (SEM) showing the textures of frictional surfaces generated in experiment. (A),(B) Flow structures. (B) Enlarged part of (A). (C)Cavernous textures on frictional surface.

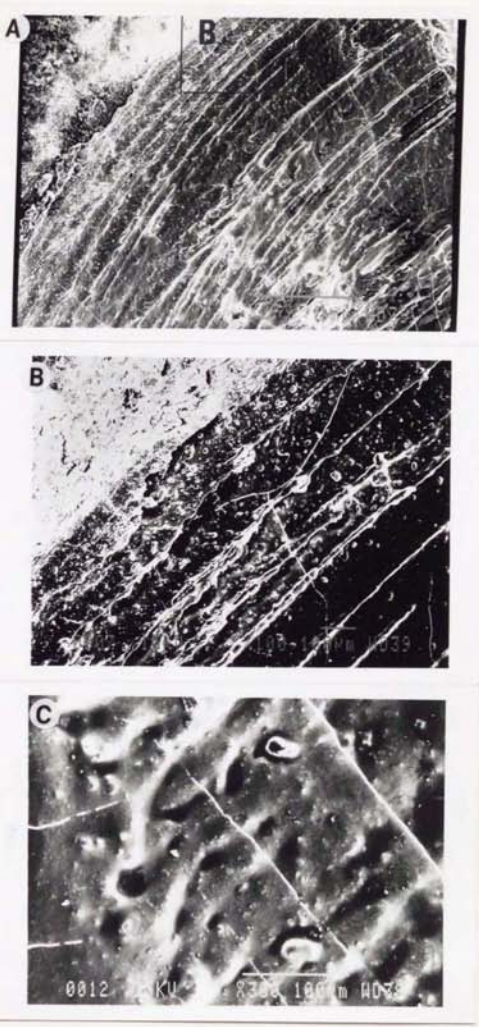

Fig. 41. Photomicrographs (BSE) showing the textures of pseudotachylite vein along the shear zone and network veins injected into the country rocks generated by frictional experiments in medium gabbro. (A),(B) were taken from the thin section parallel to the shear sense where the fragments were rounded and ranged parallel to the edge of pseudotachylite vein. (C) was taken from the thin section normal to the shear sense.

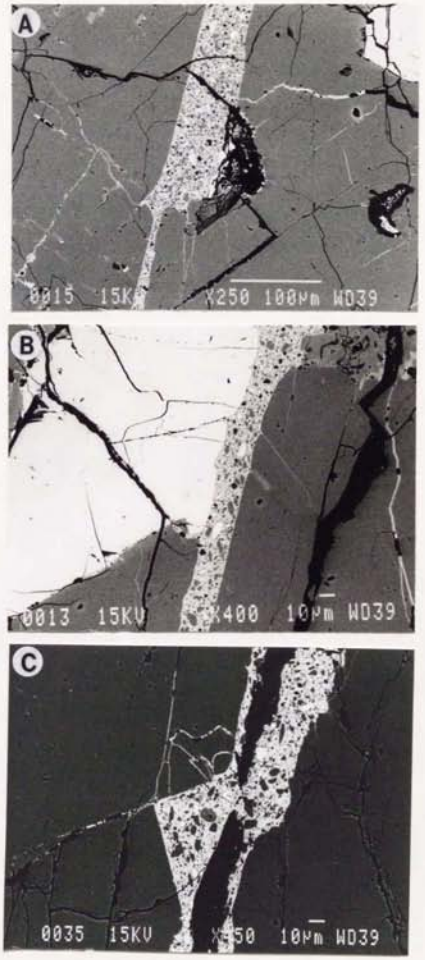

Fig. 42. Photomicrographs (BSE) showing the vesicular textures in the experimentally-generated pseudotachylites. (B):Enlarged part of (A).

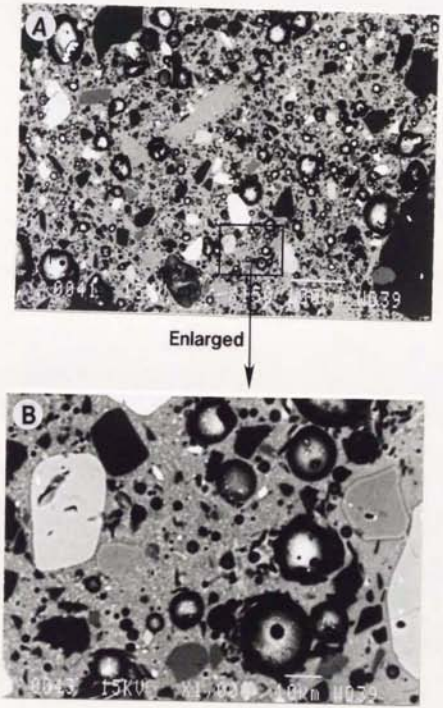

Fig. 43. Photomicrographs taken under stereoscope showing the textures on frictional surface generated by frictional experiments in the fine-grained granite (A) and the medium-grained granite (B). (A) Transparent melt flow parallel to the shear sense as fine hairs. (B) Biotite was fused and remained on frictional surface as black bands showing vitreous luster.

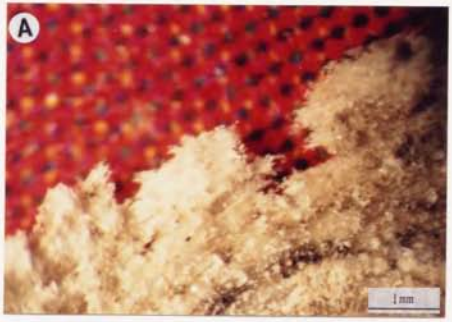


Fig. 44. Photomicrographs showing the textures of experimental pseudotachylites generated in the fine-grained granite samples. white bands shown in (A) and (B) are the glass matrix having a chemical composition similar to biotite contained in granite sample. (C),(D) showing the flow structures in glass matrix.

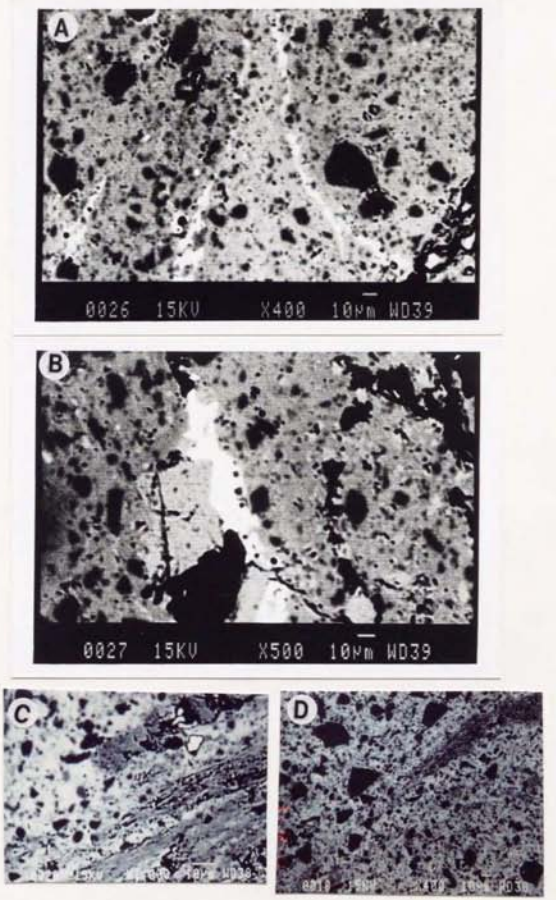

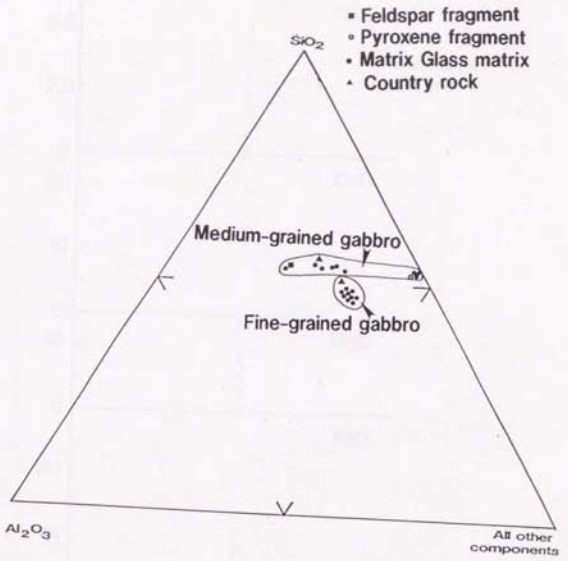


Fig. 45. $SiO_2$-$Al_2O_3$-all other components diagram showing the compositional variation of the glass matrix generated in fine-grained gabbro and medium-grained gabbros and host gabbros.

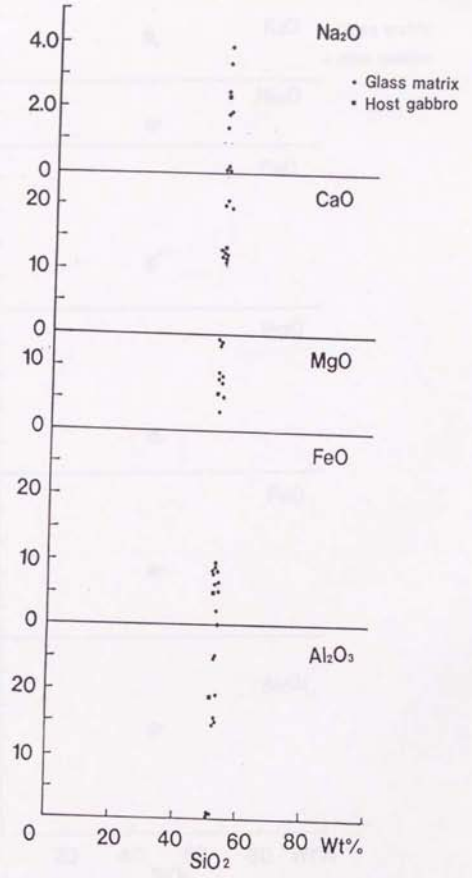


Fig. 46. Variation of oxides in glass matrix generated in medium-grained gabbro sample.

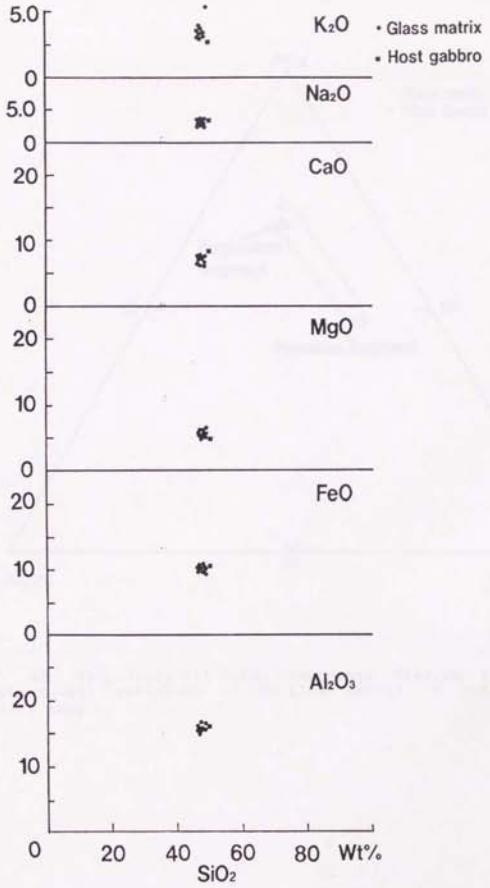


Fig. 47. Variation of oxides in glass matrix generated in fine-grained gabbro sample.

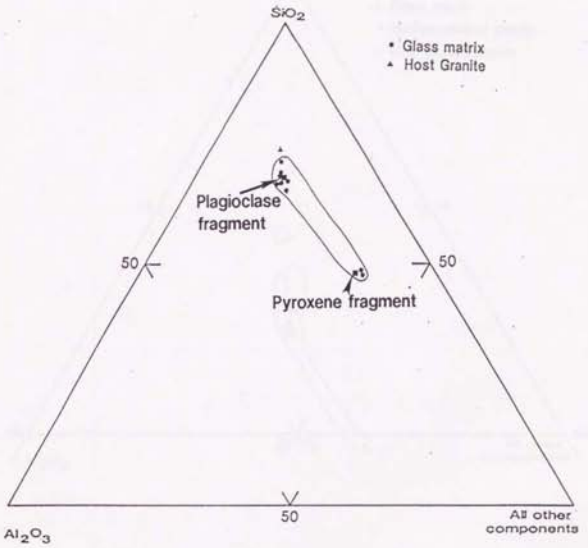


Fig. 48. $SiO_2$-$Al_2O_3$-all other components diagram showing the compositional variation of the glass matrix in coarse-grained granite sample.

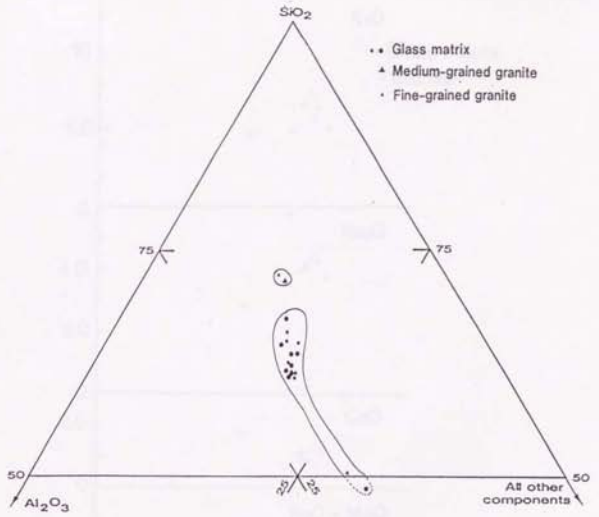


Fig. 49. $SiO_2$-$Ai_2O_3$-all other components diagram showing the compositional variation in glass matrices generated in fine-grained granite and medium-grained granite samples.

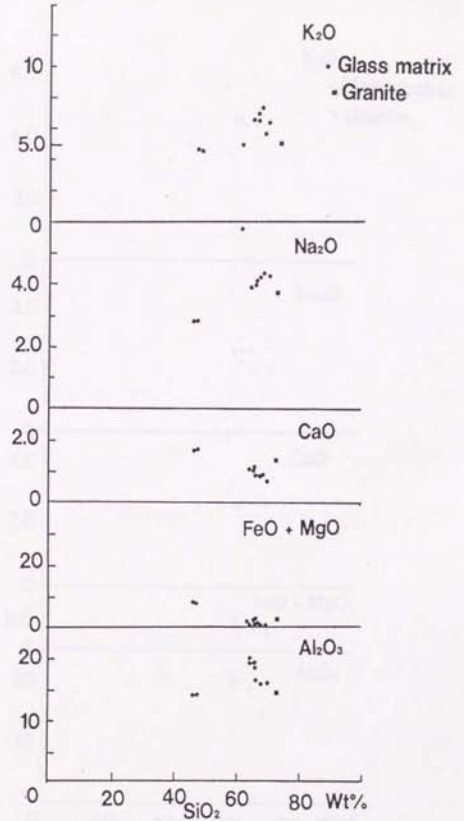


Fig. 50. Variation of oxides in glass matrix generated in coarse-grained granite sample.

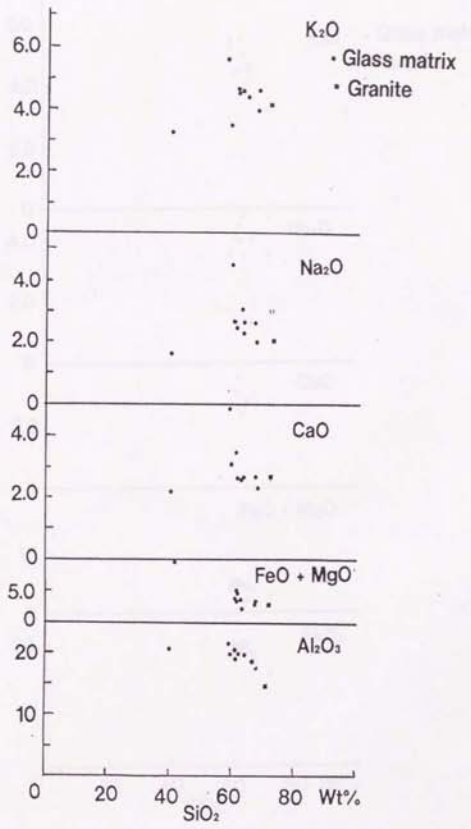


Fig. 51. Variation of oxides in glass matrix generated in medium-grained granite sample.

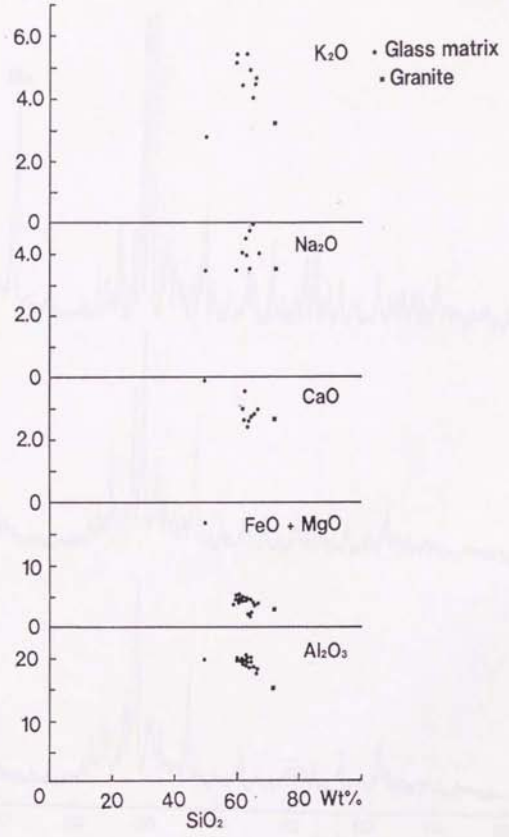


Fig. 52. Variation of oxides in glass matrix generated in fine-grained granite sample.

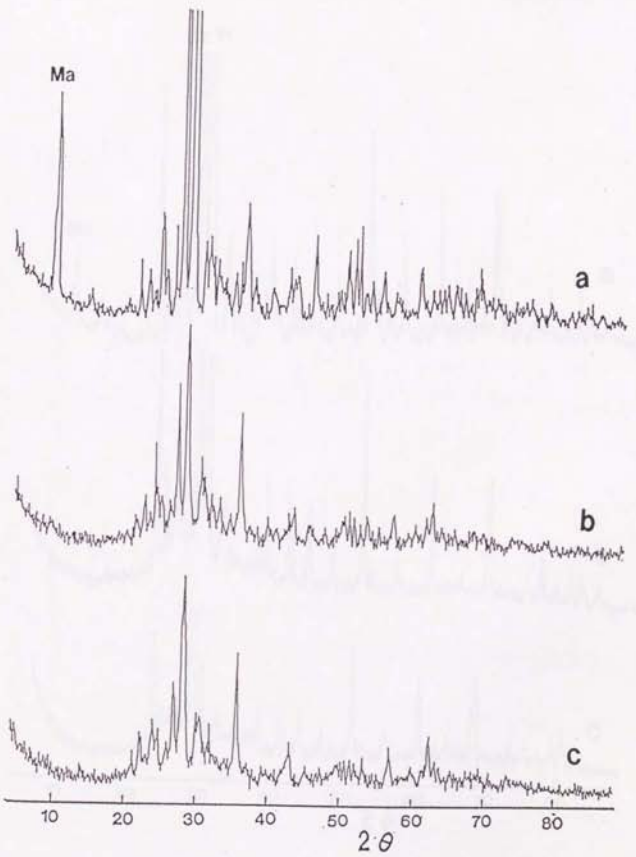


Fig. 53. Spectra of experimentally-generated pseudotachylites in fine-grained gabbro samples and host gabbro. a:Host gabbro. b,c:Experimentally-generated pseudotachylite.

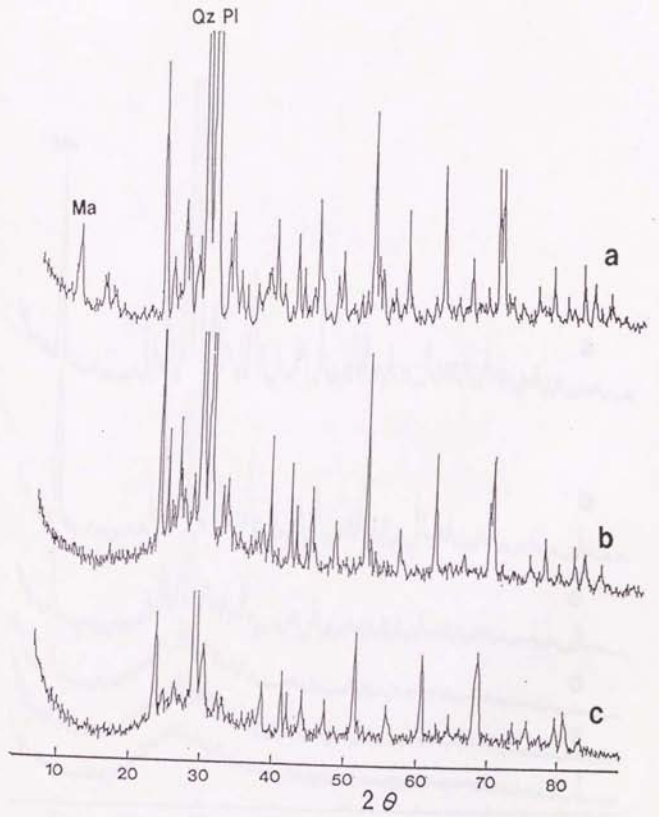


Fig. 54. Spectra of experimentally-generated pseudotachylites in fine-grained granite samples and host granite. a:Host granite. b,c:Experimental-generated pseudotachylite.

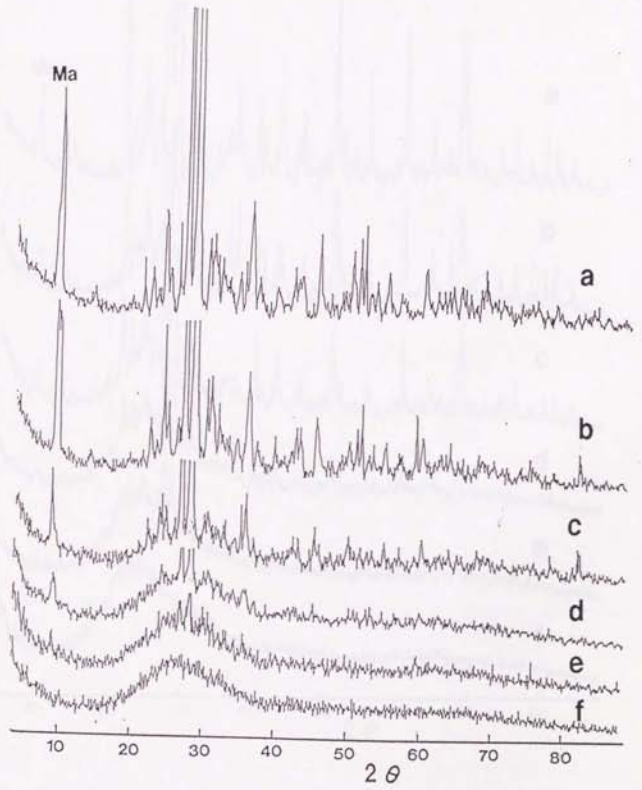


Fig. 55. Spectra of standard samples in fine-grained gabbro. a-f corresponding to 0, 10, 20, 50, 75 and 100 Wt.% glass content samples respectively.

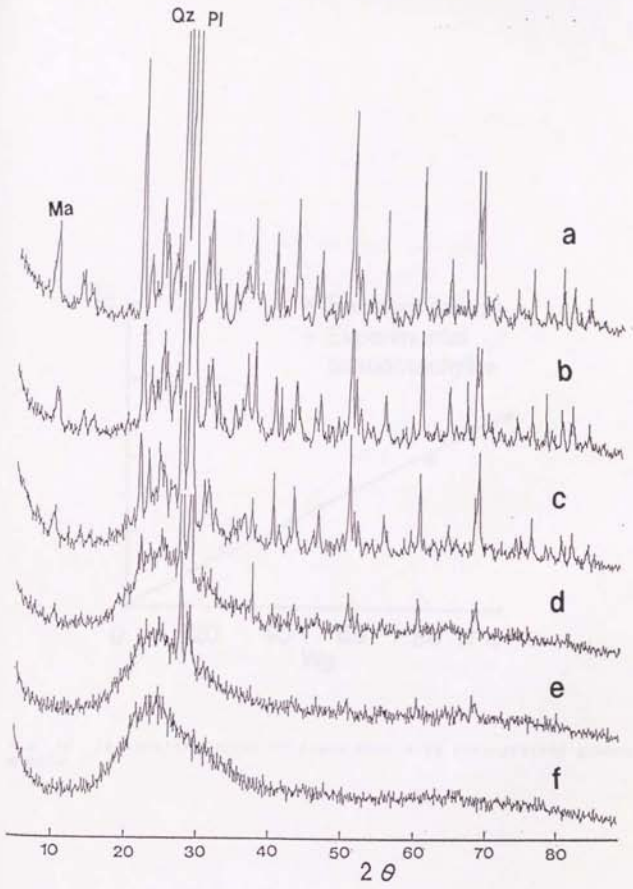


Fig. 56. Spectra of standard samples in fine-grained granite. a-f corresponding to 0, 10, 20, 50, 75 and 100 Wt.% glass content samples.

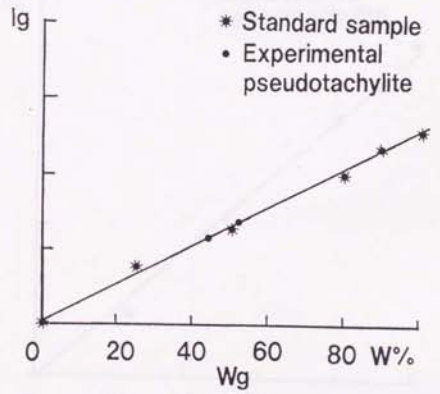


Fig. 57. Calibration curve of glass matrix in fine-grained gabbro sample.

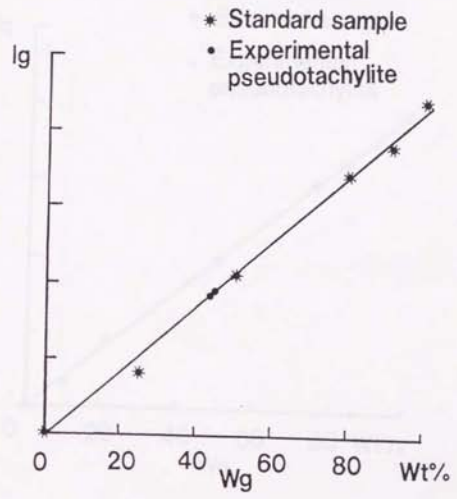


Fig. 58. Calibration curve of glass matrix in fine-grained granite sample.

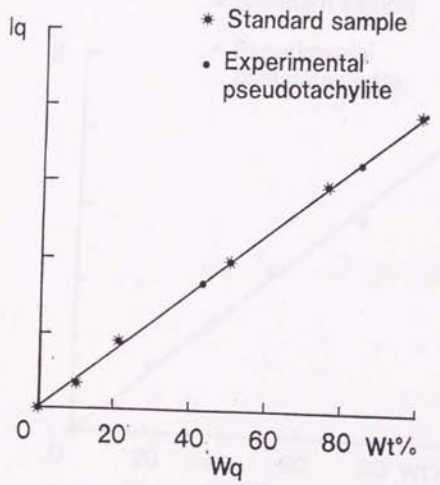


Fig. 59. Calibration curve of quartz crystalline in. fine-grained granite sample.

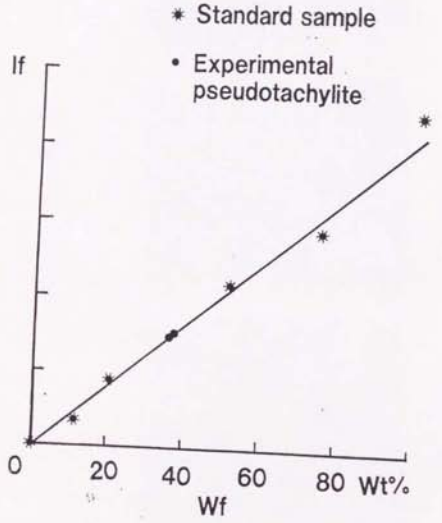


Fig. 60. Calibration curve of feldspar (albite) crystalline in fine-grained granite sample.

Fig. 61. Photomicrographs taken under stereoscope showing the textures of fused material generated in anorthosite sample (A, B) and albitite-quartzite pair samples (C, D).

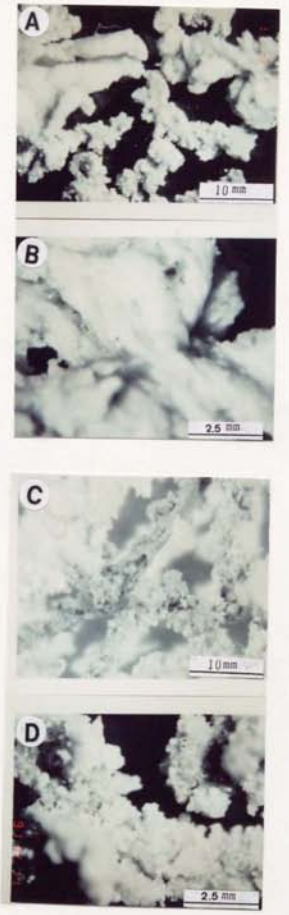

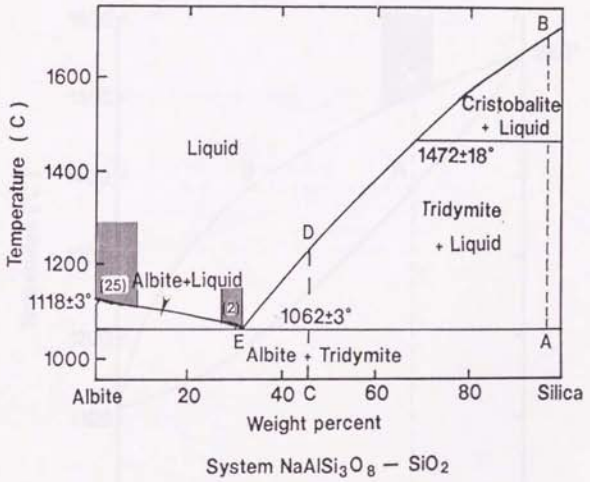


Fig. 62. $NaAlSi_3O_8$-$SiO_2$ binary diagram showing the chemical compositions (shaded parts, the numbers are measured points) of glass matrix generated in albitite-quartz pair samples.

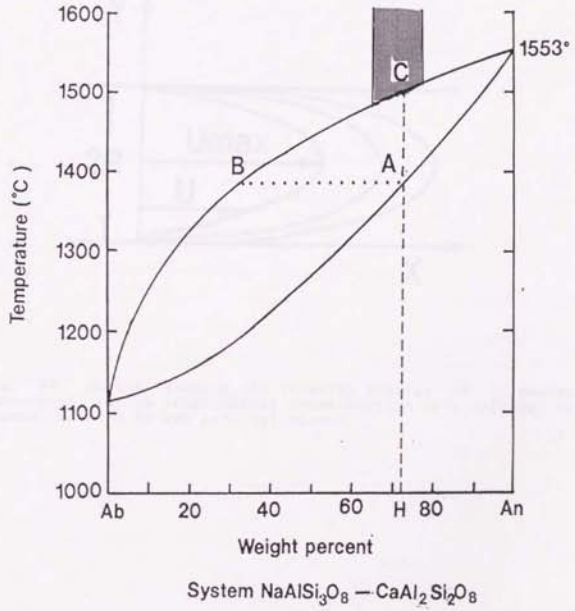


Fig. 63. $NaAlSi_3O_8$-$CaAl_2Si_2O_8$ solid system diagram showing the chemical compositions (shaded part) of glass matrix generated in anorthosite sample.

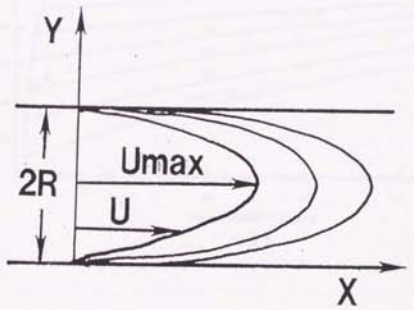


Fig. 64. Sketch showing the velocity profile of a newtonian suspension, in the longitudinal cross-section of a cylinder or a channel bounded by two parallel planes.

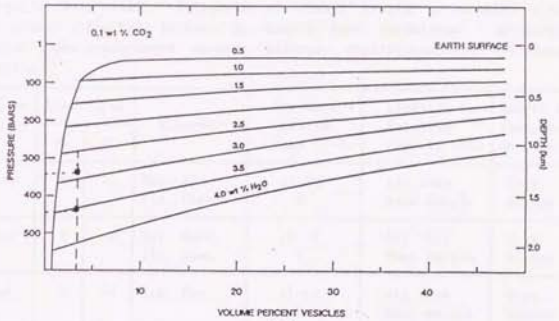


Fig. 65. Diagrams showing the relation between the volume percent of vesicles and pressure in andesitic melt. Initial $CO_2$ 0.1 Wt.% in (A) and 0.2 Wt.% in (B), initial water 0.5, 1.0, 1.5, 2.0, 2.5, 3.0, 3.5 and 4.0 Wt.% in (A) and (B).

Table 1. The basic morphologies of simple shape and skeletal microlites in the pseudotachylite veins from the Fuyun fault zone, northwest China. Terminology after (1):A.G.I (1980); (2):Lofgren (1974); (3):this study shown in sketches; (4):Ross (1962). D:Diameter of sighal crystal or crystal fiber. Pla:Plagioclase; Alk:Alkali felspar; Qz: Quartz; Horn: Hornblende; Gar:Garnet; Bio:Biotite; Opaq:unmearsured opaque mineras; Crys:Crystalline; Spi:Spinel; Ill:Illmenite.

| Morphologies a-k shown in sketches | Size ($\mu$m) | | Mineral | Pseudotachylite type II-V | Location in Pseudotachylite vein | Matrix of pseudotachylite |
|---|---|---|---|---|---|---|
| | <D | <L | | | | |
| a. Spicular (1) | 6 | 10 | Bio. Alk. Pla. Horn. | II-IV<br>V | All vein<br>Near margin | Crys.<br>Glassy |
| b. Granular (3) | 8 | 8 | Spi. Horn. Ill. Opaq. | II-IV<br>V | All vein<br>Near margin | Crys.<br>Glassy |
| c. Crossed (3) | 6 | 50 | Alk. Pla. | II-IV<br>V | All vein<br>Near margin | Crys.<br>Glassy |
| d.Accicular-lath (4) | 15 | 150 | Bio. Pla. Horn. | II-IV | All vein | Crys. |
| e. Trichitic (4) | 2 | 100 | Opaq. | V | Near margin | Glass |
| f.spider-like (4) | 6 | 20 | Alk. Pla. Opaq | V | Near margin | Glass |
| g. Tabular-skeltal (2) | 10 | 100 | Horn. Pla. Bio. | II-IV | Near center | Crys. |
| h. Dendritic skeltal (3) | 8 | 150 | Horn. Ill. Opaq. | III-IV | Near center | Crys. |
| i. Box-skeltal (3) | 6 | 10 | Horn. Ill. Opaq. | II-IV | Near center | Crys. |
| j. Chain (3) | 6 | 10 | Horn. Bio. Opaq. Ill. | III-IV | Near center | Crys. |

Table 2. The basic morphologies of dendritic microlites in the pseu- dotachylite veins from the Fuyun fault zone, northwestern China. Terminology after (1) :A.G.I (1980); (2):Lofgren (1974); (3):this study shown in sketches. D:Diameter of signal crystal or crystal fiber. Pla:Plagioclase; Alk:Alkali felspar; Qz: Quartz; Amph: Amphibole; G ar:Garnet; Bio:Biotite; Maf:unmearsured mafic mineras; Crys:Crystalline.

| Morphologies a-k shown in sketches | Size ($\mu$m) | | Mineral | Pseudotachylite type II-V | Location in Pseudotachylite vein | Matrix of pseudotachylite |
|---|---|---|---|---|---|---|
| | <D | <L | | | | |
| a.Scoplitic (1) | 2 | 10 | Opaq. | V | near margin | Glass |
| b. Feathery (1) | 8 | 10 | Pla. Opaq. | III-IV<br>V | Near center<br>Near margin | Crys.<br>Glass |
| c. Quartz-feathery(1) | 2 | 50 | Quartz | IV | Near center | Crys. |
| d. Broomy (3) | 8 | 50 | Pla. Bio. Amph. Opaq. | III-IV | Near center | Crys. |
| e.Fir-like (3) | 8 | 80 | Pla. Horn. Bio. | III-IV | Near center | Crys. |
| f. Branching (3) | 7 | 100 | Gro. Horn. Opaq. | III-IV | Near center | Crys. |
| g. Pine-like (3) | 8 | 80 | Pla. Bio. Horn. Opaq. | III-IV | Near center | Crys. |

Table 3. The basic morphologies of spherulitic microlites in the pseudotachylite veins from the Fuyun fault zone, northwestern China. Terminology after (1): A.G.I (1980); (2): Lofgren (1974); (3):this study shown in sketches. D:Diameter of signalcrystal fiber. L:Length of signal crystal fiber. Pla:Plagioclase; Alk:Alkalifelspar; Anor:Anorthoclase. Qz:Quartz; Amph:Amphibole; Gar:Garnet; Bio:Biotite;Opaq:unmearsured opaque minerals; Crys:Crystalline.

| Morphologies a-k shown in sketches | Size(μm) | | Mineral | Pseudotachylite type III-V | Location in pseudotachylite vein | Matrix of pseudotachylite |
|---|---|---|---|---|---|---|
| | < D | < L | | | | |
| a. Globular (1) | 6 | 10 | Alk. Pla | IV-V | Near margin | Glass or Glassy |
| b. Fan (2) | 5 | 130 | Anor. | V | Near center | Glass |
| c. Bow-tie (2) | 5 | 130 | Anor. | V | Near center | Glass |
| d. Spherulitic (2) | 5 | 130 | Anor. | V | Near center | Glass |
| e. Spherical (3) | 3 | 10 | Pla. Opaq. Bio. | III-IV V | in center | Crys. Glass |
| f. Sheaf (2) | 15 | 150 | Pla. | III-IV | in center | Crys. |
| g. Sheaves aggrgate (3) | 15 | 150 | Pla. | III-IV | in center | Crys. |
| h.Overgrowth (3) | 10 | 150 | Pla. Bio. Amph. Opaq. | III-V | in center | Crys. Glassy |
| i. Stellate (2) | 10 | 150 | Pla.Bio.Amph Gar. Opaq. | III-IV | in center | Crys. |
| j.Dendritic (3) | 10 | 200 | Gar.Amph.Bio Pla. Opaq. | III-IV | in center | Crys. |
| k. Compound (3) | 10 | 200 | Pla.Gar.Bio Amph. Opaq. | III-IV | in center | Crys. |

Table 4. Chemical compositions of pseudotachylites analysed by XRF. The water contents ($H_2O^+$ and $H_2O^-$) were determined by independently ignition loss, which was corrected for oxidation ironusing FeO content in this table, also made in table 5. FeO*:total Fe as FeO, all in this study.

| Wt% | A-1 | A-2 | A-3 | A-4 | A-5 | A-6 | A-7 |
|---|---|---|---|---|---|---|---|
| $SiO_2$ | 68.52 | 67.82 | 67.57 | 62.86 | 59.77 | 63.53 | 63.90 |
| $TiO_2$ | 0.46 | 0.47 | 0.48 | 0.70 | 0.54 | 0.71 | 0.59 |
| $Al_2O_3$ | 14.55 | 15.53 | 15.31 | 16.84 | 17.74 | 16.50 | 16.66 |
| FeO* | 3.60 | 4.42 | 4.10 | 5.33 | 5.04 | 6.72 | 6.20 |
| MnO | 0.08 | 0.09 | 0.08 | 0.07 | 0.06 | 0.10 | 0.13 |
| MgO | 0.64 | 1.28 | 1.20 | 2.47 | 4.52 | 3.39 | 2.78 |
| CaO | 2.28 | 3.24 | 3.19 | 3.01 | 2.31 | 1.03 | 0.75 |
| $Na_2O$ | 3.51 | 3.11 | 3.77 | 4.40 | 4.64 | 1.40 | 2.85 |
| $K_2O$ | 3.96 | 2.93 | 2.26 | 2.69 | 2.51 | 4.07 | 3.48 |
| $P_2O_5$ | 0.14 | 0.13 | 0.14 | 0.22 | 0.12 | 0.17 | 0.13 |
| $H_2O^+$ | 2.34 | 2.65 | 2.05 | 2.10 | 2.11 | 3.24 | 3.15 |
| $H_2O^-$ | 0.26 | 0.55 | 0.81 | 0.81 | 0.83 | | |
| Total $H_2O$ | 2.60 | 3.21 | 2.87 | 2.91 | 2.94 | 3.24 | 3.15 |

Table 5. Bulk compositions of the country rocks where the pseudotachylites injected analysed by XRF.

| Wt% | B-1 | B-2 | B-3 | B-4 | B-5 | B-6 | B-7 |
|---|---|---|---|---|---|---|---|
| $SiO_2$ | 68.12 | 72.77 | 71.32 | 69.75 | 74.13 | 68.00 | 67.15 |
| $TiO_2$ | 0.42 | 0.25 | 0.32 | 0.48 | 0.21 | 0.50 | 0.50 |
| $Al_2O_3$ | 15.15 | 13.98 | 14.10 | 14.28 | 13.83 | 15.83 | 15.83 |
| FeO* | 3.65 | 2.10 | 2.95 | 3.73 | 1.81 | 4.87 | 3.95 |
| MnO | 0.09 | 0.05 | 0.07 | 0.06 | 0.03 | 0.10 | 0.08 |
| MgO | 1.24 | 0.49 | 0.63 | 0.67 | 0.47 | 2.43 | 1.94 |
| CaO | 3.60 | 2.00 | 2.28 | 2.31 | 0.95 | 0.99 | 2.42 |
| $Na_2O$ | 3.67 | 3.57 | 3.77 | 3.61 | 3.73 | 3.10 | 4.48 |
| $K_2O$ | 2.10 | 3.88 | 3.63 | 4.01 | 3.80 | 3.14 | 2.66 |
| $P_2O_5$ | 0.13 | 0.07 | 0.10 | 0.14 | 0.12 | 0.14 | 0.11 |
| $H_2O^+$ | 0.54 | 0.51 | 0.83 | 0.52 | 0.94 | 0.93 | 0.89 |
| $H_2O^-$ | 0.38 | 0.34 | | 0.43 | | | |
| Total $H_2O$ | 0.92 | 0.84 | 0.83 | 0.95 | 0.94 | 0.93 | 0.89 |

Table 6. Chemical compositions of glass matrix in type-I pseudotachylite analyzed by EDX.

| | Glass matrix in glass pseudotachylite | | | | | | | | |
|---|---|---|---|---|---|---|---|---|---|
| Wt% | Glas1 | Glas2 | Glas3 | Glas4 | Glas5 | Glas6 | Glas7 | Glas8 | Glas9 |
| $SiO_2$ | 67.32 | 63.90 | 63.50 | 64.94 | 64.41 | 65.73 | 97.41 | 92.68 | 88.52 |
| $TiO_2$ | 0.56 | 0.59 | 0.64 | 0.60 | 0.58 | 0.59 | 0.00 | 0.07 | 0.30 |
| $Al_2O_3$ | 15.52 | 17.44 | 17.26 | 18.03 | 16.92 | 16.41 | 0.00 | 2.24 | 6.13 |
| $Cr_2O_3$ | 0.05 | 0.07 | 0.00 | 0.02 | 0.00 | 0.01 | 0.00 | 0.03 | 0.00 |
| FeO* | 3.07 | 3.35 | 3.43 | 3.40 | 3.49 | 3.31 | 0.00 | 0.81 | 0.63 |
| MnO | 0.08 | 0.14 | 0.10 | 0.13 | 0.09 | 0.08 | 0.00 | 0.00 | 0.08 |
| MgO | 0.66 | 0.85 | 0.92 | 0.86 | 0.68 | 0.75 | 0.00 | 0.03 | 0.08 |
| CaO | 2.00 | 2.81 | 3.01 | 2.93 | 2.68 | 2.48 | 0.00 | 0.70 | 0.31 |
| $Na_2O$ | 3.05 | 3.04 | 3.02 | 3.16 | 2.97 | 2.84 | 0.09 | 0.36 | 2.00 |
| $K_2O$ | 4.56 | 4.13 | 3.83 | 3.99 | 4.07 | 4.30 | 0.00 | 0.00 | 1.52 |
| $P_2O_5$ | 0.49 | 0.59 | 0.38 | 0.55 | 0.44 | 0.62 | 0.73 | 0.16 | 0.11 |
| NiO | 0.00 | 0.11 | 0.01 | 0.00 | 0.02 | 0.06 | 0.04 | 0.00 | 0.00 |
| Total | 97.36 | 97.02 | 96.08 | 98.95 | 96.36 | 97.18 | 98.14 | 97.08 | 99.73 |
| Number of ions on the basis of twenty-four oxygens | | | | | | | | | |
| Si | 9.199 | 8.827 | 8.848 | 8.801 | 8.940 | 9.018 | 11.90 | 11.60 | 11.04 |
| Ti | 0.057 | 0.061 | 0.067 | 0.061 | 0.061 | 0.061 | 0.000 | 0.006 | 0.028 |
| Al | 2.500 | 2.840 | 2.834 | 2.879 | 2.768 | 2.654 | 0.000 | 0.331 | 0.900 |
| Cr | 0.005 | 0.008 | 0.000 | 0.002 | 0.000 | 0.001 | 0.000 | 0.003 | 0.000 |
| Fe | 0.351 | 0.387 | 0.399 | 0.419 | 0.405 | 0.380 | 0.000 | 0.331 | 0.070 |
| Mn | 0.009 | 0.017 | 0.011 | 0.015 | 0.011 | 0.009 | 0.000 | 0.000 | 0.008 |
| Mg | 0.134 | 0.174 | 0.190 | 0.173 | 0.140 | 0.154 | 0.000 | 0.005 | 0.000 |
| Ca | 0.293 | 0.416 | 0.449 | 0.426 | 0.398 | 0.364 | 0.022 | 0.093 | 0.041 |
| Na | 0.807 | 0.814 | 0.815 | 0.831 | 0.799 | 0.756 | 0.000 | 0.088 | 0.485 |
| K | 0.794 | 0.728 | 0.681 | 0.690 | 0.721 | 0.753 | 0.000 | 0.000 | 0.243 |
| P | 0.057 | 0.069 | 0.045 | 0.063 | 0.052 | 0.072 | 0.075 | 0.017 | 0.012 |
| Ni | 0.000 | 0.012 | 0.001 | 0.000 | 0.003 | 0.007 | 0.003 | 0.000 | 0.000 |
| Total | 14.205 | 14.354 | 14.341 | 14.359 | 14.297 | 14.230 | 12.000 | 12.243 | 12.831 |

Table 7. Chemical compositions of glass matrix in type-V pseudotachylite analyzed by EDX.

| | Glass matrix in mixed type pseudotachylite | | | | | | | | |
|---|---|---|---|---|---|---|---|---|---|
| Wt% | Gla10 | Gla11 | Gla12 | Gla13 | Gla14 | Gla15 | Gla16 | Gla17 | Gla18 |
| $SiO_2$ | 62.01 | 61.77 | 61.59 | 61.16 | 60.09 | 60.84 | 64.75 | 57.06 | 59.05 |
| $TiO_2$ | 0.59 | 0.62 | 0.55 | 0.68 | 0.57 | 0.42 | 0.36 | 0.50 | 0.28 |
| $Al_2O_3$ | 19.06 | 18.92 | 18.91 | 18.76 | 18.00 | 19.25 | 13.26 | 15.63 | 9.65 |
| $Cr_2O_3$ | 0.04 | 0.07 | 0.04 | 0.00 | 0.02 | 0.00 | 0.01 | 0.00 | 0.00 |
| FeO* | 4.28 | 4.32 | 4.28 | 3.67 | 4.62 | 5.24 | 7.47 | 8.55 | 16.88 |
| MnO | 0.21 | 0.11 | 0.05 | 0.00 | 0.06 | 0.12 | 0.08 | 0.17 | 0.17 |
| MgO | 1.68 | 1.55 | 1.56 | 1.56 | 2.14 | 1.71 | 1.08 | 2.73 | 2.29 |
| CaO | 4.39 | 4.32 | 4.28 | 3.67 | 4.62 | 5.24 | 2.17 | 2.43 | 2.21 |
| $Na_2O$ | 2.37 | 2.22 | 2.29 | 2.03 | 1.81 | 1.80 | 2.85 | 3.43 | 1.02 |
| $K_2O$ | 3.08 | 3.33 | 3.32 | 3.62 | 3.16 | 2.84 | 3.34 | 4.39 | 2.13 |
| $P_2O_5$ | 0.36 | 0.35 | 0.31 | 0.66 | 0.37 | 0.36 | 0.18 | 0.20 | 0.37 |
| NiO | 0.21 | 0.02 | 0.17 | 0.03 | 0.02 | 0.00 | 0.04 | 0.00 | 0.09 |
| Total | 98.23 | 97.64 | 97.42 | 96.90 | 97.57 | 98.79 | 95.57 | 95.08 | 94.84 |
| Number of ions on the basis of twenty-four oxygens | | | | | | | | | |
| Si | 8.512 | 8.532 | 8.531 | 8.499 | 8.417 | 8.514 | 9.190 | 8.400 | 8.865 |
| Ti | 0.061 | 0.064 | 0.057 | 0.072 | 0.060 | 0.044 | 0.038 | 0.055 | 0.031 |
| Al | 3.084 | 3.080 | 3.087 | 3.072 | 2.972 | 3.010 | 2.218 | 2.713 | 1.708 |
| Cr | 0.004 | 0.002 | 0.004 | 0.000 | 0.002 | 0.000 | 0.001 | 0.000 | 0.000 |
| Fe | 0.491 | 0.512 | 0.504 | 0.549 | 0.769 | 0.587 | 0.886 | 1.503 | 2.120 |
| Mn | 0.025 | 0.013 | 0.005 | 0.000 | 0.007 | 0.014 | 0.010 | 0.021 | 0.021 |
| Mg | 0.344 | 0.318 | 0.323 | 0.321 | 0.446 | 0.357 | 0.228 | 0.600 | 0.669 |
| Ca | 0.646 | 0.639 | 0.635 | 0.546 | 0.684 | 0.786 | 0.329 | 0.979 | 0.355 |
| Na | 0.631 | 0.590 | 0.615 | 0.549 | 0.491 | 0.488 | 0.784 | 0.979 | 0.297 |
| K | 0.540 | 0.587 | 0.586 | 0.642 | 0.560 | 0.508 | 0.604 | 0.824 | 0.407 |
| P | 0.042 | 0.041 | 0.037 | 0.078 | 0.044 | 0.044 | 0.022 | 0.024 | 0.047 |
| Ni | 0.023 | 0.002 | 0.019 | 0.003 | 0.020 | 0.000 | 0.005 | 0.000 | 0.011 |
| Total | 14.404 | 14.387 | 14.411 | 14.496 | 14.342 | 14.369 | 14.315 | 15.053 | 14.531 |

Table 8. Chemical compositions of fine-grained crystalline matrix in type-IV pseudotachylite analyzed by EDX.

| | Matrix in microlitic pseudotachylite | | | | | | | | |
|---|---|---|---|---|---|---|---|---|---|
| Wt% | Mn1 | Mn2 | Mn3 | Mn4 | Mn5 | Mn6 | Mn7 | Mn8 | Mn9 |
| $SiO_2$ | 39.73 | 63.58 | 63.38 | 64.18 | 62.61 | 63.81 | 63.70 | 65.89 | 41.81 |
| $TiO_2$ | 1.69 | 0.73 | 0.80 | 0.87 | 1.05 | 0.81 | 0.79 | 0.54 | 1.08 |
| $Al_2O_3$ | 15.34 | 21.38 | 21.02 | 21.54 | 21.73 | 21.04 | 21.11 | 20.15 | 14.84 |
| FeO* | 15.55 | 0.77 | 1.17 | 0.67 | 0.85 | 0.62 | 0.90 | 1.24 | 15.78 |
| MnO | 0.19 | 0.05 | 0.00 | 0.00 | 0.12 | 0.00 | 0.00 | 0.09 | 0.26 |
| MgO | 12.24 | 0.00 | 0.00 | 0.01 | 0.00 | 0.00 | 0.18 | 0.16 | 12.44 |
| CaO | 1.20 | 2.48 | 2.34 | 2.47 | 2.56 | 2.31 | 2.46 | 2.37 | 3.74 |
| $Na_2O$ | 0.70 | 9.24 | 9.32 | 9.54 | 9.17 | 9.34 | 8.97 | 8.81 | 1.02 |
| $K_2O$ | 4.46 | 0.12 | 0.00 | 0.07 | 0.24 | 0.09 | 0.25 | 0.20 | 3.27 |
| $Cr_2O_3$ | 0.00 | 0.00 | 0.00 | 0.00 | 0.04 | 0.00 | 0.05 | 0.01 | 0.13 |
| NiO | 0.12 | 0.07 | 0.00 | 0.13 | 0.05 | 0.00 | 0.00 | 0.00 | 0.14 |
| $P_2O_5$ | 0.12 | 0.34 | 0.50 | 0.52 | 0.42 | 0.44 | 0.60 | 0.50 | 0.29 |
| Total | 91.34 | 98.76 | 98.53 | 100.00 | 98.84 | 98.46 | 99.01 | 99.96 | 94.80 |
| Number of ions on the basis of twenty-four oxygens | | | | | | | | | |
| Si | 6.545 | 8.514 | 8.508 | 8.487 | 8.406 | 8.547 | 8.499 | 8.696 | 6.628 |
| Ti | 0.209 | 0.075 | 0.081 | 0.087 | 0.105 | 0.081 | 0.078 | 0.054 | 0.128 |
| Al | 2.979 | 3.375 | 3.327 | 3.357 | 3.438 | 3.321 | 3.321 | 3.134 | 2.772 |
| Fe | 2.143 | 0.087 | 0.132 | 0.075 | 0.096 | 0.069 | 0.099 | 0.136 | 2.093 |
| Mn | 0.025 | 0.006 | 0.000 | 0.000 | 0.012 | 0.000 | 0.000 | 0.030 | 0.035 |
| Mg | 3.004 | 0.000 | 0.000 | 0.003 | 0.000 | 0.000 | 0.036 | 0.032 | 2.940 |
| Ca | 0.212 | 0.357 | 0.336 | 0.348 | 0.369 | 0.330 | 0.351 | 1.005 | 0.636 |
| Na | 0.224 | 2.400 | 2.427 | 2.445 | 2.367 | 2.439 | 2.322 | 2.253 | 0.313 |
| K | 0.938 | 0.021 | 0.000 | 0.012 | 0.039 | 0.015 | 0.042 | 0.034 | 0.662 |
| Cr | 0.000 | 0.000 | 0.000 | 0.000 | 0.006 | 0.000 | 0.006 | 0.001 | 0.016 |
| Ni | 0.015 | 0.009 | 0.000 | 0.012 | 0.006 | 0.000 | 0.000 | 0.000 | 0.018 |
| P | 0.016 | 0.039 | 0.057 | 0.057 | 0.048 | 0.051 | 0.081 | 0.168 | 0.038 |
| Total | 16.310 | 14.888 | 14.868 | 14.883 | 14.892 | 14.853 | 14.835 | 15.543 | |

Table 9. Chemical compositions of anorthoclase microlites analyzed by EDX.

| | Anorthoclase microlites | | | | | | | | |
|---|---|---|---|---|---|---|---|---|---|
| Wt% | Anor1 | Anor2 | Anor3 | Anor4 | Anor5 | Anor6 | Anor7 | Anor8 | Ano9 |
| $SiO_2$ | 62.59 | 63.62 | 61.95 | 64.27 | 62.85 | 62.59 | 63.23 | 65.57 | 66.0 |
| $TiO_2$ | 0.65 | 0.59 | 0.68 | 0.55 | 0.69 | 0.65 | 0.67 | 0.59 | 0.75 |
| $Al_2O_3$ | 19.68 | 20.28 | 19.70 | 19.74 | 19.89 | 20.02 | 21.39 | 20.69 | 19.45 |
| $Cr_2O_3$ | 0.00 | 0.00 | 0.05 | 0.06 | 0.03 | 0.09 | 0.00 | 0.05 | 0.05 |
| FeO* | 3.82 | 1.91 | 4.34 | 2.51 | 2.39 | 2.78 | 1.92 | 1.85 | 4.87 |
| MnO | 0.16 | 0.13 | 0.00 | 0.20 | 0.08 | 0.02 | 0.07 | 0.00 | 0.27 |
| MgO | 1.25 | 0.50 | 1.87 | 0.64 | 0.42 | 0.91 | 0.42 | 0.04 | 1.60 |
| CaO | 3.21 | 3.34 | 2.87 | 2.99 | 3.18 | 3.15 | 3.13 | 3.41 | 3.17 |
| $Na_2O$ | 5.83 | 6.53 | 6.10 | 6.44 | 6.25 | 6.70 | 6.17 | 6.51 | 5.96 |
| $K_2O$ | 2.69 | 2.56 | 3.04 | 2.62 | 2.26 | 2.59 | 3.61 | 2.41 | 2.68 |
| Total | 99.74 | 99.46 | 100.50 | 99.93 | 98.09 | 99.19 | 100.52 | 100.92 | 99.40 |
| Number of ions on the basis of eight oxygens | | | | | | | | | |
| Si | 2.822 | 2.846 | 2.790 | 2.863 | 2.862 | 2.819 | 2.836 | 2.874 | 2.783 |
| Ti | 0.022 | 0.020 | 0.023 | 0.018 | 0.023 | 0.022 | 0.022 | 0.019 | 0.026 |
| Al | 1.046 | 1.069 | 1.046 | 1.036 | 1.067 | 1.063 | 1.096 | 1.069 | 1.021 |
| Cr | 0.000 | 0.000 | 0.002 | 0.002 | 0.001 | 0.003 | 0.000 | 0.002 | 0.002 |
| Fe | 0.144 | 0.071 | 0.167 | 0.094 | 0.091 | 0.104 | 0.070 | 0.068 | 0.187 |
| Mn | 0.006 | 0.005 | 0.000 | 0.008 | 0.003 | 0.001 | 0.003 | 0.000 | 0.011 |
| Mg | 0.084 | 0.033 | 0.113 | 0.042 | 0.029 | 0.061 | 0.028 | 0.003 | 0.110 |
| Ca | 0.155 | 0.160 | 0.138 | 0.143 | 0.155 | 0.152 | 0.146 | 0.160 | 0.156 |
| Na | 0.510 | 0.533 | 0.533 | 0.556 | 0.552 | 0.585 | 0.520 | 0.554 | 0.530 |
| K | 0.155 | 0.146 | 0.448 | 0.149 | 0.133 | 0.149 | 0.200 | 0.138 | 0.157 |
| An:Ab:Or radios | | | | | | | | | |
| An | 18.90 | 18.35 | 16.35 | 16.85 | 18.49 | 17.12 | 16.83 | 18.88 | 18.49 |
| Ab | 62.20 | 64.91 | 62.96 | 65.55 | 65.67 | 66.06 | 60.07 | 65.21 | 62.86 |
| Or | 18.90 | 16.74 | 20.69 | 17.60 | 15.84 | 16.82 | 23.10 | 15.91 | 18.65 |

Table 10. Chemical compositons of alkali feldspar microlites analyzed by EDX.

| | Alkali felspars in spherulitic microlites | | | | | | | | |
|---|---|---|---|---|---|---|---|---|---|
| Wt% | Alkf1 | Alkf2 | Alkf3 | Alkf4 | Alkf5 | Alkf6 | Alkf7 | Alkf8 | Alkf9 |
| $SiO_2$ | 65.09 | 66.73 | 66.70 | 65.39 | 66.19 | 65.17 | 62.55 | 63.39 | 62.96 |
| $TiO_2$ | 0.07 | 0.12 | 0.16 | 0.16 | 0.09 | 0.11 | 0.94 | 0.26 | 0.17 |
| $Al_2O_3$ | 18.99 | 19.49 | 19.35 | 19.23 | 19.42 | 19.19 | 18.89 | 18.54 | 18.39 |
| $Cr_2O_3$ | 0.00 | 0.00 | 0.00 | 0.00 | 0.00 | 0.00 | 0.02 | 0.01 | 0.04 |
| FeO* | 0.00 | 0.00 | 0.00 | 0.00 | 0.03 | 0.33 | 1.55 | 0.00 | 0.06 |
| MnO | 0.03 | 0.04 | 0.15 | 0.00 | 0.02 | 0.02 | 0.03 | 0.00 | 0.00 |
| MgO | 0.00 | 0.00 | 0.01 | 0.06 | 0.00 | 0.06 | 0.53 | 0.00 | 0.00 |
| CaO | 0.00 | 0.12 | 0.23 | 0.00 | 0.34 | 0.50 | 0.98 | 0.00 | 0.00 |
| $Na_2O$ | 2.62 | 5.01 | 4.76 | 0.05 | 4.58 | 4.53 | 1.72 | 1.32 | 0.73 |
| $K_2O$ | 11.83 | 5.80 | 5.65 | 16.48 | 5.59 | 5.41 | 12.21 | 14.11 | 14.66 |
| Total | 98.83 | 97.31 | 97.01 | 101.48 | 96.26 | 95.32 | 99.41 | 97.53 | 97.01 |
| Number of ions on the basis of eight oxygens | | | | | | | | | |
| Si | 2.972 | 3.009 | 3.015 | 2.957 | 3.019 | 3.000 | 2.866 | 2.963 | 2.964 |
| Ti | 0.002 | 0.004 | 0.006 | 0.005 | 0.003 | 0.004 | 0.033 | 0.009 | 0.006 |
| Al | 1.022 | 1.006 | 1.027 | 1.025 | 1.044 | 1.031 | 1.027 | 1.021 | 1.016 |
| Cr | 0.000 | 0.000 | 0.000 | 0.000 | 0.000 | 0.000 | 0.001 | 0.000 | 0.001 |
| Fe | 0.000 | 0.000 | 0.000 | 0.000 | 0.001 | 0.013 | 0.020 | 0.000 | 0.002 |
| Mn | 0.001 | 0.001 | 0.006 | 0.000 | 0.001 | 0.001 | 0.001 | 0.000 | 0.000 |
| Mg | 0.000 | 0.000 | 0.001 | 0.004 | 0.000 | 0.004 | 0.012 | 0.000 | 0.000 |
| Ca | 0.000 | 0.006 | 0.006 | 0.000 | 0.015 | 0.025 | 0.049 | 0.000 | 0.000 |
| Na | 0.232 | 0.438 | 0.417 | 0.005 | 0.405 | 0.404 | 0.154 | 0.120 | 0.067 |
| K | 0.689 | 0.334 | 0.326 | 0.951 | 0.325 | 0.318 | 0.719 | 0.843 | 0.880 |
| An:Ab:Or radios | | | | | | | | | |
| An | 0.000 | 7.61 | 0.81 | 0.00 | 2.02 | 3.35 | 0.05 | 0.00 | 0.00 |
| Ab | 25.19 | 56.44 | 55.67 | 0.52 | 54.51 | 54.08 | 16.70 | 12.46 | 7.08 |
| Or | 74.81 | 35.95 | 43.52 | 99.48 | 43.47 | 42.57 | 83.25 | 87.54 | 92.92 |

Table 11. Chemical compositions of alkali feldspar microlites analyzed by EDX.

| | Alkali felspars in dendritic microlites | | | | | | | | |
|---|---|---|---|---|---|---|---|---|---|
| Wt% | Alkd1 | Alkd2 | Alkd3 | Alkd4 | Alkd5 | Alkd6 | Alkd7 | Alkd8 | Alkd9 |
| $SiO_2$ | 60.54 | 60.85 | 59.63 | 60.45 | 62.84 | 63.60 | 66.25 | 66.68 | 66.38 |
| $TiO_2$ | 0.26 | 0.19 | 0.15 | 0.37 | 0.16 | 0.25 | 0.35 | 0.35 | 0.33 |
| $Al_2O_3$ | 19.29 | 18.70 | 19.92 | 19.67 | 18.75 | 17.45 | 17.10 | 17.11 | 18.79 |
| $Cr_2O_3$ | 0.19 | 0.19 | 0.04 | 0.00 | 0.00 | 0.04 | 0.01 | 0.00 | 0.00 |
| FeO* | 1.53 | 0.93 | 1.50 | 1.32 | 0.72 | 1.72 | 1.41 | 0.48 | 0.77 |
| MnO | 0.15 | 0.22 | 0.06 | 0.15 | 0.00 | 0.12 | 0.01 | 0.11 | 0.00 |
| MgO | 0.22 | 0.14 | 0.39 | 0.37 | 0.12 | 0.80 | 0.56 | 0.19 | 0.34 |
| CaO | 0.89 | 0.91 | 0.78 | 0.49 | 0.93 | 1.21 | 1.18 | 1.49 | 1.18 |
| $Na_2O$ | 1.35 | 1.53 | 1.47 | 0.92 | 0.96 | 3.76 | 4.92 | 1.94 | 2.21 |
| $K_2O$ | 15.22 | 14.74 | 12.18 | 14.28 | 11.43 | 7.44 | 5.44 | 10.96 | 9.02 |
| Total | 99.65 | 98.34 | 96.06 | 97.02 | 95.53 | 96.39 | 97.22 | 96.22 | 96.14 |
| Number of ions on the basis of eight oxygens | | | | | | | | | |
| Si | 2.854 | 2.887 | 2.864 | 2.895 | 2.973 | 2.995 | 3.031 | 3.007 | 3.026 |
| Ti | 0.009 | 0.004 | 0.005 | 0.013 | 0.006 | 0.029 | 0.012 | 0.012 | 0.012 |
| Al | 1.072 | 1.045 | 1.116 | 1.054 | 1.013 | 0.928 | 0.922 | 0.952 | 0.874 |
| Cr | 0.007 | 0.007 | 0.001 | 0.000 | 0.000 | 0.001 | 0.001 | 0.000 | 0.000 |
| Fe | 0.060 | 0.033 | 0.060 | 0.053 | 0.029 | 0.065 | 0.054 | 0.014 | 0.030 |
| Mn | 0.006 | 0.009 | 0.002 | 0.006 | 0.000 | 0.005 | 0.001 | 0.001 | 0.000 |
| Mg | 0.015 | 0.010 | 0.028 | 0.027 | 0.008 | 0.058 | 0.034 | 0.014 | 0.010 |
| Ca | 0.045 | 0.046 | 0.136 | 0.025 | 0.044 | 0.062 | 0.058 | 0.002 | 0.059 |
| Na | 0.123 | 0.140 | 0.136 | 0.086 | 0.088 | 0.349 | 0.436 | 0.144 | 0.166 |
| K | 0.916 | 0.892 | 0.755 | 0.872 | 0.691 | 0.454 | 0.317 | 0.660 | 0.536 |
| An:Ab:Or radios | | | | | | | | | |
| An | 4.16 | 4.30 | 4.03 | 2.58 | 5.73 | 7.17 | 7.14 | 8.28 | 7.42 |
| Ab | 11.37 | 13.03 | 14.82 | 8.72 | 10.65 | 40.32 | 53.76 | 19.42 | 25.12 |
| Or | 84.47 | 82.67 | 81.15 | 88.71 | 83.62 | 52.51 | 39.10 | 72.30 | 67.46 |

Table 12. Chemical compositions of plagioclase microlites analyzed by EDX.

| | Labradorites in dendritic microlites | | | | | | | | |
|---|---|---|---|---|---|---|---|---|---|
| Wt% | Lab1 | Lab2 | Lab3 | Lab4 | Lab5 | Lab6 | Lab7 | Lab8 | Lab9 |
| $SiO_2$ | 51.88 | 50.42 | 50.46 | 50.99 | 51.38 | 52.49 | 53.34 | 50.24 | 50.33 |
| $TiO_2$ | 0.43 | 0.25 | 0.32 | 0.44 | 0.38 | 0.39 | 0.17 | 0.50 | 0.23 |
| $Al_2O_3$ | 29.43 | 31.01 | 30.10 | 30.28 | 28.54 | 27.96 | 26.82 | 29.03 | 28.23 |
| $Cr_2O_3$ | 0.06 | 0.05 | 0.06 | 0.10 | 0.12 | 0.10 | 0.11 | 0.11 | 0.20 |
| FeO* | 0.99 | 0.98 | 1.10 | 0.91 | 0.99 | 0.84 | 0.91 | 1.04 | 1.02 |
| MnO | 0.00 | 0.08 | 0.00 | 0.01 | 0.00 | 0.00 | 0.16 | 0.15 | 0.21 |
| MgO | 0.16 | 0.18 | 0.07 | 0.16 | 0.21 | 0.12 | 0.19 | 0.23 | 0.17 |
| CaO | 11.67 | 13.01 | 12.25 | 12.44 | 10.83 | 10.27 | 10.96 | 12.91 | 12.57 |
| $Na_2O$ | 3.92 | 3.30 | 3.23 | 3.66 | 4.13 | 4.41 | 3.85 | 3.26 | 3.59 |
| $K_2O$ | 0.45 | 0.37 | 0.42 | 0.38 | 0.50 | 0.58 | 1.63 | 0.47 | 0.48 |
| Total | 99.00 | 99.65 | 98.27 | 99.37 | 97.11 | 97.16 | 98.19 | 97.95 | 97.05 |
| Number of ions on the basis of eight oxygens | | | | | | | | | |
| Si | 2.384 | 2.305 | 2.327 | 2.332 | 2.397 | 2.445 | 2.466 | 2.333 | 2.334 |
| Ti | 0.015 | 0.009 | 0.011 | 0.015 | 0.013 | 0.014 | 0.006 | 0.018 | 0.008 |
| Al | 1.594 | 1.671 | 1.644 | 1.632 | 1.569 | 1.534 | 1.473 | 1.601 | 1.574 |
| Cr | 0.002 | 0.002 | 0.002 | 0.004 | 0.001 | 0.004 | 0.004 | 0.004 | 0.007 |
| Fe | 0.034 | 0.034 | 0.043 | 0.035 | 0.034 | 0.033 | 0.035 | 0.041 | 0.040 |
| Mn | 0.000 | 0.003 | 0.000 | 0.001 | 0.000 | 0.000 | 0.006 | 0.006 | 0.008 |
| Mg | 0.006 | 0.013 | 0.005 | 0.011 | 0.015 | 0.007 | 0.013 | 0.016 | 0.012 |
| Ca | 0.565 | 0.673 | 0.622 | 0.609 | 0.542 | 0.513 | 0.514 | 0.647 | 0.636 |
| Na | 0.349 | 0.293 | 0.290 | 0.325 | 0.373 | 0.366 | 0.318 | 0.296 | 0.329 |
| K | 0.026 | 0.021 | 0.025 | 0.022 | 0.030 | 0.034 | 0.097 | 0.096 | 0.029 |
| An:Ab:Or radios | | | | | | | | | |
| An | 60.07 | 66.97 | 66.15 | 63.75 | 57.32 | 54.23 | 55.14 | 66.67 | 64.04 |
| Ab | 37.16 | 30.79 | 30.97 | 33.95 | 39.51 | 42.15 | 35.04 | 30.48 | 33.08 |
| Or | 2.77 | 2.24 | 2.88 | 2.30 | 3.17 | 3.62 | 9.72 | 2.85 | 2.88 |

Table 13. Chemical compositions of plagioclase microlites analyzed by EDX.

| | Labradorite | | | Betonite | Andesine | | | | |
|---|---|---|---|---|---|---|---|---|---|
| Wt% | Lab10 | Lab11 | Lab12 | Bet1 | And1 | And2 | And3 | And4 | And5 |
| $SiO_2$ | 53.91 | 51.03 | 51.27 | 50.38 | 60.99 | 60.71 | 60.11 | 56.78 | 57.78 |
| $TiO_2$ | 0.25 | 0.25 | 0.16 | 0.40 | 0.40 | 0.66 | 0.09 | 0.30 | 0.24 |
| $Al_2O_3$ | 27.12 | 26.15 | 27.86 | 29.02 | 22.36 | 18.59 | 24.70 | 24.39 | 24.74 |
| $Cr_2O_3$ | 0.11 | 0.15 | 0.09 | 0.11 | 0.06 | 0.04 | 0.05 | 0.15 | 0.17 |
| FeO* | 1.15 | 0.99 | 0.99 | 1.04 | 1.78 | 3.93 | 0.48 | 0.40 | 0.53 |
| MnO | 0.18 | 0.12 | 0.12 | 0.20 | 0.08 | 0.18 | 0.00 | 0.08 | 0.06 |
| MgO | 0.21 | 0.11 | 0.20 | 0.18 | 0.53 | 0.83 | 0.00 | 0.08 | 0.06 |
| CaO | 10.91 | 12.23 | 10.97 | 13.43 | 6.01 | 4.74 | 6.00 | 6.90 | 7.06 |
| $Na_2O$ | 4.41 | 3.74 | 4.28 | 2.84 | 6.60 | 6.34 | 7.30 | 5.65 | 5.54 |
| $K_2O$ | 0.74 | 0.44 | 0.46 | 0.58 | 0.32 | 0.50 | 0.34 | 1.72 | 0.99 |
| Total | 98.98 | 97.21 | 96.97 | 97.18 | 99.11 | 96.52 | 99.09 | 96.51 | 97.36 |
| Number of ions on the basis of eight oxygens | | | | | | | | | |
| Si | 2.464 | 2.345 | 2.437 | 2.315 | 2.722 | 2.789 | 2.693 | 2.973 | 2.981 |
| Ti | 0.008 | 0.008 | 0.006 | 0.014 | 0.014 | 0.023 | 0.003 | 0.010 | 0.008 |
| Al | 1.437 | 1.561 | 1.505 | 1.617 | 1.509 | 1.036 | 1.307 | 1.340 | 1.342 |
| Cr | 0.004 | 0.005 | 0.007 | 0.004 | 0.002 | 0.001 | 0.002 | 0.005 | 0.006 |
| Fe | 0.044 | 0.039 | 0.039 | 0.041 | 0.066 | 0.156 | 0.018 | 0.016 | 0.020 |
| Mn | 0.021 | 0.014 | 0.014 | 0.024 | 0.009 | 0.021 | 0.000 | 0.016 | 0.020 |
| Mg | 0.014 | 0.007 | 0.014 | 0.013 | 0.035 | 0.059 | 0.000 | 0.005 | 0.034 |
| Ca | 0.538 | 0.617 | 0.559 | 0.680 | 0.287 | 0.243 | 0.288 | 0.345 | 0.348 |
| Na | 0.397 | 0.341 | 0.395 | 0.294 | 0.571 | 0.581 | 0.635 | 0.511 | 0.494 |
| K | 0.044 | 0.026 | 0.026 | 0.026 | 0.018 | 0.027 | 0.019 | 0.102 | 0.058 |
| An:Ab:Or radios | | | | | | | | | |
| An | 55.16 | 62.65 | 56.94 | 69.73 | 32.78 | 29.35 | 30.59 | 37.32 | 38.65 |
| Ab | 40.37 | 34.64 | 40.24 | 26.68 | 65.13 | 68.25 | 67.33 | 53.85 | 54.87 |
| Or | 4.47 | 2.71 | 2.82 | 3.59 | 4.09 | 2.40 | 2.08 | 8.83 | 6.48 |

Table 14. Chemical compositons of plagiocalse microlites analyzed by EDX.

| | Oligoclase microlites | | | | | | | | |
|---|---|---|---|---|---|---|---|---|---|
| Wt% | Olig1 | Olig2 | Olig3 | Olig4 | Olig5 | Olig6 | Olig7 | Olig8 | Olig9 |
| $SiO_2$ | 60.79 | 60.48 | 61.33 | 60.91 | 60.54 | 63.73 | 63.79 | 60.54 | 60.60 |
| $TiO_2$ | 0.06 | 0.05 | 0.18 | 0.13 | 0.66 | 0.52 | 0.65 | 0.19 | 0.65 |
| $Al_2O_3$ | 24.65 | 24.47 | 24.10 | 24.51 | 19.33 | 19.66 | 19.66 | 23.87 | 19.79 |
| $Cr_2O_3$ | 0.03 | 0.00 | 0.03 | 0.03 | 0.06 | 0.04 | 0.04 | 0.05 | 0.00 |
| FeO* | 0.44 | 0.55 | 0.38 | 0.38 | 4.80 | 4.01 | 3.63 | 1.33 | 4.60 |
| MnO | 0.04 | 0.06 | 0.00 | 0.00 | 0.13 | 0.02 | 0.10 | 0.24 | 0.18 |
| MgO | 0.05 | 0.07 | 0.00 | 0.00 | 0.13 | 0.02 | 0.10 | 0.24 | 0.18 |
| CaO | 5.46 | 5.43 | 4.72 | 5.22 | 4.53 | 3.07 | 3.09 | 4.91 | 4.59 |
| $Na_2O$ | 7.72 | 7.74 | 7.89 | 7.66 | 6.68 | 7.03 | 7.28 | 7.21 | 6.45 |
| $K_2O$ | 0.31 | 0.15 | 0.44 | 0.33 | 1.03 | 1.02 | 1.11 | 1.51 | 0.75 |
| Total | 99.54 | 99.00 | 99.07 | 99.32 | 99.12 | 100.51 | 100.70 | 100.54 | 99.02 |
| Number of ions on the basis of eight oxygens | | | | | | | | | |
| Si | 2.699 | 2.703 | 2.734 | 2.708 | 2.761 | 2.825 | 2.833 | 2.700 | 2.746 |
| Ti | 0.002 | 0.002 | 0.006 | 0.004 | 0.022 | 0.017 | 0.022 | 0.006 | 0.022 |
| Al | 1.290 | 1.293 | 0.267 | 1.284 | 1.037 | 1.027 | 1.029 | 1.255 | 1.060 |
| Cr | 0.001 | 0.000 | 0.001 | 0.001 | 0.002 | 0.001 | 0.002 | 0.001 | 0.000 |
| Fe | 0.016 | 0.021 | 0.014 | 0.014 | 0.184 | 0.148 | 0.135 | 0.049 | 0.007 |
| Mn | 0.001 | 0.002 | 0.000 | 0.000 | 0.005 | 0.001 | 0.004 | 0.009 | 0.007 |
| Mg | 0.003 | 0.004 | 0.000 | 0.003 | 0.085 | 0.106 | 0.089 | 0.046 | 0.099 |
| Ca | 0.259 | 0.261 | 0.226 | 0.249 | 0.225 | 0.146 | 0.147 | 0.235 | 0.224 |
| Na | 0.665 | 0.673 | 0.682 | 0.660 | 0.593 | 0.604 | 0.627 | 0.623 | 0.571 |
| K | 0.018 | 0.008 | 0.025 | 0.018 | 0.059 | 0.058 | 0.063 | 0.084 | 0.044 |
| An:Ab:Or radios | | | | | | | | | |
| An | 27.56 | 27.11 | 24.19 | 26.84 | 25.77 | 18.14 | 17.56 | 24.86 | 26.94 |
| Ab | 70.53 | 71.41 | 73.13 | 71.20 | 67.78 | 74.72 | 74.92 | 66.03 | 68.02 |
| Or | 1.91 | 1.48 | 2.68 | 1.96 | 6.45 | 7.14 | 7.52 | 9.11 | 5.04 |

Table 15. Chemical compositions of plagioclase microlites analyzed by EDX.

| | Plagioclase in spherulitic microlites | | | | | | | | |
|---|---|---|---|---|---|---|---|---|---|
| Wt% | Plas1 | Plas2 | Plas3 | Plas4 | Plas5 | Plas6 | Plas7 | Plas8 | Plas9 |
| $SiO_2$ | 58.95 | 57.27 | 55.01 | 56.73 | 54.26 | 61.00 | 66.77 | 53.34 | 68.43 |
| $TiO_2$ | 0.04 | 0.05 | 0.08 | 0.12 | 0.04 | 0.00 | 0.62 | 0.15 | 0.60 |
| $Al_2O_3$ | 26.52 | 25.80 | 27.99 | 26.48 | 27.95 | 24.89 | 18.95 | 27.99 | 18.03 |
| $Cr_2O_3$ | 0.04 | 0.10 | 0.00 | 0.00 | 0.00 | 0.14 | 0.04 | 0.13 | 0.00 |
| FeO* | 0.70 | 1.12 | 1.53 | 0.69 | 1.13 | 0.33 | 1.27 | 1.30 | 1.32 |
| MnO | 0.00 | 0.00 | 0.00 | 0.13 | 0.01 | 0.00 | 0.03 | 0.11 | 0.04 |
| MgO | 0.00 | 0.02 | 0.45 | 0.00 | 0.00 | 0.00 | 0.03 | 0.01 | 0.43 |
| CaO | 7.58 | 8.20 | 9.54 | 8.41 | 10.13 | 5.97 | 5.58 | 10.57 | 5.57 |
| $Na_2O$ | 6.57 | 5.86 | 5.02 | 5.63 | 4.84 | 7.24 | 5.03 | 4.54 | 4.02 |
| $K_2O$ | 0.54 | 0.44 | 0.56 | 0.60 | 0.30 | 0.33 | 0.51 | 0.47 | 0.59 |
| Total | 100.94 | 98.86 | 100.18 | 98.79 | 98.66 | 99.90 | 98.80 | 98.61 | 99.03 |
| Number of ions on the basis of eight oxygens | | | | | | | | | |
| Si | 2.606 | 2.591 | 2.482 | 2.577 | 2.484 | 2.704 | 2.934 | 2.444 | 2.994 |
| Ti | 0.001 | 0.002 | 0.003 | 0.004 | 0.001 | 0.000 | 0.021 | 0.005 | 0.020 |
| Al | 1.382 | 1.376 | 1.489 | 1.418 | 1.508 | 1.300 | 0.982 | 1.512 | 0.930 |
| Cr | 0.001 | 0.003 | 0.000 | 0.000 | 0.000 | 0.005 | 0.001 | 0.005 | 0.000 |
| Fe | 0.026 | 0.042 | 0.058 | 0.026 | 0.043 | 0.012 | 0.047 | 0.050 | 0.048 |
| Mn | 0.000 | 0.000 | 0.000 | 0.005 | 0.000 | 0.000 | 0.001 | 0.004 | 0.002 |
| Mg | 0.000 | 0.001 | 0.030 | 0.000 | 0.000 | 0.000 | 0.030 | 0.001 | 0.028 |
| Ca | 0.359 | 0.397 | 0.461 | 0.392 | 0.497 | 0.284 | 0.263 | 0.519 | 0.261 |
| Na | 0.564 | 0.514 | 0.440 | 0.496 | 0.429 | 0.625 | 0.429 | 0.404 | 0.341 |
| K | 0.031 | 0.025 | 0.032 | 0.035 | 0.018 | 0.019 | 0.029 | 0.027 | 0.033 |
| An:Ab:Or radios | | | | | | | | | |
| An | 37.63 | 41.97 | 49.41 | 42.47 | 53.21 | 30.60 | 28.56 | 54.63 | 41.10 |
| Ab | 59.12 | 54.33 | 47.16 | 53.74 | 45.93 | 67.34 | 45.60 | 42.53 | 53.70 |
| Or | 3.25 | 3.70 | 3.43 | 3.79 | 0.86 | 2.06 | 5.84 | 2.84 | 5.20 |

Table 16. Chemical compositions of plagioclase fragments analyzed by EDX.

| | Fragments of alkali feldspar | | | | | | | | |
|---|---|---|---|---|---|---|---|---|---|
| Wt% | Frag1 | Frag2 | Frag3 | Frag4 | Frag5 | Frag6 | Frag7 | Frag8 | Frag9 |
| $SiO_2$ | 62.83 | 58.05 | 60.96 | 58.76 | 64.43 | 64.13 | 64.34 | 64.68 | 64.92 |
| $TiO_2$ | 0.21 | 0.61 | 0.33 | 0.29 | 0.16 | 0.24 | 0.12 | 0.20 | 0.16 |
| $Al_2O_3$ | 17.67 | 20.49 | 17.64 | 22.09 | 18.72 | 18.95 | 18.75 | 19.09 | 19.05 |
| Cr2O3 | 0.08 | 0.21 | 0.12 | 0.02 | 0.04 | 0.00 | 0.00 | 0.00 | 0.00 |
| FeO* | 1.03 | 0.90 | 1.54 | 1.24 | 0.07 | 0.00 | 0.00 | 0.02 | 0.00 |
| MnO | 0.17 | 0.05 | 0.09 | 0.06 | 0.00 | 0.04 | 0.06 | 0.08 | 0.00 |
| MgO | 0.32 | 0.36 | 0.35 | 0.51 | 0.00 | 0.00 | 0.00 | 0.00 | 0.12 |
| CaO | 0.28 | 0.25 | 0.60 | 0.02 | 0.00 | 0.00 | 0.00 | 0.00 | 0.00 |
| $Na_2O$ | 0.37 | 0.17 | 0.71 | 0.39 | 0.81 | 0.94 | 1.17 | 0.44 | 0.12 |
| $K_2O$ | 18.26 | 16.29 | 14.87 | 12.87 | 14.85 | 14.80 | 14.16 | 15.53 | 16.27 |
| Total | 101.20 | 97.48 | 97.21 | 96.24 | 99.08 | 99.40 | 98.60 | 100.04 | 100.64 |
| Number of ions on the basis of eight oxygens | | | | | | | | | |
| Si | 2.930 | 2.792 | 2.924 | 2.783 | 2.965 | 2.954 | 2.968 | 2.954 | 2.965 |
| Ti | 0.007 | 0.022 | 0.012 | 0.010 | 0.006 | 0.008 | 0.004 | 0.007 | 0.006 |
| Al | 0.971 | 1.164 | 1.001 | 1.244 | 1.015 | 1.029 | 1.019 | 1.028 | 1.026 |
| Cr | 0.003 | 0.008 | 0.004 | 0.001 | 0.002 | 0.000 | 0.000 | 0.000 | 0.000 |
| Fe | 0.040 | 0.036 | 0.058 | 0.049 | 0.003 | 0.000 | 0.000 | 0.001 | 0.000 |
| Mn | 0.007 | 0.002 | 0.004 | 0.002 | 0.000 | 0.002 | 0.002 | 0.003 | 0.000 |
| Mg | 0.022 | 0.026 | 0.025 | 0.037 | 0.000 | 0.000 | 0.000 | 0.000 | 0.025 |
| Ca | 0.014 | 0.013 | 0.031 | 0.001 | 0.000 | 0.000 | 0.000 | 0.000 | 0.000 |
| Na | 0.033 | 0.015 | 0.066 | 0.036 | 0.072 | 0.084 | 0.105 | 0.039 | 0.032 |
| K | 1.086 | 1.002 | 0.907 | 0.784 | 0.872 | 0.870 | 0.834 | 0.905 | 0.948 |
| An:Ab:Or radios | | | | | | | | | |
| An | 1.24 | 1.27 | 3.09 | 0.12 | 0.00 | 0.00 | 0.00 | 0.00 | 0.00 |
| Ab | 2.91 | 1.48 | 6.54 | 4.42 | 7.63 | 8.80 | 11.18 | 4.13 | 3.27 |
| Or | 95.85 | 97.25 | 90.37 | 95.46 | 92.37 | 91.20 | 88.82 | 95.87 | 96.73 |

Table 17. Chemical compositions of plagioclase fragments annlyzed by EDX.

| | Fragments of plagioclase | | | | | | | | |
|---|---|---|---|---|---|---|---|---|---|
| Wt% | Frag10 | Frag11 | Frag12 | Frag13 | Frag14 | Frag15 | Frag16 | Frag17 | Frag18 |
| $SiO_2$ | 62.10 | 60.80 | 61.50 | 60.92 | 60.02 | 62.36 | 64.69 | 61.14 | 61.97 |
| $TiO_2$ | 0.04 | 0.16 | 0.05 | 0.11 | 0.09 | 0.18 | 0.13 | 0.29 | 0.19 |
| $Al_2O_3$ | 24.47 | 23.91 | 24.37 | 24.30 | 24.73 | 23.62 | 22.17 | 24.40 | 24.57 |
| $Cr_2O_3$ | 0.00 | 0.03 | 0.04 | 0.08 | 0.00 | 0.04 | 0.07 | 0.07 | 0.06 |
| FeO* | 0.02 | 0.89 | 0.12 | 0.58 | 0.51 | 0.45 | 0.32 | 0.73 | 0.48 |
| MnO | 0.03 | 0.00 | 0.02 | 0.00 | 0.05 | 0.00 | 0.01 | 0.10 | 0.05 |
| MgO | 0.06 | 0.28 | 0.00 | 0.18 | 0.08 | 0.00 | 0.00 | 0.00 | 0.08 |
| CaO | 4.92 | 4.80 | 5.06 | 4.86 | 5.58 | 4.35 | 4.12 | 5.08 | 5.82 |
| $Na_2O$ | 7.34 | 7.20 | 7.65 | 7.28 | 7.41 | 8.27 | 8.20 | 7.83 | 7.53 |
| $K_2O$ | 1.38 | 0.92 | 0.92 | 1.24 | 0.32 | 0.38 | 0.11 | 0.25 | 0.44 |
| Total | 100.26 | 99.69 | 99.73 | 99.55 | 99.79 | 99.83 | 99.82 | 99.89 | 101.19 |
| Number of ions on the basis of eirht oxygens | | | | | | | | | |
| Si | 2.738 | 2.719 | 2.722 | 2.711 | 2.682 | 2.762 | 2.838 | 2.713 | 2.688 |
| Ti | 0.001 | 0.005 | 0.002 | 0.004 | 0.003 | 0.006 | 0.004 | 0.010 | 0.006 |
| Al | 1.272 | 1.260 | 1.271 | 1.274 | 1.303 | 1.233 | 1.146 | 1.276 | 1.306 |
| Cr | 0.000 | 0.001 | 0.001 | 0.003 | 0.000 | 0.001 | 0.002 | 0.003 | 0.002 |
| Fe | 0.001 | 0.033 | 0.005 | 0.022 | 0.019 | 0.017 | 0.012 | 0.027 | 0.017 |
| Mn | 0.001 | 0.000 | 0.001 | 0.000 | 0.002 | 0.000 | 0.000 | 0.003 | 0.002 |
| Mg | 0.004 | 0.019 | 0.000 | 0.012 | 0.005 | 0.000 | 0.000 | 0.000 | 0.005 |
| Ca | 0.233 | 0.230 | 0.240 | 0.232 | 0.267 | 0.207 | 0.194 | 0.241 | 0.271 |
| Na | 0.627 | 0.624 | 0.657 | 0.629 | 0.642 | 0.711 | 0.698 | 0.674 | 0.633 |
| K | 0.078 | 0.053 | 0.052 | 0.070 | 0.018 | 0.022 | 0.006 | 0.014 | 0.024 |
| An:Ab:Or radios | | | | | | | | | |
| An | 24.84 | 25.33 | 25.29 | 24.92 | 28.80 | 22.02 | 21.60 | 25.94 | 29.20 |
| Ab | 66.84 | 68.72 | 69.23 | 67.56 | 69.26 | 75.64 | 77.73 | 72.55 | 68.21 |
| Or | 8.32 | 5.95 | 5.48 | 7.52 | 1.94 | 2.34 | 1.67 | 1.51 | 2.59 |

Table 18. Chemical compositions of biotite microlites analyzed.
--:undetermined.

| | Accicular biotite microlites | | | | | | | | |
|---|---|---|---|---|---|---|---|---|---|
| Wt% | Bio1 | Bio2 | Bio3 | Bio4 | Bio5 | Bio6 | Bio7 | Bio8 | Bio9 |
| $SiO_2$ | 35.43 | 37.80 | 34.87 | 35.58 | 35.53 | 36.67 | 37.20 | 37.90 | 36.99 |
| $TiO_2$ | 2.39 | 5.78 | 4.74 | 8.84 | 5.48 | 2.25 | 2.27 | 3.28 | 2.82 |
| $Al_2O_3$ | 14.90 | 15.04 | 16.38 | 14.35 | 15.67 | 17.43 | 16.28 | 16.61 | 17.65 |
| $Cr_2O_3$ | 0.08 | 0.00 | 0.07 | 0.08 | 0.04 | 0.00 | 0.00 | 0.02 | 0.02 |
| FeO* | 16.13 | 12.54 | 14.97 | 12.60 | 13.57 | 22.74 | 17.73 | 18.92 | 17.65 |
| MnO | 0.61 | 0.00 | 0.18 | 0.16 | 0.15 | 0.51 | 0.23 | 0.15 | 0.24 |
| MgO | 12.67 | 11.95 | 11.93 | 11.16 | 11.04 | 10.40 | 12.43 | 10.36 | 12.95 |
| CaO | 0.24 | 0.63 | 0.28 | 0.38 | 0.36 | 0.32 | 0.34 | 0.17 | 0.18 |
| $Na_2O$ | 0.52 | 0.66 | 0.68 | 1.01 | 0.68 | 0.60 | 0.34 | 0.92 | 0.58 |
| $K_2O$ | 10.67 | 7.63 | 7.93 | 7.74 | 7.35 | 7.91 | 8.55 | 8.26 | 8.57 |
| $P_2O_5$ | -- | -- | -- | -- | -- | 0.31 | 0.34 | 0.25 | 0.12 |
| Total | 93.62 | 92.63 | 92.13 | 92.10 | 94.87 | 99.24 | 95.71 | 96.84 | 96.35 |
| Number of ions on the basis of twenty-two oxygens | | | | | | | | | |
| Si | 5.507 | 5.683 | 5.396 | 5.434 | 5.352 | 5.401 | 5.555 | 5.618 | 4.133 |
| Ti | 0.275 | 0.653 | 0.600 | 1.016 | 0.624 | 0.250 | 0.251 | 0.366 | 0.237 |
| Al | 2.731 | 2.665 | 2.946 | 2.583 | 2.797 | 3.028 | 2.866 | 2.901 | 2.137 |
| Cr | 0.009 | 0.000 | 0.008 | 0.009 | 0.005 | 0.000 | 0.000 | 0.003 | 0.003 |
| Fe | 2.731 | 1.576 | 1.934 | 1.609 | 2.353 | 2.802 | 2.214 | 2.346 | 1.650 |
| Mn | 0.081 | 0.000 | 0.024 | 0.020 | 0.019 | 0.063 | 0.030 | 0.019 | 0.022 |
| Mg | 2.937 | 2.678 | 2.747 | 2.541 | 2.492 | 2.305 | 2.767 | 2.288 | 2.156 |
| Ca | 0.039 | 0.010 | 0.046 | 0.062 | 0.059 | 0.050 | 0.055 | 0.028 | 0.022 |
| Na | 0.155 | 0.191 | 0.202 | 0.299 | 0.200 | 0.173 | 0.096 | 0.264 | 0.127 |
| K | 2.117 | 1.462 | 1.564 | 1.507 | 1.421 | 1.488 | 1.628 | 1.562 | 1.221 |
| P | -- | -- | -- | -- | -- | 0.039 | 0.041 | 0.030 | 0.011 |
| XMg | 0.51 | 0.63 | 0.59 | 0.61 | 0.51 | 0.45 | 0.55 | 0.49 | 0.56 |

Table 19. Chemical compositions of biotite microlites analyzed by EDX.

| | Biotites in spherulitic microlites | | | | | | | | |
|---|---|---|---|---|---|---|---|---|---|
| Wt% | Bio10 | Bio11 | Bio12 | Bio13 | Bio14 | Bio15 | Bio16 | Bio17 | Bio18 |
| $SiO_2$ | 38.76 | 36.23 | 37.52 | 36.70 | 37.32 | 36.29 | 37.43 | 37.20 | 37.44 |
| $TiO_2$ | 6.90 | 4.74 | 4.28 | 4.44 | 4.15 | 4.18 | 7.27 | 2.27 | 2.42 |
| $Al_2O_3$ | 15.93 | 16.84 | 17.89 | 17.78 | 17.39 | 14.45 | 16.66 | 16.28 | 17.32 |
| $Cr_2O_3$ | 0.04 | 0.00 | 0.11 | 0.09 | 0.00 | 0.02 | 0.00 | 0.00 | 0.08 |
| FeO* | 11.62 | 13.75 | 15.30 | 14.40 | 13.65 | 14.45 | 11.35 | 17.73 | 21.00 |
| MnO | 0.17 | 0.29 | 0.20 | 0.24 | 0.08 | 0.19 | 0.26 | 0.23 | 0.33 |
| MgO | 14.13 | 12.84 | 11.38 | 13.22 | 13.93 | 13.25 | 14.11 | 12.43 | 8.01 |
| CaO | 0.76 | 0.87 | 0.23 | 0.16 | 0.10 | 0.36 | 0.23 | 0.34 | 0.00 |
| $Na_2O$ | 1.80 | 0.66 | 0.76 | 0.86 | 0.87 | 0.85 | 1.21 | 0.34 | 0.00 |
| $K_2O$ | 7.51 | 8.46 | 8.79 | 8.46 | 8.60 | 8.19 | 7.60 | 8.55 | 8.01 |
| $P_2O_5$ | 0.16 | 0.56 | 0.01 | 0.16 | 0.10 | 0.11 | 0.06 | 0.34 | 0.18 |
| Total | 97.65 | 95.23 | 96.46 | 96.54 | 96.17 | 95.10 | 96.17 | 95.97 | 95.28 |
| Number of ions on the basis of twenty-two oxygens | | | | | | | | | |
| Si | 5.515 | 5.368 | 5.512 | 5.367 | 5.453 | 5.395 | 5.403 | 5.555 | 5.584 |
| Ti | 0.738 | 0.528 | 0.473 | 0.488 | 0.456 | 0.468 | 0.790 | 0.256 | 0.028 |
| Al | 2.671 | 2.940 | 3.098 | 3.065 | 2.996 | 3.017 | 0.834 | 2.866 | 3.126 |
| Cr | 0.004 | 0.000 | 0.013 | 0.011 | 0.000 | 0.002 | 0.000 | 0.000 | 0.009 |
| Fe | 1.382 | 1.704 | 1.880 | 1.765 | 1.668 | 1.796 | 1.370 | 2.214 | 2.688 |
| Mn | 0.020 | 0.036 | 0.025 | 0.029 | 0.010 | 0.024 | 0.032 | 0.011 | 0.042 |
| Mg | 2.975 | 2.837 | 2.491 | 2.882 | 3.033 | 2.936 | 3.036 | 2.767 | 1.829 |
| Ca | 0.115 | 0.138 | 0.036 | 0.024 | 0.015 | 0.058 | 0.036 | 0.055 | 0.000 |
| Na | 0.497 | 0.191 | 0.216 | 0.244 | 0.245 | 0.245 | 0.340 | 0.096 | 0.000 |
| K | 1.362 | 1.600 | 0.648 | 1.578 | 1.603 | 1.553 | 1.400 | 1.628 | 1.846 |
| P | 0.019 | 0.071 | 0.001 | 0.022 | 0.012 | 0.014 | 0.006 | 0.043 | 0.024 |
| XMg | 0.68 | 0.62 | 0.59 | 0.62 | 0.61 | 0.62 | 0.68 | 0.55 | 0.40 |

Table 20. Chemical compositions of biotite fragments analyzed by EDX.

| | Fragments of biotite | | | | | | | | |
|---|---|---|---|---|---|---|---|---|---|
| Wt% | Bio19 | Bio20 | Bio21 | Bio22 | Bio23 | Bio24 | Bio25 | Bio26 | Bio27 |
| $SiO_2$ | 36.48 | 37.00 | 36.36 | 37.13 | 36.78 | 36.97 | 36.94 | 36.43 | 36.42 |
| $TiO_2$ | 2.42 | 2.32 | 2.26 | 2.25 | 2.35 | 2.49 | 2.40 | 2.49 | 2.40 |
| $Al_2O_3$ | 17.33 | 18.08 | 17.33 | 18.28 | 17.32 | 17.78 | 17.89 | 17.37 | 17.36 |
| $Cr_2O_3$ | 0.08 | 0.00 | 0.05 | 0.00 | 0.00 | 0.00 | 0.00 | 0.06 | 0.01 |
| FeO* | 21.01 | 21.19 | 20.96 | 20.93 | 21.48 | 21.44 | 21.12 | 20.87 | 20.73 |
| MnO | 0.32 | 0.50 | 0.30 | 0.45 | 0.04 | 0.36 | 0.30 | 0.38 | 0.27 |
| MgO | 8.01 | 8.44 | 7.83 | 8.30 | 8.15 | 8.32 | 8.01 | 7.68 | 8.35 |
| CaO | 0.00 | 0.00 | 0.06 | 0.00 | 0.03 | 0.02 | 0.00 | 0.00 | 0.02 |
| $Na_2O$ | 0.00 | 0.05 | 0.00 | 0.18 | 0.03 | 0.22 | 0.00 | 0.03 | 0.00 |
| $K_2O$ | 9.45 | 9.35 | 9.34 | 9.70 | 9.21 | 9.58 | 9.82 | 9.63 | 9.18 |
| $P_2O_5$ | 0.18 | 0.27 | 0.21 | 0.17 | 0.12 | 0.31 | 0.21 | 0.25 | 0.16 |
| Total | 95.28 | 97.20 | 94.73 | 97.39 | 95.81 | 97.26 | 96.67 | 95.17 | 95.00 |
| Number of ions on the basis of twenty-two oxygens | | | | | | | | | |
| Si | 5.854 | 5.545 | 5.600 | 5.543 | 5.601 | 5.531 | 5.573 | 5.578 | 5.588 |
| Ti | 0.278 | 0.262 | 0.262 | 0.253 | 0.269 | 0.278 | 0.272 | 0.287 | 0.277 |
| Al | 3.126 | 3.193 | 3.146 | 3.215 | 3.108 | 3.135 | 3.177 | 3.135 | 3.130 |
| Cr | 0.009 | 0.000 | 0.000 | 0.000 | 0.000 | 0.000 | 0.000 | 0.007 | 0.001 |
| Fe | 2.688 | 2.653 | 2.700 | 2.612 | 2.735 | 2.682 | 2.664 | 2.673 | 2.652 |
| Mn | 0.042 | 0.064 | 0.040 | 0.001 | 0.030 | 0.045 | 0.038 | 0.050 | 0.035 |
| Mg | 1.829 | 1.884 | 1.798 | 1.848 | 1.850 | 1.856 | 1.802 | 1.754 | 1.904 |
| Ca | 0.000 | 0.000 | 0.039 | 0.001 | 0.004 | 0.003 | 0.000 | 0.000 | 0.003 |
| Na | 0.000 | 0.015 | 0.000 | 0.053 | 0.009 | 0.064 | 0.000 | 0.008 | 0.000 |
| K | 1.846 | 1.787 | 1.798 | 1.847 | 1.829 | 1.802 | 1.754 | 1.904 | 1.792 |
| P | 0.024 | 0.035 | 0.019 | 0.021 | 0.015 | 0.043 | 0.027 | 0.032 | 0.021 |
| XMg | 0.40 | 0.42 | 0.40 | 0.41 | 0.40 | 0.41 | 0.40 | 0.40 | 0.42 |

Table 21. Chemical compositios of hornblende microlites analyzed by EDX.

| | Skeletal hornblende microlites | | | | | | | |
|---|---|---|---|---|---|---|---|---|
| Wt% | Horn1 | Horn2 | Horn3 | Horn4 | Horn5 | Horn6 | Horn7 | Horn8 |
| $SiO_2$ | 39.17 | 38.37 | 40.28 | 42.17 | 39.71 | 37.85 | 39.19 | 36.30 |
| $TiO_2$ | 2.94 | 3.68 | 2.89 | 2.88 | 3.03 | 6.14 | 2.63 | 7.02 |
| $Al_2O_3$ | 11.52 | 12.99 | 12.23 | 10.74 | 12.17 | 13.00 | 13.68 | 11.10 |
| $Cr_2O_3$ | 0.04 | 0.00 | 0.00 | 0.00 | 0.00 | 0.08 | 0.06 | 0.13 |
| FeO* | 16.33 | 12.58 | 15.53 | 14.50 | 15.22 | 13.38 | 12.52 | 17.70 |
| MnO | 0.44 | 0.41 | 0.40 | 0.44 | 0.34 | 0.93 | 0.27 | 0.73 |
| MgO | 8.52 | 10.20 | 8.99 | 12.26 | 10.04 | 10.32 | 10.43 | 9.48 |
| CaO | 9.46 | 9.45 | 9.44 | 9.17 | 10.87 | 9.46 | 10.37 | 9.45 |
| $Na_2O$ | 2.10 | 2.29 | 2.38 | 2.44 | 2.12 | 1.88 | 1.67 | 2.03 |
| $K_2O$ | 1.46 | 0.89 | 0.99 | 0.71 | 1.47 | 1.70 | 1.66 | 1.30 |
| $P_2O_5$ | 0.29 | 0.28 | 0.87 | 0.88 | 0.28 | 0.47 | 0.17 | 0.36 |
| Total | 92.17 | 91.14 | 94.00 | 96.19 | 95.34 | 95.67 | 92.72 | 95.62 |
| Number of ions on the basis of twenty-three | | | | | | | | |
| Si | 6.278 | 6.050 | 6.252 | 6.340 | 6.129 | 5.830 | 6.123 | 5.705 |
| Ti | 0.354 | 0.436 | 0.337 | 0.326 | 0.352 | 0.711 | 0.309 | 0.830 |
| Al | 2.176 | 2.156 | 2.235 | 1.902 | 2.213 | 2.361 | 2.520 | 2.056 |
| Cr | 0.005 | 0.000 | 0.000 | 0.000 | 0.010 | 0.000 | 0.008 | 0.017 |
| Fe | 2.189 | 1.659 | 2.016 | 1.824 | 1.964 | 1.723 | 1.636 | 2.326 |
| Mn | 0.059 | 0.055 | 0.054 | 0.056 | 0.044 | 0.121 | 0.035 | 0.097 |
| Mg | 2.036 | 2.399 | 2.078 | 0.748 | 2.310 | 2.368 | 2.430 | 2.221 |
| Ca | 1.624 | 1.597 | 1.572 | 1.477 | 1.798 | 1.562 | 1.735 | 1.592 |
| Na | 0.654 | 0.700 | 0.717 | 0.710 | 0.634 | 0.560 | 0.504 | 0.619 |
| K | 0.297 | 0.179 | 0.196 | 0.135 | 0.290 | 0.334 | 0.332 | 0.261 |
| P | 0.026 | 0.025 | 0.030 | 0.112 | 0.037 | 0.062 | 0.022 | 0.048 |
| XMg | 0.48 | 0.59 | 0.51 | 0.60 | 0.54 | 0.58 | 0.60 | 0.49 |

Table 22. Chemical compositions of hornblende microlites analyzed by EDX.

| | Hornblendes in spherulitic microlites | | | | | | Fragments | | |
|---|---|---|---|---|---|---|---|---|---|
| Wt% | Hor9 | Hor10 | Hor11 | Hor12 | Hor13 | Hor14 | Hor15 | Hor16 | Hor17 |
| $SiO_2$ | 44.17 | 44.24 | 41.06 | 43.16 | 45.75 | 45.18 | 46.16 | 41.81 | 42.11 |
| $TiO_2$ | 1.62 | 1.25 | 0.95 | 0.89 | 1.25 | 0.88 | 0.75 | 1.08 | 0.99 |
| $Al_2O_3$ | 13.27 | 14.65 | 13.26 | 12.36 | 12.35 | 13.47 | 10.19 | 14.84 | 13.41 |
| $Cr_2O_3$ | 0.00 | 0.00 | 0.02 | 0.00 | 0.09 | 0.00 | 0.01 | 0.13 | 0.00 |
| FeO* | 15.93 | 14.65 | 16.95 | 14.95 | 15.99 | 16.74 | 14.90 | 15.78 | 15.42 |
| MnO | 0.34 | 0.34 | 0.33 | 0.33 | 0.25 | 0.30 | 0.26 | 0.26 | 0.26 |
| MgO | 11.33 | 11.98 | 12.74 | 10.99 | 9.69 | 11.27 | 11.11 | 12.44 | 12.08 |
| CaO | 6.25 | 6.81 | 6.24 | 8.57 | 7.28 | 9.01 | 8.44 | 3.74 | 7.24 |
| $Na_2O$ | 2.79 | 2.33 | 1.57 | 1.76 | 2.45 | 1.41 | 1.49 | 1.02 | 2.01 |
| $K_2O$ | 0.64 | 0.61 | 1.21 | 0.76 | 0.38 | 0.88 | 1.01 | 3.27 | 1.08 |
| $P_2O_5$ | 0.24 | 0.47 | 0.28 | 0.24 | 0.19 | 0.36 | 0.18 | 0.29 | 0.13 |
| Total | 96.58 | 97.33 | 94.61 | 94.19 | 95.67 | 99.50 | 94.50 | 94.66 | 94.73 |
| Number of ions on the basis of twenty-three oxygens | | | | | | | | | |
| Si | 6.546 | 6.475 | 6.295 | 6.590 | 6.738 | 6.787 | 6.905 | 6.352 | 6.405 |
| Ti | 0.181 | 0.138 | 0.109 | 0.102 | 0.139 | 0.100 | 0.085 | 0.123 | 0.113 |
| Al | 2.317 | 2.478 | 2.395 | 2.223 | 0.338 | 1.804 | 1.942 | 2.657 | 2.404 |
| Cr | 0.000 | 0.000 | 0.003 | 0.000 | 0.011 | 0.000 | 0.001 | 0.015 | 0.000 |
| Fe | 1.974 | 1.973 | 2.173 | 1.909 | 1.970 | 2.103 | 1.865 | 2.006 | 1.962 |
| Mn | 0.042 | 0.042 | 0.042 | 0.042 | 0.032 | 0.038 | 0.033 | 0.034 | 0.033 |
| Mg | 2.503 | 2.614 | 2.911 | 2.501 | 2.127 | 2.524 | 2.477 | 2.817 | 2.739 |
| Ca | 0.993 | 1.068 | 1.024 | 1.402 | 1.149 | 1.450 | 1.353 | 0.609 | 1.180 |
| Na | 0.803 | 0.661 | 0.467 | 0.521 | 0.698 | 0.411 | 0.431 | 0.609 | 0.592 |
| K | 0.121 | 0.114 | 0.237 | 0.147 | 0.072 | 0.168 | 0.192 | 0.635 | 0.209 |
| P | 0.030 | 0.059 | 0.037 | 0.031 | 0.024 | 0.046 | 0.023 | 0.037 | 0.016 |
| XMg | 0.55 | 0.59 | 0.51 | 0.56 | 0.515 | 0.541 | 0.57 | 0.58 | 0.58 |

Table 23. Chemical compositions of pyroxene microlites analyzed by EDX.

| | Pyroxenes in spherulitic microlites | | | | | | | |
|---|---|---|---|---|---|---|---|---|
| Wt% | Pyr1 | Pyr2 | Pyr3 | Pyr4 | Pyr5 | Pyr6 | Pyr7 | Pyr8 |
| $SiO_2$ | 44.54 | 45.50 | 47.26 | 45.95 | 46.22 | 46.62 | 42.08 | 45.75 |
| $TiO_2$ | 1.32 | 1.11 | 1.08 | 1.07 | 1.03 | 0.92 | 0.95 | 1.09 |
| $Al_2O_3$ | 12.83 | 14.80 | 14.50 | 14.18 | 13.36 | 13.20 | 11.67 | 13.68 |
| $Cr_2O_3$ | 0.40 | 0.14 | 0.04 | 0.08 | 0.00 | 0.16 | 0.07 | 0.01 |
| FeO* | 15.57 | 15.00 | 14.73 | 14.59 | 15.52 | 15.15 | 16.88 | 16.18 |
| MnO | 0.37 | 0.19 | 0.33 | 0.28 | 0.21 | 0.08 | 0.29 | 0.30 |
| MgO | 16.15 | 20.17 | 16.41 | 17.83 | 19.41 | 20.63 | 12.97 | 19.58 |
| CaO | 2.18 | 1.03 | 1.73 | 1.68 | 1.31 | 0.92 | 5.95 | 1.50 |
| $Na_2O$ | 0.93 | 0.72 | 1.10 | 1.68 | 0.71 | 0.42 | 0.68 | 0.38 |
| $K_2O$ | 0.15 | 0.31 | 0.23 | 0.39 | 0.37 | 0.16 | 1.58 | 0.02 |
| $P_2O_5$ | 0.15 | 0.32 | 0.31 | 0.20 | 0.33 | 0.26 | 0.18 | 0.32 |
| Total | 94.59 | 99.29 | 97.58 | 97.01 | 98.52 | 98.46 | 93.29 | 98.80 |
| Number of ions on the basis of twelve oxygens | | | | | | | | |
| Si | 3.449 | 3.320 | 3.484 | 3.427 | 3.408 | 3.416 | 3.399 | 3.368 |
| Ti | 0.077 | 0.061 | 0.060 | 0.060 | 0.057 | 0.051 | 0.058 | 0.060 |
| Al | 1.171 | 1.273 | 1.261 | 1.246 | 1.161 | 1.140 | 1.112 | 1.187 |
| Cr | 0.005 | 0.008 | 0.003 | 0.002 | 0.000 | 0.006 | 0.005 | 0.000 |
| Fe | 1.009 | 0.915 | 0.908 | 0.910 | 0.957 | 0.928 | 1.140 | 0.996 |
| Mn | 0.024 | 0.012 | 0.021 | 0.015 | 0.015 | 0.005 | 0.020 | 0.018 |
| Mg | 1.865 | 2.194 | 1.804 | 1.982 | 2.133 | 2.253 | 1.561 | 2.148 |
| Ca | 0.181 | 0.080 | 0.137 | 0.134 | 0.104 | 0.072 | 0.515 | 0.118 |
| Na | 0.139 | 0.102 | 0.158 | 0.117 | 0.103 | 0.059 | 0.106 | 0.054 |
| K | 0.015 | 0.029 | 0.022 | 0.037 | 0.034 | 0.015 | 0.163 | 0.002 |
| P | 0.010 | 0.020 | 0.019 | 0.013 | 0.020 | 0.016 | 0.013 | 0.020 |
| Mn:Fe:Mg radios | | | | | | | | |
| Mn | 0.82 | 0.38 | 0.77 | 0.45 | 0.49 | 0.00 | 0.73 | 0.57 |
| Fe | 34.82 | 29.32 | 33.22 | 31.37 | 30.82 | 29.17 | 41.90 | 31.50 |
| Mg | 64.36 | 70.30 | 66.01 | 68.18 | 68.69 | 70.83 | 57.37 | 67.93 |

Table 24. Chemical compositions of garnet microlites analyzed by EDX.

| | Garnets (Grossular)in spherulitic microlites | | | | | | | | |
|---|---|---|---|---|---|---|---|---|---|
| Wt% | GArl | Gar2 | Gar3 | Gar4 | Gar5 | Gar6 | Gar7 | Gar8 | Gar9 |
| $SiO_2$ | 40.92 | 41.27 | 38.64 | 38.21 | 49.38 | 39.13 | 39.09 | 38.31 | 38.69 |
| $TiO_2$ | 5.50 | 0.35 | 0.00 | 0.02 | 0.49 | 0.04 | 0.06 | 0.07 | 0.11 |
| $Al_2O_3$ | 17.40 | 17.46 | 25.16 | 25.44 | 18.78 | 24.76 | 25.83 | 24.27 | 38.69 |
| $Cr_2O_3$ | 0.86 | 0.09 | 0.11 | 0.11 | 0.09 | 0.08 | 0.12 | 0.05 | 0.07 |
| FeO* | 9.69 | 13.53 | 9.90 | 9.61 | 10.17 | 10.14 | 9.80 | 10.71 | 10.37 |
| MnO | 0.06 | 0.10 | 0.18 | 0.24 | 0.00 | 0.20 | 0.22 | 0.16 | 0.21 |
| MgO | 1.95 | 3.87 | 0.04 | 0.18 | 0.61 | 0.05 | 0.06 | 0.00 | 0.18 |
| CaO | 19.24 | 17.92 | 22.80 | 22.66 | 17.19 | 22.69 | 22.99 | 22.82 | 21.99 |
| $Na_2O$ | 0.93 | 0.58 | 0.00 | 0.13 | 1.14 | 0.10 | 0.12 | 0.00 | 0.00 |
| $K_2O$ | 0.38 | 0.15 | 0.00 | 0.00 | 0.11 | 0.02 | 0.00 | 0.00 | 0.27 |
| $P_2O_5$ | 0.26 | 0.21 | 0.27 | 0.14 | 0.57 | 0.21 | 0.16 | 0.00 | 0.20 |
| Total | 96.38 | 95.49 | 97.08 | 96.78 | 98.68 | 97.07 | 98.43 | 96.38 | 97.73 |
| Number of ions on the basis of twelve oxygens | | | | | | | | | |
| Si | 3.182 | 3.269 | 2.974 | 2.952 | 3.633 | 2.966 | 2.967 | 2.991 | 2.990 |
| Ti | 0.322 | 0.020 | 0.000 | 0.002 | 0.027 | 0.002 | 0.003 | 0.005 | 0.006 |
| Al | 1.595 | 1.630 | 2.242 | 2.316 | 1.629 | 2.270 | 2.312 | 2.234 | 2.258 |
| Cr | 0.004 | 0.006 | 0.006 | 0.006 | 0.006 | 0.004 | 0.008 | 0.003 | 0.005 |
| Fe | 0.630 | 0.896 | 0.638 | 0.620 | 0.626 | 0.660 | 0.623 | 0.669 | 0.671 |
| Mn | 0.004 | 0.006 | 0.012 | 0.016 | 0.000 | 0.014 | 0.014 | 0.011 | 0.014 |
| Mg | 0.226 | 0.458 | 0.004 | 0.020 | 0.066 | 0.006 | 0.008 | 0.000 | 0.021 |
| Ca | 1.603 | 1.531 | 1.880 | 1.876 | 1.355 | 1.892 | 1.871 | 1.908 | 1.821 |
| Na | 0.140 | 0.089 | 0.000 | 0.024 | 0.162 | 0.016 | 0.017 | 0.000 | 0.000 |
| K | 0.038 | 0.015 | 0.000 | 0.000 | 0.011 | 0.002 | 0.000 | 0.000 | 0.023 |
| P | 0.017 | 0.014 | 0.018 | 0.008 | 0.036 | 0.014 | 0.011 | 0.000 | 0.014 |
| Mn:Fe:Mg radios | | | | | | | | | |
| Mn | 0.47 | 0.44 | 1.83 | 2.46 | 0.00 | 2.06 | 2.17 | 1.62 | 2.13 |
| Fe | 73.25 | 65.88 | 97.55 | 94.51 | 90.46 | 97.06 | 96.59 | 98.38 | 94.90 |
| Mg | 26.28 | 33.68 | 0.62 | 3.05 | 9.54 | 0.84 | 1.24 | 0.00 | 2.97 |

Table 25. Chemical compositions of ilmenite, spinel, magnetic mineral and apatite microlites analyzed by EDX.

| | Ilmenite | | | Spinel | | | Magnetic mineral | | Apatite |
|---|---|---|---|---|---|---|---|---|---|
| Wt% | Ilm1 | Ilm2 | Ilm3 | Spi1 | Spi2 | Spi4 | Mag1 | Mag2 | Apa1 |
| $SiO_2$ | 0.13 | 2.58 | 4.10 | 0.60 | 2.28 | 11.33 | 8.78 | 19.39 | 0.74 |
| $TiO_2$ | 48.62 | 47.33 | 55.63 | 1.20 | 1.60 | 0.31 | 11.36 | 5.56 | 0.09 |
| $Al_2O_3$ | 0.67 | 3.18 | 3.28 | 41.48 | 27.04 | 46.18 | 8.06 | 9.03 | 0.02 |
| $Cr_2O_3$ | 0.00 | 0.02 | 0.00 | 0.11 | 0.12 | 0.07 | 0.12 | 0.15 | 0.00 |
| FeO* | 40.72 | 36.37 | 27.20 | 42.19 | 57.60 | 27.83 | 55.33 | 50.43 | 2.70 |
| MnO | 3.67 | 0.13 | 1.27 | 1.59 | 1.55 | 0.55 | 1.67 | 0.96 | 2.34 |
| MgO | 0.15 | 4.35 | 1.79 | 4.54 | 0.68 | 7.46 | 2.17 | 3.65 | 4.39 |
| CaO | 0.00 | 0.13 | 0.31 | 0.13 | 0.26 | 0.75 | 1.56 | 0.50 | 43.74 |
| $Na_2O$ | 0.19 | 0.34 | 0.53 | 0.28 | 0.33 | 1.09 | 0.61 | 0.71 | 0.62 |
| $K_2O$ | 0.04 | 0.26 | 0.13 | 0.13 | 0.18 | 0.61 | 0.61 | 3.40 | 0.16 |
| $P_2O_5$ | 0.12 | 0.11 | 0.10 | 0.14 | 0.12 | 0.00 | 0.19 | 0.20 | 41.66 |
| NiO | 0.00 | 0.00 | 0.01 | 0.50 | 0.38 | 0.00 | 0.00 | 0.28 | 0.01 |
| Total | 94.31 | 94.88 | 94.37 | 93.15 | 92.24 | 96.18 | 90.46 | 94.26 | 96.46 |
| Actomic radios (Ilmenite:6; Spinel and magnetic mineral:24; Apatite:26) | | | | | | | | | |
| Si | 0.007 | 0.122 | 0.147 | 0.119 | 0.570 | 1.715 | 2.044 | 4.024 | 0.130 |
| Ti | 1.429 | 2.049 | 2.005 | 0.178 | 0.302 | 0.040 | 1.988 | 0.868 | 0.013 |
| Al | 0.168 | 0.178 | 0.185 | 9.748 | 6.210 | 9.203 | 2.212 | 2.208 | 0.004 |
| Cr | 0.000 | 0.001 | 0.000 | 0.017 | 0.024 | 0.010 | 0.020 | 0.024 | 0.000 |
| Fe | 1.819 | 1.045 | 1.089 | 6.974 | 12.065 | 3.934 | 10.776 | 8.752 | 6.394 |
| Mn | 0.166 | 0.005 | 0.051 | 0.267 | 0.330 | 0.078 | 0.328 | 0.168 | 0.347 |
| Mg | 0.012 | 0.309 | 0.128 | 1.338 | 0.255 | 1.879 | 0.752 | 0.282 | 1.148 |
| Ca | 0.000 | 0.009 | 0.016 | 0.028 | 0.070 | 0.135 | 0.388 | 0.112 | 8.220 |
| Na | 0.020 | 0.032 | 0.049 | 0.109 | 0.159 | 0.356 | 0.276 | 0.288 | 0.212 |
| K | 0.003 | 0.016 | 0.008 | 0.032 | 0.058 | 0.131 | 0.180 | 0.225 | 0.035 |
| P | 0.009 | 0.008 | 0.008 | 0.010 | 0.009 | 0.000 | 0.040 | 0.026 | 6.184 |
| Ni | 0.000 | 0.002 | 0.000 | 0.000 | 0.000 | 0.000 | 0.000 | 0.038 | 0.000 |
| Total | 3.633 | 3.776 | 3.686 | 18.82 | 20.07 | 17.68 | 14.01 | 17.40 | 16.70 |

Table 26. Bulk composition of rocks used in frictional experiments by XRF.

| Wt% | 01 | 02 | 03 | 04 | 05 | 06 | 07 | 08 |
|---|---|---|---|---|---|---|---|---|
| $SiO_2$ | 52.51 | 49.85 | 72.75 | 71.93 | 71.60 | 51.52 | 81.68 | 96.87 |
| $TiO_2$ | 0.19 | 2.85 | 0.24 | 0.30 | 0.49 | 0.16 | 0.02 | 0.09 |
| $Al_2O_3$ | 18.44 | 16.56 | 14.07 | 15.21 | 15.10 | 29.71 | 11.93 | 1.79 |
| FeO* | 5.97 | 10.11 | 2.14 | 2.39 | 2.94 | 1.26 | 0.43 | 2.72 |
| MnO | 0.15 | 0.15 | 0.06 | 0.05 | 0.07 | 0.02 | 0.01 | 0.26 |
| MgO | 6.94 | 4.90 | 0.37 | 0.48 | 0.64 | 0.63 | 0.18 | 0.59 |
| CaO | 13.25 | 8.20 | 1.40 | 2.37 | 2.16 | 14.35 | 0.27 | 0.28 |
| $Na_2O$ | 2.38 | 3.13 | 3.87 | 3.50 | 3.05 | 3.12 | 6.82 | 0.03 |
| $K_2O$ | 0.18 | 2.76 | 5.01 | 3.16 | 4.00 | 0.20 | 0.04 | 0.20 |
| $P_2O_5$ | 0.01 | 1.58 | 0.10 | 0.09 | 0.15 | 0.02 | 0.05 | 0.09 |
| Total | 102.90 | 100.09 | 100.88 | 101.28 | 99.78 | 101.89 | 101.76 | 102.89 |

Table 27. Chemical compositions of glass matrix in experimental pseudotachylite generated in medium-grained gabbro sample analyzed by EDX.

| Wt% | Ga1 | Ga2 | Ga3 | Ga4 | Ga5 | Ga6 | Ga7 | Ga8 | Ga9 |
|---|---|---|---|---|---|---|---|---|---|
| $SiO_2$ | 53.09 | 53.22 | 53.24 | 53.93 | 52.17 | 52.83 | 52.36 | 52.65 | 52.38 |
| $TiO_2$ | 0.18 | 0.13 | 0.16 | 0.00 | 0.36 | 0.00 | 0.25 | 0.50 | 0.35 |
| $Al_2O_3$ | 16.88 | 16.28 | 18.92 | 24.24 | 1.20 | 25.25 | 14.97 | 1.11 | 1.36 |
| FeO | 6.15 | 6.51 | 5.42 | 2.46 | 8.24 | 2.56 | 7.94 | 8.53 | 9.11 |
| MnO | 0.26 | 0.00 | 0.11 | 0.04 | 0.16 | 0.04 | 0.06 | 0.45 | 0.16 |
| MgO | 7.52 | 9.30 | 5.80 | 3.12 | 13.60 | 3.02 | 8.32 | 14.42 | 14.08 |
| CaO | 12.27 | 12.26 | 12.04 | 12.21 | 20.68 | 12.20 | 11.80 | 21.10 | 20.60 |
| $Na_2O$ | 1.83 | 1.90 | 2.54 | 3.33 | 0.00 | 3.43 | 1.42 | 0.16 | 0.01 |
| $K_2O$ | 0.23 | 0.27 | 0.13 | 0.24 | 0.11 | 0.24 | 0.26 | 0.00 | 0.02 |
| $Cr_2O_3$ | 0.05 | 0.00 | 0.19 | 0.03 | 0.16 | 0.04 | 0.16 | 0.00 | 0.23 |
| NiO | 0.62 | 0.29 | 0.00 | 0.00 | 0.07 | 0.00 | 0.35 | 0.36 | 0.23 |
| $P_2O_5$ | 0.18 | 0.43 | 0.32 | 0.13 | 0.19 | 0.12 | 0.27 | 0.21 | 0.29 |
| Total | 99.26 | 100.59 | 98.87 | 99.72 | 96.94 | 99.73 | 98.16 | 99.49 | 98.82 |
| Number of ions based of twenty-four oxygens | | | | | | | | | |
| Si | 7.559 | 7.456 | 7.516 | 7.302 | 7.960 | 7.293 | 7.568 | 7.866 | 7.876 |
| Ti | 0.019 | 0.012 | 0.016 | 0.000 | 0.040 | 0.000 | 0.028 | 0.057 | 0.040 |
| Al | 2.833 | 2.692 | 3.148 | 4.109 | 0.216 | 4.108 | 2.552 | 0.195 | 0.240 |
| Fe | 0.733 | 0.764 | 0.640 | 0.366 | 1.052 | 0.355 | 0.720 | 1.065 | 1.144 |
| Mn | 0.031 | 0.000 | 0.012 | 0.004 | 0.020 | 0.004 | 1.792 | 0.019 | 0.021 |
| Mg | 1.597 | 1.944 | 1.220 | 3.096 | 0.621 | 3.092 | 0.621 | 1.070 | 3.137 |
| Ca | 1.872 | 1.640 | 1.402 | 1.803 | 3.340 | 1.803 | 1.628 | 3.378 | 3.320 |
| Na | 0.504 | 0.507 | 0.700 | 0.000 | 1.224 | 0.918 | 0.400 | 0.048 | 0.004 |
| K | 0.041 | 0.048 | 0.024 | 0.042 | 0.024 | 0.043 | 0.048 | 0.000 | 0.004 |
| Cr | 0.006 | 0.000 | 0.020 | 0.003 | 0.020 | 0.003 | 0.016 | 0.000 | 0.028 |
| Ni | 0.007 | 0.032 | 0.036 | 0.000 | 0.008 | 0.000 | 0.040 | 0.015 | 0.028 |
| P | 0.020 | 0.042 | 0.028 | 0.015 | 0.024 | 0.015 | 0.032 | 0.027 | 0.036 |
| Total | 15.222 | 15.137 | 14.762 | 16.740 | 14.547 | 18.183 | 15.445 | 13.735 | 15.877 |

Table 28. Chemical compositionas of glass matrix in experimental pseudotachylite generated in fine-grained gabbro sample analyzed by EDX.

| | Glass matrix in fine-grained gabbro sample | | | | | | | | |
|---|---|---|---|---|---|---|---|---|---|
| Wt% | 1 | 2 | 3 | 4 | 5 | 6 | 7 | 8 | 9 |
| $SiO_2$ | 47.53 | 49.18 | 46.91 | 47.78 | 46.83 | 47.27 | 47.17 | 46.32 | 46.62 |
| $TiO_2$ | 3.54 | 3.02 | 3.56 | 3.28 | 2.99 | 3.35 | 3.23 | 3.45 | 3.62 |
| $Al_2O_3$ | 16.33 | 16.86 | 16.23 | 16.88 | 16.40 | 16.97 | 15.75 | 16.40 | 16.35 |
| FeO* | 9.88 | 8.57 | 10.11 | 9.60 | 10.43 | 9.96 | 10.31 | 10.04 | 10.28 |
| MnO | 0.16 | 0.20 | 0.15 | 0.22 | 0.21 | 0.24 | 0.11 | 0.00 | 0.09 |
| MgO | 6.32 | 5.18 | 5.41 | 5.95 | 5.74 | 5.60 | 6.27 | 6.28 | 6.22 |
| CaO | 6.98 | 5.88 | 7.46 | 7.25 | 7.09 | 7.37 | 7.48 | 6.93 | 6.92 |
| $Na_2O$ | 2.64 | 2.63 | 2.66 | 3.02 | 3.07 | 2.70 | 2.80 | 2.76 | 2.48 |
| $K_2O$ | 3.78 | 5.14 | 2.92 | 2.98 | 3.16 | 3.10 | 3.48 | 3.54 | 3.59 |
| $Cr_2O_3$ | 0.14 | 0.08 | 0.00 | 0.00 | 0.00 | 0.00 | 0.05 | 0.14 | 0.06 |
| NiO | 0.08 | 0.00 | 0.08 | 0.26 | 0.00 | 0.15 | 0.07 | 0.48 | 0.01 |
| $P_2O_5$ | 1.77 | 1.43 | 1.60 | 1.80 | 1.59 | 1.55 | 1.58 | 1.45 | 1.60 |
| SeO | 0.07 | 0.70 | 0.26 | 0.40 | 0.17 | 0.20 | 0.39 | 0.41 | 0.34 |
| Total | 99.22 | 98.87 | 97.35 | 99.42 | 97.68 | 98.46 | 98.69 | 98.20 | 98.18 |
| Number of ions on the basis of twenty-four oxygens | | | | | | | | | |
| Si | 6.975 | 7.220 | 7.012 | 6.978 | 6.993 | 6.980 | 6.996 | 6.912 | 6.936 |
| Ti | 0.390 | 0.333 | 0.400 | 0.360 | 0.336 | 0.372 | 2.360 | 0.388 | 0.404 |
| Al | 2.824 | 2.918 | 2.860 | 2.906 | 2.887 | 2.954 | 2.756 | 2.881 | 2.868 |
| Fe | 1.213 | 1.052 | 1.264 | 1.173 | 1.303 | 1.230 | 1.280 | 1.252 | 1.280 |
| Mn | 0.020 | 0.024 | 0.019 | 0.027 | 0.026 | 0.030 | 0.012 | 0.000 | 0.012 |
| Mg | 1.382 | 1.133 | 1.205 | 1.295 | 1.278 | 1.234 | 1.384 | 1.396 | 1.380 |
| Ca | 1.097 | 0.924 | 1.195 | 1.134 | 1.135 | 1.167 | 1.188 | 1.108 | 1.104 |
| Na | 0.751 | 0.748 | 0.771 | 0.856 | 0.889 | 0.773 | 0.808 | 0.800 | 0.716 |
| K | 0.707 | 0.968 | 0.556 | 0.555 | 0.602 | 0.584 | 0.656 | 0.676 | 0.680 |
| Cr | 0.017 | 0.009 | 0.000 | 0.000 | 0.000 | 0.000 | 0.008 | 0.016 | 0.008 |
| Ni | 0.009 | 0.000 | 0.010 | 0.031 | 0.000 | 0.018 | 0.008 | 0.056 | 0.000 |
| P | 0.220 | 0.178 | 0.202 | 0.222 | 0.201 | 0.194 | 0.200 | 0.196 | 0.200 |
| Se | 0.006 | 0.065 | 0.024 | 0.037 | 0.016 | 0.019 | 0.036 | 0.040 | 0.032 |
| Total | 15.611 | 15.572 | 15.518 | 15.574 | 15.666 | 15.555 | 17.692 | 15.721 | 15.620 |

Table 29. Chemical compositions of glass matrix in experimental pseudotachylite generated in coarse-grained granite sample analyzed.

| | Glass matrix in coarse-grained granite samples | | | | | | | | |
|---|---|---|---|---|---|---|---|---|---|
| Wt% | 1 | 2 | 3 | 4 | 5 | 6 | 7 | 8 | 9 |
| $SiO_2$ | 65.56 | 65.62 | 66.24 | 64.18 | 70.27 | 67.40 | 68.36 | 47.78 | 46.72 |
| $TiO_2$ | 0.09 | 0.20 | 0.31 | 0.29 | 0.09 | 0.26 | 0.32 | 11.08 | 11.31 |
| $Al_2O_3$ | 18.75 | 19.12 | 17.26 | 18.49 | 16.56 | 17.86 | 17.33 | 13.67 | 13.26 |
| FeO* | 0.94 | 2.41 | 1.73 | 2.18 | 0.71 | 1.01 | 1.29 | 7.82 | 8.23 |
| MnO | 0.00 | 0.00 | 0.00 | 0.04 | 0.05 | 0.05 | 0.02 | 1.49 | 1.56 |
| MgO | 0.00 | 0.30 | 0.04 | 0.30 | 0.18 | 0.25 | 0.21 | 0.38 | 0.22 |
| CaO | 1.02 | 1.02 | 0.85 | 1.02 | 0.71 | 0.93 | 0.90 | 1.74 | 1.73 |
| $Na_2O$ | 5.81 | 4.02 | 4.09 | 3.98 | 4.29 | 4.22 | 4.38 | 2.79 | 2.73 |
| $K_2O$ | 5.00 | 6.83 | 6.29 | 6.24 | 6.20 | 7.15 | 5.59 | 4.67 | 4.47 |
| $Cr_2O_3$ | 0.00 | 0.00 | 0.07 | 0.09 | 0.09 | 0.05 | 0.06 | 0.03 | 0.04 |
| NiO | 0.00 | 0.10 | 0.08 | 0.00 | 0.04 | 0.06 | 0.03 | 0.04 | 0.00 |
| $P_2O_5$ | 0.35 | 0.68 | 0.11 | 0.36 | 0.54 | 0.37 | 0.48 | 0.68 | 0.66 |
| SeO | 0.60 | 0.20 | 0.00 | 0.19 | 0.52 | 0.62 | 0.53 | 0.50 | 0.52 |
| Total | 98.12 | 100.50 | 97.07 | 97.36 | 100.15 | 100.15 | 99.50 | 92.67 | 91.46 |
| Number of ions on the basis of twenty-four oxygens | | | | | | | | | |
| Si | 8.931 | 8.814 | 9.124 | 8.868 | 9.300 | 9.040 | 9.142 | 7.440 | 7.399 |
| Ti | 0.009 | 0.021 | 0.032 | 0.030 | 0.008 | 0.026 | 0.032 | 1.298 | 1.346 |
| Al | 3.010 | 3.027 | 2.802 | 3.012 | 2.584 | 2.824 | 2.732 | 2.509 | 2.475 |
| Fe | 0.107 | 0.270 | 0.199 | 0.252 | 0.079 | 0.113 | 0.144 | 1.019 | 1.090 |
| Mn | 0.000 | 0.000 | 0.000 | 0.005 | 0.006 | 0.000 | 0.002 | 0.196 | 0.209 |
| Mg | 0.000 | 0.060 | 0.008 | 0.061 | 0.035 | 0.050 | 0.041 | 0.087 | 0.051 |
| Ca | 0.148 | 0.147 | 0.126 | 0.150 | 0.101 | 0.133 | 0.129 | 0.290 | 0.293 |
| Na | 1.535 | 1.047 | 1.093 | 1.067 | 1.100 | 1.096 | 1.135 | 0.844 | 0.837 |
| K | 0.862 | 1.170 | 1.106 | 1.100 | 1.046 | 1.224 | 0.953 | 0.928 | 0.903 |
| Cr | 0.000 | 0.000 | 0.008 | 0.010 | 0.009 | 0.005 | 0.006 | 0.004 | 0.005 |
| P | 0.040 | 0.077 | 0.013 | 0.042 | 0.060 | 0.042 | 0.055 | 0.090 | 0.088 |
| Se | 0.052 | 0.002 | 0.000 | 0.016 | 0.044 | 0.053 | 0.044 | 0.048 | 0.052 |
| Total | 14.694 | 14.625 | 14.511 | 14.613 | 14.372 | 14.606 | 14.415 | 14.753 | 14.748 |

Table 30. Chemical compositions of glass matrix in experimental pseudotachylite in medium-grained granite sample.

| | Glass matrix in medium-grained granite sample | | | | | | | | |
|---|---|---|---|---|---|---|---|---|---|
| Wt% | 1 | 2 | 3 | 4 | 5 | 6 | 7 | 8 | 9 |
| $SiO_2$ | 61.12 | 64.53 | 65.51 | 61.67 | 63.12 | 63.10 | 60.81 | 67.31 | 41.13 |
| $TiO_2$ | 0.51 | 0.17 | 0.14 | 0.42 | 0.48 | 0.35 | 0.49 | 0.29 | 1.85 |
| $Al_2O_3$ | 20.52 | 20.37 | 20.68 | 19.78 | 20.54 | 21.39 | 20.58 | 17.15 | 20.21 |
| FeO* | 3.72 | 1.52 | 1.74 | 3.80 | 3.29 | 3.65 | 3.76 | 2.65 | 18.45 |
| MnO | 0.18 | 0.02 | 0.08 | 0.01 | 0.00 | 0.01 | 0.08 | 0.10 | 0.74 |
| MgO | 0.62 | 0.34 | 0.50 | 0.83 | 0.55 | 0.67 | 0.72 | 0.66 | 8.70 |
| CaO | 3.11 | 3.55 | 3.59 | 3.07 | 2.59 | 3.60 | 2.95 | 2.68 | 2.20 |
| $Na_2O$ | 3.71 | 5.00 | 4.98 | 3.43 | 3.92 | 4.54 | 3.56 | 3.59 | 1.58 |
| $K_2O$ | 4.36 | 3.67 | 3.06 | 4.51 | 3.40 | 3.26 | 5.14 | 3.40 | 3.16 |
| $Cr_2O_3$ | 0.00 | 0.01 | 0.10 | 0.00 | 0.05 | 0.03 | 0.00 | 0.06 | 0.03 |
| NiO | 0.00 | 0.00 | 0.10 | 0.00 | 0.03 | 0.05 | 0.06 | 0.06 | 0.00 |
| $P_2O_5$ | 0.34 | 0.14 | 0.28 | 0.28 | 0.29 | 0.26 | 0.37 | 0.49 | 0.15 |
| SeO | 0.00 | 0.33 | 0.07 | 0.10 | 0.00 | 0.00 | 0.11 | 0.58 | 0.17 |
| Total | 98.19 | 99.65 | 100.83 | 97.90 | 98.26 | 100.91 | 98.63 | 99.02 | 98.37 |
| Number of ions on the basis of twenty-four oxygens | | | | | | | | | |
| Si | 8.435 | 8.667 | 8.663 | 8.528 | 8.531 | 8.443 | 8.397 | 9.039 | 6.319 |
| Ti | 0.053 | 0.017 | 0.014 | 0.044 | 0.048 | 0.036 | 0.051 | 0.285 | 0.214 |
| Al | 3.338 | 3.224 | 3.224 | 3.224 | 3.273 | 3.370 | 3.349 | 2.714 | 3.661 |
| Fe | 0.430 | 0.171 | 0.192 | 0.440 | 0.372 | 0.408 | 0.434 | 0.297 | 2.371 |
| Mn | 0.178 | 0.002 | 0.009 | 0.001 | 0.000 | 0.001 | 0.010 | 0.011 | 0.097 |
| Mg | 0.128 | 0.068 | 0.098 | 0.171 | 0.111 | 0.133 | 0.148 | 0.131 | 1.991 |
| Ca | 0.992 | 0.511 | 0.509 | 0.455 | 0.376 | 0.516 | 0.437 | 0.385 | 0.363 |
| Na | 0.992 | 1.301 | 1.278 | 0.920 | 1.026 | 1.175 | 0.953 | 0.934 | 0.471 |
| K | 0.768 | 0.629 | 0.516 | 0.796 | 0.931 | 0.556 | 0.909 | 0.582 | 0.619 |
| Cr | 0.000 | 0.001 | 0.010 | 0.000 | 0.006 | 0.003 | 0.000 | 0.006 | 0.004 |
| P | 0.040 | 0.016 | 0.030 | 0.032 | 0.033 | 0.029 | 0.043 | 0.056 | 0.020 |
| Se | 0.000 | 0.028 | 0.006 | 0.009 | 0.000 | 0.000 | 0.000 | 0.049 | 0.016 |
| Total | 15.714 | 14.635 | 14.549 | 14.620 | 14.707 | 14.670 | 14.731 | 14.489 | 16.146 |

Table 31. Chemical compositions of glass matrix in experimental pseudotachylite generated in fine-grained granite sample.

| | Glass matrix in fine-grained granite sample | | | | | | | | |
|---|---|---|---|---|---|---|---|---|---|
| Wt% | 1 | 2 | 3 | 4 | 5 | 6 | 7 | 8 | 9 |
| $SiO_2$ | 65.70 | 61.58 | 63.53 | 62.43 | 61.26 | 61.73 | 64.02 | 64.86 | 50.07 |
| $TiO_2$ | 0.41 | 0.45 | 0.47 | 0.37 | 0.48 | 0.52 | 0.25 | 0.52 | 1.04 |
| $Al_2O_3$ | 17.48 | 19.98 | 17.87 | 19.32 | 19.82 | 19.97 | 19.93 | 18.61 | 19.61 |
| FeO* | 2.48 | 3.56 | 3.85 | 3.20 | 3.38 | 3.61 | 1.95 | 3.59 | 11.98 |
| MnO | 0.04 | 0.05 | 0.00 | 0.05 | 0.18 | 0.08 | 0.01 | 0.03 | 0.48 |
| MgO | 0.44 | 0.79 | 0.69 | 0.74 | 0.60 | 0.57 | 0.17 | 0.72 | 1.11 |
| CaO | 2.56 | 2.85 | 2.57 | 2.56 | 2.82 | 2.91 | 3.21 | 2.42 | 3.87 |
| $Na_2O$ | 4.18 | 3.88 | 3.70 | 4.00 | 3.86 | 3.81 | 4.76 | 3.26 | 3.40 |
| $K_2O$ | 3.64 | 4.58 | 4.40 | 4.93 | 4.86 | 4.40 | 3.43 | 4.46 | 2.76 |
| $Cr_2O_3$ | 0.00 | 0.01 | 0.01 | 0.01 | 0.00 | 0.00 | 0.00 | 0.00 | 0.00 |
| NiO | 0.01 | 0.01 | 0.00 | 0.00 | 0.00 | 0.00 | 0.00 | 0.02 | 0.01 |
| $P_2O_5$ | 0.05 | 0.06 | 0.05 | 0.04 | 0.04 | 0.07 | 0.01 | 0.06 | 0.05 |
| SeO | 0.04 | 0.06 | 0.07 | 0.04 | 0.06 | 0.04 | 0.02 | 0.02 | 0.03 |
| Total | 97.03 | 97.86 | 97.21 | 97.69 | 97.36 | 97.71 | 97.76 | 98.57 | 94.41 |
| Number of ions on the basis of twenty-four oxygens | | | | | | | | | |
| Si | 8.959 | 8.455 | 8.746 | 8.595 | 8.494 | 8.481 | 8.721 | 8.770 | 7.296 |
| Ti | 0.042 | 0.046 | 0.049 | 0.039 | 0.050 | 0.053 | 0.025 | 0.053 | 0.114 |
| Al | 2.809 | 3.233 | 2.899 | 3.135 | 3.238 | 3.235 | 3.201 | 2.965 | 3.369 |
| Fe | 0.283 | 0.409 | 0.443 | 0.368 | 0.391 | 0.415 | 0.222 | 0.406 | 1.459 |
| Mn | 0.005 | 0.006 | 0.000 | 0.006 | 0.022 | 0.010 | 0.002 | 0.003 | 0.059 |
| Mg | 0.090 | 0.162 | 0.142 | 0.152 | 0.125 | 0.118 | 0.035 | 0.144 | 1.106 |
| Ca | 0.373 | 0.420 | 0.379 | 0.378 | 0.419 | 0.429 | 0.439 | 0.351 | 0.604 |
| Na | 1.105 | 1.033 | 0.987 | 1.067 | 1.038 | 1.014 | 1.257 | 0.855 | 0.959 |
| K | 0.633 | 0.802 | 0.767 | 0.867 | 0.860 | 0.772 | 0.596 | 0.855 | 0.513 |
| Cr | 0.000 | 0.012 | 0.009 | 0.010 | 0.000 | 0.000 | 0.002 | 0.001 | 0.000 |
| Ni | 0.008 | 0.006 | 0.000 | 0.000 | 0.000 | 0.000 | 0.004 | 0.018 | 0.005 |
| P | 0.046 | 0.062 | 0.053 | 0.044 | 0.037 | 0.068 | 0.012 | 0.060 | 0.051 |
| Se | 0.042 | 0.055 | 0.072 | 0.036 | 0.057 | 0.044 | 0.016 | 0.021 | 0.027 |
| Total | 14.198 | 14.701 | 14.546 | 14.697 | 14.731 | 14.639 | 14.532 | 14.502 | 14.958 |

Table 32. Chemical compositions of glass matrix generated by frictional melting experiment in albitite-quartzite pair sample.

| | Ab1 | Ab2 | Ab3 | Ab4 | Ab5 | Ab6 | Ab7 | Ab8 | Ab9 |
|---|---|---|---|---|---|---|---|---|---|
| Wt% | 1 | 2 | 3 | 4 | 5 | 6 | 7 | 8 | 9 |
| $SiO_2$ | 68.12 | 67.91 | 67.74 | 67.98 | 67.92 | 67.98 | 67.63 | 74.23 | 76.51 |
| $TiO_2$ | 0.03 | 0.00 | 0.00 | 0.00 | 0.03 | 0.05 | 0.00 | 0.00 | 0.10 |
| $Al_2O_3$ | 20.29 | 19.34 | 19.40 | 20.39 | 19.82 | 20.05 | 19.96 | 14.78 | 12.76 |
| FeO* | 0.10 | 0.06 | 0.06 | 0.00 | 0.04 | 0.04 | 0.24 | 0.30 | 0.04 |
| MnO | 0.00 | 0.00 | 0.01 | 0.07 | 0.00 | 0.00 | 0.12 | 0.00 | 0.00 |
| MgO | 0.00 | 0.02 | 0.00 | 0.00 | 0.00 | 0.02 | 0.02 | 0.00 | 0.07 |
| CaO | 0.58 | 0.03 | 0.08 | 0.39 | 0.24 | 0.45 | 0.61 | 0.32 | 0.26 |
| $Na_2O$ | 10.51 | 11.16 | 10.92 | 11.00 | 10.51 | 10.68 | 10.29 | 7.04 | 8.29 |
| $K_2O$ | 0.00 | 0.00 | 0.02 | 0.00 | 0.00 | 0.00 | 0.11 | 0.09 | 0.15 |
| $Cr_2O_3$ | 0.01 | 0.00 | 0.00 | 0.01 | 0.03 | 0.05 | 0.01 | 0.00 | 0.19 |
| NiO | 0.00 | 0.05 | 0.07 | 0.00 | 0.00 | 0.02 | 0.02 | 0.00 | 0.22 |
| $P_2O_5$ | 0.38 | 0.24 | 0.42 | 0.45 | 0.50 | 0.53 | 0.25 | 0.16 | 0.57 |
| SeO | 0.72 | 0.75 | 0.64 | 0.53 | 0.56 | 0.89 | 0.52 | 0.16 | 0.57 |
| Total | 100.74 | 99.56 | 99.45 | 100.82 | 99.65 | 101.21 | 99.76 | 97.08 | 99.73 |
| Number of ions on the basis of twenty-four oxygens | | | | | | | | | |
| Si | 8.869 | 8.911 | 8.939 | 8.845 | 8.915 | 8.849 | 8.910 | 9.759 | 9.863 |
| Ti | 0.003 | 0.000 | 0.000 | 0.000 | 0.003 | 0.005 | 0.000 | 0.000 | 0.010 |
| Al | 3.115 | 3.068 | 3.018 | 3.126 | 3.066 | 3.090 | 3.043 | 2.290 | 1.939 |
| Fe | 0.011 | 0.007 | 0.007 | 0.000 | 0.004 | 0.004 | 0.005 | 0.033 | 0.004 |
| Mn | 0.000 | 0.000 | 0.001 | 0.008 | 0.000 | 0.000 | 0.000 | 0.000 | 0.000 |
| Mg | 0.000 | 0.003 | 0.000 | 0.000 | 0.000 | 0.005 | 0.003 | 0.000 | 0.014 |
| Ca | 0.081 | 0.004 | 0.011 | 0.055 | 0.033 | 0.063 | 0.052 | 0.045 | 0.036 |
| Na | 2.653 | 2.839 | 2.795 | 2.775 | 2.674 | 2.708 | 2.705 | 1.793 | 2.073 |
| K | 0.000 | 0.000 | 0.004 | 0.000 | 0.000 | 0.000 | 0.000 | 0.016 | 0.024 |
| Cr | 0.001 | 0.000 | 0.000 | 0.001 | 0.003 | 0.005 | 0.001 | 0.000 | 0.019 |
| Ni | 0.000 | 0.006 | 0.008 | 0.000 | 0.000 | 0.002 | 0.002 | 0.000 | 0.022 |
| P | 0.042 | 0.027 | 0.046 | 0.050 | 0.055 | 0.059 | 0.027 | 0.018 | 0.062 |
| Se | 0.060 | 0.062 | 0.053 | 0.044 | 0.047 | 0.073 | 0.042 | 0.020 | 0.038 |
| Total | 14.835 | 14.927 | 14.870 | 14.904 | 14.800 | 14.863 | 14.79 | 13.973 | 14.094 |

Table 33. Chemical compositions of glass matrix generated by frictional melting experiment in anorthosite sample.

| | An1 | An2 | An3 | An4 | An5 | An6 | An7 | An8 | An9 |
|---|---|---|---|---|---|---|---|---|---|
| Wt% | 1 | 2 | 3 | 4 | 5 | 6 | 7 | 8 | 9 |
| $SiO_2$ | 48.79 | 49.75 | 48.99 | 51.57 | 49.72 | 49.73 | 49.93 | 66.88 | 49.24 |
| $TiO_2$ | 0.51 | 0.34 | 0.63 | 0.00 | 0.33 | 0.31 | 0.37 | 0.01 | 0.04 |
| $Al_2O_3$ | 29.25 | 29.21 | 27.81 | 31.67 | 30.60 | 30.27 | 28.75 | 20.11 | 30.75 |
| FeO* | 2.82 | 2.66 | 3.39 | 0.11 | 1.78 | 1.99 | 2.61 | 0.00 | 1.55 |
| MnO | 0.25 | 0.00 | 0.14 | 0.00 | 0.04 | 0.07 | 0.00 | 0.00 | 0.00 |
| MgO | 1.93 | 1.55 | 2.40 | 0.00 | 0.97 | 0.88 | 1.44 | 0.52 | 0.77 |
| CaO | 13.41 | 13.04 | 12.54 | 10.42 | 13.28 | 13.36 | 13.48 | 0.00 | 13.61 |
| $Na_2O$ | 2.43 | 2.85 | 3.13 | 3.50 | 2.97 | 2.64 | 3.31 | 11.14 | 2.78 |
| $K_2O$ | 0.24 | 0.31 | 0.42 | 0.01 | 0.15 | 0.20 | 0.39 | 0.02 | 0.18 |
| $Cr_2O_3$ | 0.03 | 0.04 | 0.25 | 0.00 | 0.00 | 0.09 | 0.07 | 0.00 | 0.14 |
| NiO | 0.28 | 0.00 | 0.00 | 1.74 | 0.21 | 0.29 | 0.09 | 0.00 | 0.14 |
| $P_2O_5$ | 0.00 | 0.21 | 0.37 | 0.05 | 0.13 | 0.31 | 0.09 | 0.57 | 0.03 |
| SeO | 0.31 | 0.00 | 0.05 | 1.76 | 0.71 | 0.00 | 0.17 | 0.91 | 0.42 |
| Total | 100.25 | 99.96 | 97.72 | 100.83 | 100.89 | 100.14 | 100.70 | 100.16 | 99.61 |
| Number of ions on the basis of twenty-four oxygens | | | | | | | | | |
| Si | 6.761 | 6.841 | 6.815 | 7.017 | 6.812 | 6.840 | 6.884 | 8.794 | 6.818 |
| Ti | 0.053 | 0.036 | 0.066 | 0.000 | 0.034 | 0.032 | 0.038 | 0.001 | 0.004 |
| Al | 4.778 | 4.792 | 4.560 | 5.079 | 4.942 | 4.907 | 4.672 | 3.116 | 5.018 |
| Fe | 0.327 | 0.310 | 0.394 | 0.012 | 0.201 | 0.228 | 0.305 | 0.000 | 0.179 |
| Mn | 0.029 | 0.000 | 0.016 | 0.000 | 0.004 | 0.008 | 0.000 | 0.000 | 0.000 |
| Mg | 0.399 | 0.322 | 0.497 | 0.000 | 0.199 | 0.181 | 0.295 | 0.100 | 0.158 |
| Ca | 1.991 | 1.945 | 1.870 | 1.519 | 1.949 | 1.968 | 1.991 | 0.000 | 2.019 |
| Na | 0.734 | 0.770 | 0.844 | 0.922 | 0.790 | 0.705 | 0.886 | 2.807 | 0.745 |
| K | 0.043 | 0.055 | 0.075 | 0.002 | 0.027 | 0.036 | 0.068 | 0.003 | 0.032 |
| Cr | 0.004 | 0.005 | 0.027 | 0.000 | 0.000 | 0.009 | 0.008 | 0.000 | 0.015 |
| Ni | 0.031 | 0.000 | 0.000 | 0.191 | 0.023 | 0.032 | 0.010 | 0.000 | 0.015 |
| P | 0.000 | 0.024 | 0.042 | 0.005 | 0.015 | 0.036 | 0.011 | 0.063 | 0.003 |
| Se | 0.027 | 0.000 | 0.004 | 0.151 | 0.062 | 0.000 | 0.015 | 0.075 | 0.037 |
| Total | 15.177 | 15.100 | 15.210 | 14.897 | 15.058 | 14.982 | 15.183 | 14.959 | 13.024 |